Development of ultrathin molecularly imprinted polymer films for polyaromatic hydrocarbon sensing

by

A thesis submitted to the School of Graduate Studies in partial fulfillment of the requirements for the degree of

Master of Science

Department of Chemistry

Memorial University of Newfoundland

January 2016

St. John's Newfoundland

Abstract

Produced water is one of the pollutants produced at a large scale during offshore oil and gas activities. Wastewater which has been separated from oil and gas during production can be defined as produced water. Although produced water contains a wide variety of toxic chemicals, polycyclic aromatic hydrocarbons (PAHs) within produced water have received considerably greater attention due to their capability of causing long term toxic effects at the individual level in the marine environment. Due to the adverse effect of PAHs (organic pollutants) on the environment and lives, accurate detection and monitoring of PAHs is required before discharging the produced water into the sea. Molecularly imprinted polymers (MIPs) can capture analytes such as PAHs, and when coupled with a detection mechanism, can act as sensors for those pollutants. These films are suitable for remote sensing because they can effectively concentrate the analyte in situ. To combine MIPs with an optical sensing element, it can be useful to create them in an ultrathin film format, which is also important for portability to remote areas. One way to achieve a uniform film with nanoscale thickness is through spin coating. In this study, ultrathin film MIPs have been prepared following a new procedure. Various processing parameters including spin time and speed have been explored to determine their effects on MIP film structure as well as their removal and uptake of template molecules. Raman spectroscopy was used for the detection of the analyte, and atomic force microscopy was used to characterize the

films' morphology as well as to measure the thickness of the films, which ranged from 300 nm down to 4 nm. Our findings have determined that different spin speeds produce different film morphology. Furthermore, thinner films showed more homogeneity and reproducibility.

Acknowledgements

First of all, I praise the Almighty God for providing me the capability to complete my research.

Then, I would like to express my sincere gratitude, respect and cordial thanks to my supervisor, Dr. Erika Merschrod, Department of Chemistry, for accepting me as a masters student. Her encouragement, thoughtful guidance, caring mentorship, correction of the thesis and overall cooperation drive me in the right way throughout the period of my study.

I also would like to thank the members of my supervisory committee, Dr. Christina Bottaro and Dr. Yuming Zhao, Department of Chemistry, for their suggestions, comments and overall support.

Special thanks to all my group members and summer students specially Catherine, Ashley, Victoria and Brandon for helping me in the laboratory work.

Also thanks to all academic and administrative staff in the Department of Chemistry for their cooperation.

I am grateful to all the funding agencies: NSERC, RDC, Atlantic Canada Opportunities Agency, Petroleum Research Newfoundland and Labrador, Canada Foundation for Innovation to provide support in the research project. Also, I am thankful to School of Graduate Studies for providing scholarship.

Last but not the least, thanks to my parents and husband for their inspiration,

love, and cooperation. This thesis is dedicated to them.

Table of Contents

List of Tables

List of Figures

List of Abbreviations and Symbols

MIP	molecularly imprinted polymer
NIP	non-imprinted polymer
MAA	methacrylic acid
PDMS	polydimethylsiloxane
SERS	surface enhanced Raman scattering
AIBN	2,2'-azobisisobutyronitrile
EGDMA	ethylene glycol dimethacrylate
UV	ultraviolet
PAH	polycyclic aromatic hydrocarbon
SCCM	standard cubic centimeters per minute
RF	radio frequency
QCM	quartz crystal microbalance
AFM	atomic force microscopy
BTEX	benzene, toluene, ethyl benzene, xylenes
PW	produced water
GC	gas chromatography
MS	mass spectrometry
FID	flame ionization detection
HRGC	high resolution gas chromatography

DREAM	dose related risk and effect assessment model
MIT	molecular imprinting technique
TBZ	thiabendazole
SMO	sulfamethoxazole
TNT	2,4,6-trinitrotoluene

Chapter 1

Introduction

1.1 Polycyclic aromatic hydrocarbons

Polycyclic aromatic hydrocarbons (PAHs), a large series of hydrocarbons, are a potent and ancient type of environmental pollutant consisting of two or more fused aromatic rings [1–3]. PAHs can be divided into two classes based on their properties and molecular weight. Low molecular weight PAHs containing two or three aromatic rings exhibit acute toxicity, whereas some higher molecular weight PAHs, including four or more rings, have high carcinogenic and mutagenic properties due to their metabolic transformation capability [4]. Sixteen PAHs have been listed as priority pollutants by the US Environmental Protection Agency which include naphthalene, acenaphthylene, acenaphthene, fluorene, phenanthrene, anthrecene, fluoranthene, pyrene, chrysene, benzo[a]anthracene, benzo[b]fluoranthene, benzo[k]fluoranthene, benzo[a]pyrene, indeo[1,2,3-c,d]pyrene, benzo[g,h,i]perylene, and dibenzo[a,h]anthracene [5–7].

There are both natural and anthropogenic sources of PAHs. Volcanic eruption, forest and rangeland fires, oil seeps, and exudates from trees are some natural sources of PAHs [8, 9]. The anthropogenic sources of PAHs are domestic sewage, industrial

wastewater, municipal effluents, burning of fossil fuels, wood, production of coke, charcoal, metal smelting, petroleum refining, petroleum spills or leakage, urban run off, asphalt production, aluminium production, energy emission, and incomplete combustion of coal, oil, and gas [1, 4–6, 8–11]. Also, different organic compounds in pesticides, fungicides, detergents, dyes, and mothballs have been synthesized by using some PAHs such as naphthalene and phenanthrene [12]. Although both natural sources and anthropogenic sources introduce PAHs in the environment, anthropogenic sources contain higher PAH concentrations compared to natural sources [4,13]. In the environment, the main sources of the exposure to PAHs are plants [1], air [1, 2] , water [7, 14–17], food [1], soil [1, 6, 10], and sediment [18–22].

A considerable and worldwide concern is water pollution caused by PAHs. PAHs are found in surface waters and groundwater, including drinking water. The origins of PAHs in surface waters are atmospheric fall out, including wet and dry deposition of particles and vapors, urban run-off, municipal effluents, industrial effluent, and oil spillage or leakage [7]. The introduction of PAHs in groundwater may be due to the polluted surface water bodies, leachates from solid waste disposal sites or contaminated oil, and agricultural irrigation with effluents [1, 7]. In drinking water, PAHs may originate from raw water sources (e.g. surface and ground water) [1]. Although urban and industrial sites are the foremost sources of PAHs, high concentrations of PAHs are also found in rural and remote areas as PAHs can be transported over long distances as gases or aerosols [7]. PAHs can be transported to the sea water both via surface waters and the atmosphere [4, 23]. Studies indicate that PAH inputs to the world's oceans from atmospheric sources range from 10 to 80 % [1] and the amount of PAHs reaching the marine environment is 230000 tonnes every year [4].

In water, the solubility of PAHs is low and it decreases with increasing molecular weight of PAH. Since the nature of PAHs is hydrophobic, the concentrations of dis-

solved PAHs are very low in sea water [3,4]. In aquatic systems, a number of physical, chemical, and biological processes influence the nature and effects of PAHs. Major processes, including volatilization, dissolution, adsorption onto suspended solids, uptake by aquatic organisms and subsequent accumulation, sedimentation, and biotic and abiotic degradation are underway in aquatic systems [3, 7, 16]. In surface waters and sea water, PAHs are associated with particulate matter due to their strong affinity for organic carbon in particulate matter, and they are consequently deposited in sediments. Sediments exhibit an important exposure route for a variety of aquatic organisms to PAHs since these organisms live in contact with sediments constantly [3,4,16]. Also, PAHs can enter aquatic organisms through the food chain [20, 24, 25]. As a result, the condition of the marine environment is alarming due to its frequent pollution by PAHs. Moreover, aquatic organisms provide a pathway for PAHs to enter into human bodies by our consumption of marine organisms [20] as well as other exposure routes.

PAHs show their toxicity on different organisms such as humans, mammals, fish, birds, amphibians, reptiles, invertebrates, and plants [8]. The effect of PAHs on humans includes skin irritation, headache, nausea, vomiting, bronchitis, embryotoxicity, tetatogenicity, reproductive damage, immune disruption, endocrine disruption, cancer, and death [2, 8, 26, 27]. The effects of PAHs on fish include birth and cardiac defects, reduced growth, cranial facial malformations, yolk sac and pericardial oedema, subcutaneous haemorrhaging, fin erosion, liver abnormalities, cataracts, and immune system impairments [8, 28–32]. Also, there are many adverse health effects of PAHs on other organisms [8].

1.2 Produced water

In the marine environment, produced water can be a source of PAHs [33]. Due to high demand for energy, development of offshore oil and gas industries has increased a lot over the past 40 years which involves drilling, production, waste disposal, and transport activities [34–36]. Since various kinds of wastes are produced along with offshore oil and gas production, these offshore oil and gas activities are the sources of a variety of pollutants [37]. Produced water is one of the major sources of pollutants produced during these activities. It is a mixture of oil, gas, and water in the reservoir. This also contains some injected seawater to maintain reservoir pressure [36, 38–40]. Produced water can also be defined as fossil water due to the accumulation with the fossil fuels over million of years in geologic formations deep in the earth [37, 41, 42]. After formation of produced water on offshore oil and gas platforms, it may be either transported by pipeline to shore for treatment and disposal, or re-injected, treated and discharged to the ocean [42].

The volume of total discharged produced water to the ocean has gradually increased. In 1993, the volume of discharged produced water in the UK sector of the North Sea was 187 million tonnes, whereas 234 million tonnes of produced water were discharged in 1997 [36, 37]. On the other hand, 134 million m^3 (about 45.9 million tonnes) of produced water was discharged in the Norwegian sector of the North Sea in 2009, whereas the prediction of total volume of discharged produced water reached more than 250 million m^3 (about 88.3 million tonnes) in 2010 [40]. Each year, the estimated amount of the petroleum hydrocarbons entering into the marine environment from produced water discharges is 7500-11500 tonnes [37].

Produced water presents a wide variety of chemical compositions. It contains small amounts of dispersed oil, monocyclic aromatic hydrocarbons (BTEX: benzene, toluene, ethyl benzene, xylenes), polycyclic aromatic hydrocarbons, heterocyclic

aromatic compounds, metals (e.g. arsenic, cadmium, copper, chromium, lead, mercury, nickel, and zinc), naturally occurring radioactive materials (e.g. radium-226 and radium-228), and inorganic salts [35, 38]. Among all of these chemicals, the major toxicants in produced water are monocyclic aromatic hydrocarbons, polycyclic aromatic hydrocarbons, and heterocyclic aromatic hydrocarbons [35]. The components of produced water such as metals and dissolved hydrocarbons are of the greatest environmental concern as they are more likely to bioaccumulate and have potential for being toxic [42].

PAHs of produced water have received considerably greater attention due to their ability to cause long term toxic effects at the individual level in the marine environment. In a 2012 report, the concentration of 2- and 3-ring aromatic hydrocarbons (e.g. naphthalene, phenanthrene, dibenzothiophene, and their C1-C3 alkylated homologs) was 0.4-6.7 mg/L and 0.4-12 mg/L for 4 to 6 ring PAHs (benzo[a]anthracene, benzo[b]fluoranthene, benzo[k]fluoranthene, benzo[a]pyrene, indeo[1,2,3-cd]pyrene, chrysene, dibenzo[a,h]anthracene, fluoranthene, pyrene) in produced water on the Norwegian Continental Shelf [35]. Although produced water contains both high and low molecular weight of PAHs, the concentration of low molecular weight PAHs (e.g. 2 and 3 rings PAHs) is higher in produced water [33]. In 1996, the annual discharge of PAHs from produced water in the Norwegian sector of the North Sea was approximately 25 tonnes and it was predicted to increase as the fields get older [43]. Although the removal of the bulk amount of oil present in produced water was performed before discharges, significant amount of polycyclic aromatic hydrocarbons was released due to their involvement of the large volumes. In 2008, the involved volume of PAHs was roughly 81 tonnes in the Norwegian sector [44].

Produced water shows intense and persistent toxicity to marine organisms. PAHs of produced water are responsible for many diseases of marine organisms as mentioned

earlier. Therefore, produced water needs to be treated using a number of methods. The methods include physical treatment, chemical treatment, biological treatment, and membrane treatment, with advantages and disadvantages for each techniques [45, 46]. Note that any single produced water treatment can not produce suitable water, and therefore, the treatment of produced water might involve two or more methods. The preferred technologies involved with the best treatment of produced water depends on produced water chemistry, age of the field, space availability, cost effectiveness, durable operations, by products, and reuse and discharge plans [45].

Treated produced water can be reused for many purposes such as industrial (e.g. dust control, vehicle cleaning, and fire control) and crop irrigation in semiarid environments where water is insufficient [47]. Although treated produced water can be used as an alternative irrigation source, it has short term effects on microbial activity of soil cultivated with bio-energy plants. It also negatively affects the growth of micro organisms and microbiological activity of soil in semiarid environments. As a result, both before and after treatment, the monitoring at sea of contamination of produced water discharges, more specifically PAHs, is necessary.

There are five techniques of monitoring PAHs of aquatic environment monitoring. They are chemical monitoring, bioaccumulation monitoring, biological effect monitoring, health monitoring, and ecosystem monitoring [33]. In the organisms, the environmental impacts of PAHs of produced water at sea has been monitored by using biological markers of PAHs exposure. The chemical analysis is carried out with different spectrometry such as gas chromatography/mass spectrometry (GC-MS), fluorescence spectrometry, and gas chromatography with flame ionization detection (GC-FID) [39, 40, 48–50]. The biological marker monitoring study is defined as biomonitoring, which is a robust and sensitive method. This method provides the information on uptake and biotransformation of PAHs compounds that may cause

the biological effects of fish [39, 48, 51].

Semi permeable membrane devices (SPMDs) with GC-MS detection system have been extensively used for detecting low concentration PAHs, present in the water column of sea [52]. SPMDs generally provide reliable estimates and have several advantages over living organisms to measure the levels of seawater contaminants. They can also be used in heavily contaminated marine environments where a single bioindicator is not available or living organisms may not survive [53]. However, the measured concentration of PAHs of the water column using SPMDs are not identical to living organisms in the sea [52]. Again, SPMDs, blue mussels, and dose related risk and effect assessment model (DREAM) predictions with high resolution gas chromatography/-mass spectrometry (HGGC-MS) are used to estimate PAHs concentration [41, 42]. Also, SPMDs and blue mussels data with GC-FID detection are used to measure the concentration of PAHs [53]. These detection techniques require sample preparation and laboratory work before performing the detection analyses.

On the other hand, sensors can also be used to detect PAHs directly in seawater. Molecularly imprinted polymers (MIPs) can be used for capturing and removing PAHs from water, a key step in on-site sensing. These MIP-based sensors can be applied for environmental monitoring and remote sensing [54]. They can also be used to concentrate and remove trace concentrations of PAHs from contaminated seawater [55].

1.3 Molecularly imprinted polymer (MIP)

A molecularly imprinted polymer (MIP) is a synthetic, robust, and functional molecular recognition element, synthesized around a target molecule called template [56, 57]. The molecular imprinting technique (MIT) was first introduced by M. K. Polyakov in

1931 as “unusual adsorption properties of silica particles prepared using a novel synthesis procedure” [58–60]. This is a rapidly developing effective method and mainly used to prepare polymers such as MIPs [58–60].

MIT is a relatively easy and cheap technique where a template molecule is combined with a functional monomer, a cross-linker, and an initiator either in an aprotic or a non polar solvent to make a pre-polymerization complex. This step is known as a pre-polymerization step which is followed by a polymerization step. In the polymerization step, polymerization is initiated either thermally (applying heat) or photochemically (using UV light). Thus, the pre-polymerization complex is stabilized within the rigid, highly cross-linked polymer matrix [61–63]. After polymerization, the template is removed, leaving specific binding sites (also known as cavities) in the polymer matrix. The purpose of creating the cavities is to enable the polymer matrix to rebind molecules. They can even serve to capture the template molecules from a mixture of firmly related compounds [61, 63].

To create the specific binding sites in the polymer matrix, several kinds of molecular imprinting procedures have been normally used: covalent imprinting, non-covalent imprinting, stoichiometric non-covalent imprinting, semi-covalent imprinting, and metal ion-mediated imprinting [59, 60, 64]. Among all these methods, covalent and non-covalent imprinting have been widely used as the main methods [58, 65]. In the covalent imprinting method, an easily cleavable covalent bond is formed between template and functional monomer. The template molecule is then removed from the polymer matrix by cleaving the covalent bond between the template and functional monomer [61, 62].

On the other hand, in the non-covalent imprinting method, the template molecule is bonded with the functional monomer by non-covalent bonding, such as hydrophobic interactions, hydrogen-bonding, or ionic bonding [61, 62]. As no chemical interactions

are present between the template and functional monomer, the template can be easily removed by washing with a solvent. Between the two imprinting processes, non-covalent imprinting is widely used as it has several advantages: it is an easy procedure; template removal is much easier; it provides higher affinity binding sites; and a wider range of functional monomer can be introduced into the specific binding sites [58,61]. Furthermore, suitable templates are limited for covalent imprinting as quick reversible covalent interactions between templates and functional monomer are required to form alike rebinding linkages which makes this method a less flexible one [58].

MIPs have been extensively used in many areas associated with chemistry and biology. They have become very popular as a binding assay and adsorbent in separation methods [61, 66–70], sensors (e.g. chemical sensors and biosensors) [61, 71–78], catalysis [79], and artificial antibodies [80, 81] due to their low cost, high selectivity and sensitivity, and flexibility in preparation [58, 82, 83]. They have been utilized to detect and remove various toxic compounds from environmental, bioanalytical, pharmaceutical, and food samples [58].

Various physical formats of MIPs are being used to make MIPs for many different applications. For example, MIP particles can be prepared by bulk polymerization; MIP beads and microspheres can be prepared by suspension, multi-swelling, and precipitation polymerization; thin imprinted MIP layers onto preformed beads can be prepared by surface grafting polymerization; and monolith MIPs can be prepared by in-situ polymerization [58, 61, 84]. Researchers such as Gonzalez et al. [85], McStay et al. [86], and Karsten Haupt [68] utilized bulk polymerization to prepare digoxin MIP, and triazine MIP, BOC-phenylalanine MIP, 2,2-bipyridyl MIP, and herbicide 2,4-dichlorophenoxyacitic acid based MIP respectively. Barahona et al. [87] used surface grafting and precipitation polymerization to synthesize thin films of thiabendazole (TBZ)-imprinted polymer and TBZ core shell MIP particles. Ansell et

al. [88] synthesized (R,S)-propranolol imprinted magnetic beads by using suspension polymerization for drug radioligand binding assay. Liu et al. [89] synthesized a sulfamethoxazole (SMO)-MIP monolith column to identify the ingredients of SMO in three kinds of pharmaceutical tablets.

Bulk MIPs prepared by traditional methods are used as an adsorbent that is coupled with different analytical techniques to detect and remove toxic compounds such as PAHs from water. For instance, Krupadam et al. [90] synthesized a PAH-imprinted polymer adsorbent by using bulk polymerization to detect 16 different PAHs from wastewater. In another study, Krupadam et al. [91] synthesized a pyrene-imprinted adsorbent to detect PAHs from sea water. In sea water, the pyrene-imprinted adsorbent had a binding capacity of 35 mg/g. Also, Krupadam et al. later synthesized a 6PAH-imprinted polymer adsorbent to remove PAHs from contaminated water samples [55]. The binding capacity of the 6PAH-imprinted polymer adsorbent was 687 μg/g. Song et al. [92] synthesized a 16PAH-imprinted polymer adsorbent to remove PAHs from sea water. The binding capacity of this adsorbent was 111-190 μg/g, and the adsorbent removed 93.2 % PAHs from natural sea water. Although this MIP-adsorbent shows good results to detect PAHs in water, these traditional bulk techniques of making PAH-MIPs have many disadvantages (e.g. long procedure, time consuming) [61, 93]. Also, longer procedures (e.g. grinding, sieving) are used for removal of the template.

MIPs can also be used in a film format to detect and remove toxic compounds in sensor applications [65, 94–97]. In order to use an MIP as part of a microfabricated sensor package, it helps to have it as a film. The general approach of using a MIP in sensing applications is the attachment of the MIP onto the surface of a transducer which senses binding events between the MIP and the target analyte and sends a measurable signal to the user. For many transducing methods a thin film MIP is

required, and the sensitivity of this device is optimized controlling the thickness and porosity of the film [94].

Researchers [94] have introduced a simple, quick, and robust technique for preparing MIP films (e.g. thin and ultra thin) using spin coating. Using spin coating, a MIP pre-polymerization mixture can be spread on to a substrate and the films can be cured using UV photolysis. This technique can produce porous films that can be useful for adsorption applications. MIP films produced using this technique contain the same selectivity properties as traditional bulk MIPs. As presented in chapter 5, the films produced using this method and reported herein have better homogeneity.

Unlike bulk polymer characterization studies, thin films do not require grinding or sieving [64]. Holthoff et al. [98] synthesized a micron thick xerogel MIP film containing 2,4,6-trinitrotoluene (TNT) as an analyte to detect TNT from explosive materials. Tokareva et al. [99] synthesized a poly(2-vinylpyridine) ultra thin MIP sensor layer to detect cholesterol molecules in samples. Furthermore, spin coated MIP sensitive layers can be used to detect PAHs from contaminated water. Dickert et al. [100] synthesized highly sensitive double imprinted MIP layers to detect PAHs from water. It was noted that the detection limit of PAHs was approximately 30 ng/L.

1.4 Detection of PAHs

In situ detection of individual PAHs in a natural environment is a challenging task as PAHs are present in mixtures rather than individually in the environment [101]. Several detection methods have been used to detect PAHs in natural environment. The most conventional detection methods are mass spectrometry [102], capillary electrophoresis [103, 104], quartz crystal microbalance [103], electrochemiluminescence [103], fluorescence spectrometry [102, 103], and immunoassays [102], sometimes with

prior sample preparation high performance liquid chromatography [101,102,104,105], liquid chromatography [104], or gas chromatography [101, 104]. Most of the conventional techniques have disadvantages as most of these methods need sophisticated sampling procedures [102], and a laborious and time-consuming preconcentration step [101, 104]. Although liquid chromatography in combination with fluorescence or absorbance detection, and gas chromatography in combination with mass spectrometry have a powerful ability to detect PAHs in mixture, the expensive instrumentation and time-consuming sample preparation procedures limit their application to in situ analysis [103].

The main detection technique in sensor applications used frequently in combination with MIPs is fluorescence [62]. However, this technique has some disadvantages. It can only detect fluorescent or fluorescently labeled template molecules [62,106,107]. Moreover, it is hard to differentiate PAHs using fluorescence spectroscopy because of the similarity of PAH structure and broadening of emission bands [108]. To overcome these limitations, Raman spectroscopy has been used for the identification of binding and release of target molecules to and from MIPs [86, 106].

1.4.1 Raman Spectroscopy

Raman spectroscopy is a promising spectroscopic technique for the identification and quantification of PAHs having high specificity and sensitivity [109, 110]. Raman scattering is a vibrational spectroscopic technique where the sample inelastically scatters the incident laser light [111]. Raman spectroscopy is convenient to study environmentally relevant samples because of the ability to study aqueous solutions as well as the identification and quantification of a wide range of chemical species and states [109]. It is a fast and non-destructive characterization tool which provides distinct sample identification [112]. The spectrum is like a molecular "fingerprint" that offers

high resolution and gives structural and electronic information of the samples [113]. In addition, the technique is also suitable to environmental analysis due to its easy portability and rapid sample analysis time [114]. Compared to fluorescence bands, Raman bands are normally 10 to 100 times narrower. In a given spectral region, the probable overlap of different peaks is therefore reduced for the Raman bands [115]. Moreover, humidity, presence of oxygen, or other quenchers do not affect the sensitivity of Raman scattering [115]. This technique could be applied in aqueous media due to the small Raman scattering cross section of water [116].

However, Raman spectroscopy has also some limitations. It produces weak signals; therefore, the identification of trace amount of chemical species is difficult [114, 116, 117]. Moreover, fluorescence can interfere with the Raman signal [114]. These limitations can be overcome by using Surface Enhanced Raman Scattering (SERS) [114, 116]. SERS is a powerful spectroscopic technique that enhances the Raman signals of adsorbed molecules on metallic surfaces due to the interaction between adsorbed molecules and nanostructured metallic surfaces [109, 117]. Besides having all the advantages of Raman spectroscopy, SERS can be further used to identify trace amounts of single individual molecules [108, 109]. The magnitudes of Raman signals of the molecules can be enhanced by a factor of 10^{10} in SERS measurements [118].

Due to its highly sensitive and selective analysis, the concept of SERS permits its utilization in emergency and rapid response detection as SERS sensor chips [116]. This technique is also widely used for the detection of trace amounts of PAHs from the marine environment [108, 109, 111, 117]. In addition, SERS with MIPs can be used as a new approach in sensing applications [98] where SERS works as a transducer to gain an immense level of sensitivity. The excellent detection capabilities of SERS achieved by the enhancement of Raman signals of adsorbed analytes on metal surfaces make it an outstanding transduction method for selective detection whereas the other existing

MIP sensors currently do not have that capability.

In the MIP-SERS concept, the MIP concentrates the target analyte adjacent to a SERS-active surface which enhances the Raman scattering of analyte molecules [98]. Holthoff et al. [98] synthesized a MIP-SERS sensor for the detection and identification of 2,4,6-trinitrotoluene from explosive materials. Kantarovich et al. [119] synthesized MIP droplets on a SERS-active surface by using a pipet or a nano fountain pen and precisely monitored template molecules by SERS. Liu et al. [120] synthesized theophylline MIPs on rough surface of silver nanoparticles. Recent study shows that an efficient and robust chemical nanosensing system can be developed using this combination of integrated MIP-SERS. Moreover, high selectivity, sensitivity, and portability in sensing applications can be maintained as well as the cost and size of the sensor can be minimized if a proper MIP-SERS sensing format can be introduced [98].

1.5 Objectives

The main purpose of this study is to prepare ultrathin film MIPs on different substrates following a new procedure. Testing the efficiency and performance of the MIP-substrates is another important part of this thesis. Another objective of this study is to determine the effects of different processing parameters such as spin time and speed on the ultrathin MIP film structure as well as removal and reuptake of analyte molecules. Laboratory tests are carried out to diagnose the unique analyte peak for analyte's removal and reuptake, and to identify the suitable analyte's reuptake time.

Chapter 2

Experimental

2.1 MIP synthesis

Variations in mixing method, volume of solvent, and reagents were tested to make different types of molecularly imprinted polymer (MIP).

2.1.1 MAA-based bulk MIP

The precursors used for making bulk MAA-based and MAA-based modified MIPs were methacrylic acid (MAA), a functional monomer; ethylene glycol dimethacrylate (EGDMA), a cross-linker; 2,2'-azobisisobutyronitrile (AIBN), a polymerization reaction initiator; phenanthrene, a template molecule; and acetonitrile, a solvent. The reaction scheme is shown in Figure 2.1. MAA and EGDMA were obtained from Sigma Aldrich. A non-imprinted polymer (NIP), made without using a template molecule, was prepared to distinguish between the spectra of the NIP and the MIP.

During the polymerization process, the ratio of the template and functional monomer was used as 1:4 whereas the ratio of the functional monomer and the cross-linker was 4:40 [90]. For each MIP synthesized, an analogous non-imprinted polymer

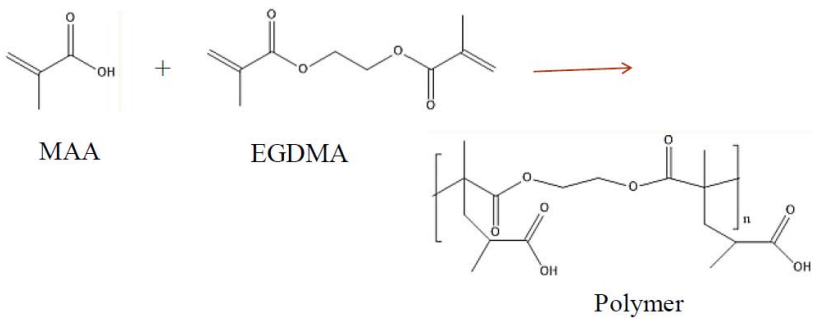

Figure 2.1: Reaction scheme for production of molecularly imprinted polymer

was also prepared following the same procedure but without adding the template molecule. All liquids were measured and transferred using micropipettors. Three steps were used to mix the precursors for making bulk MAA-based MIP.

1. A solution was prepared mixing 3.8 μL MAA (d= 1.015 g/cm^3), 915 μL EGDMA (d=1.051 g/cm^3), and 0.002 g phenanthrene. The mixture was then dissolved in 200 μL acetonitrile and was termed as Solution A.

2. Solution B was produced by dissolving 0.002 g AIBN in 100 μL acetonitrile.

3. 20 μL solution A, 10 μL solution B, and 70 μL acetonitrile were then mixed together.

The polymer mixture was then polymerized for 10 mins using 400 W EC Silver Series UV light source flood lamp system (Dymax).

2.1.2 MAA-based modified bulk MIP

Two additional kinds of bulk MAA-based MIPs were synthesized using a different mixing procedure. The ratio of the template, the functional monomer, and the cross-linker was the same whereas the amount of the precursors and the solvent was different for each MAA-based modified MIP.

In both cases, the following mixing procedure was used:

1. Solution A - 7.6 μL MAA (d= 1.015 g/cm^3) and 0.004 g phenanthrene (template) were dissolved in 200 μL acetonitrile.

2. Solution B - 1830 μL EGDMA (d=1.051 g/cm^3) was dissolved in 200 μL acetonitrile.

3. Solution C - 0.004 g AIBN was dissolved in 200μL acetonitrile

4. 20 μL solution A, 20 μL solution B, 20 μL solution C, and additional acetonitrile were then mixed together.

For the first type (modified procedure 1), 140 μL acetonitrile was added in the last step, while for the second type (modified procedure 2) only 20 μL were used. Then the solution was polymerized for 10 mins using 400 W EC Silver Series UV light source flood lamp system (Dymax).

2.1.3 Ultrathin film MIP

Bulk MAA-based and bulk MAA-based modified MIP (modified procedure 1) were used to make ultrathin film MIPs. To spread the MIP solution onto substrates, models WS-650SZ-6NPP/LITE and WS-400B-6NPP/LITE (Laurell Technologies Corporation) spin coaters were used. Three different instruments were used to polymerize these ultrathin film MIPs. A few MAA-based ultrathin film MIPs were polymerized by using the SF-100 Intelligent micro patterning system, LLC. The light of the Intelligent micro patterning system used during exposure had ultraviolet energy (UV) of 365 nm, and at 365 nm the irradiance level was approximately 25 watt/cm^2. Other MAA-based ultrathin film MIPs were polymerized by using a hot plate at 100 ^{o}C in ambient light. Finally, some MAA-based modified ultrathin film MIPs made with modified procedure 1 were polymerized by using the 400 W EC Silver Series UV light

Table 2.1: MAA-based ultrathin film MIPs on glass slides exposed for 300 s : varying spin speed

Sample	Spin speed (rpm)	Spin time (s)	Exposure time (s)
1	500	60	300
2	800	60	300
3	1000	60	300
4	1100	60	300
5	1400	60	300
6	1800	60	300
7	2000	60	300

Table 2.2: MAA-based ultrathin film MIPs on glass slides exposed for 60 s: varying spin speed

Sample	Spin speed (rpm)	Spin time (s)	Exposure time (s)
1	1000	60	60
2	1400	60	60
3	1800	60	60

source flood lamp system (Dymax). The various parameters used for making MAA-based and MAA-based modified ultrathin film MIPs on different substrates are shown in Tables 2.1, 2.3, 2.2, 2.4, 2.5, and 2.6.

2.1.4 Polydimethylsiloxane (PDMS)-based MIP

Given the extensive literature on spin coating PDMS and the ease of preparation of the crosslinked polymer [121, 122], PDMS was also tested as a MIP. To make non-imprinted polydimethylsiloxane, PDMS base monomer and curing agent were mixed in a 10:1 (weight:weight) ratio and cured for 6 mins at 140 ^{o}C on an Al wrapped glass slide. Three protocols were tested:

Table 2.3: MAA-based ultrathin film MIPs on Si substrates exposed for 300 s: varying spin speed

Sample	Spin speed (rpm)	Spin time (s)	Exposure time (s)
1	1000	60	300
2	2000	60	300

Table 2.4: MAA-based ultrathin film MIPs on glass slides thermally cured for 60s: varying spin speed

Sample	Spin speed (rpm)	Spin time (s)	Cure time (s)
1	1000	60	60
2	1500	60	60
3	1800	60	60
4	2000	60	60

Table 2.5: MAA-based modified ultrathin film MIPs on glass slides (modified procedure 1) spun for 60 s: varying spin speed and exposure time

Sample	Spin speed (rpm)	Spin time (s)	Exposure time (s)
1	100	60	360
2	200	60	360
3	300	60	360
4	400	60	360
5	500	60	360
6	300	60	600
7	400	60	600
8	500	60	600
9	200	60	180
10	2000	60	180

Table 2.6: MAA-based modified ultrathin film MIPs on Si substrates (modified procedure 1) spun for 30 s: varying spin speed and exposure time

Sample	Spin speed (rpm)	Spin time (s)	Exposure time (s)
1	200	30	120
2	300	30	30

1. The ratio of PDMS base monomer and curing agent used for making PDMS-based MIP was 1:9 (weight:weight). 0.110 g PDMS base monomer and 0.900 g curing agent were mixed with 0.004 g phenanthrene to make PDMS-based MIP. Solvent (toluene) was used to dissolve phenanthrene. No sonication was used for mixing the materials.

2. The ratio of PDMS base monomer and curing agent used for making PDMS-based MIP was 1:4 (weight:weight). 0.060 g PDMS base monomer and 0.280 g curing agent were mixed with 0.004 g phenanthrene to make PDMS-based MIP. Solvent (toluene) was used to dissolve phenanthrene. No sonication was used for mixing the materials.

3. The ratio of PDMS base monomer and curing agent used for making PDMS-based MIP was 10:1 (weight:weight) [121–123]. 1.000 g PDMS base monomer and 0.100 g curing agent were mixed with 0.004 g phenanthrene to make PDMS-based MIP. Two different solvents (toluene and ethanol) were used to dissolve phenanthrene. Sonication was used for mixing the materials.

To make PDMS-based MIP as an uniform thin film onto substrates, models WS-650SZ-6NPP/LITE and WS-400B-6NPP/LITE (Laurell Technologies Corporation) spin coaters were used. Using protocols 1 or 2, thin films on Al-wrapped glass substrates were spun at 2000 rpm for 30s. Then the films were thermally cured for 90 s.

A wider variety of parameters (e.g. spin speed, cure time, types of solvent, volume of solvent, and sonication time) were applied to deposit PDMS-based MIP as an ultrathin film onto the Al wrapped glass substrates using the protocol 3. The parameters were changed to see the changes of the Raman spectra of the films. The variation of the parameters is described in Table 2.7.

Table 2.7: PDMS-based MIP on Al wrapped glass slides (protocol 3) spun for 30 s: varying solvent, spin speed, cure time, and sonication time.

Sample	Solvent		Spin		Cure	Sonication
	Type	Volume (μL)	speed (rpm)	time (s)	time (s)	time (s)
1	toluene	100	500	30	90	3600
2	toluene	130	500	30	120	3600
3	toluene	130	800	30	120	3600
4	toluene	130	1000	30	90	4500
5	toluene	130	1300	30	90	4500
6	toluene	100	2000	30	90	3600
7	ethanol	100	2000	30	90	3600
8	ethanol	300	2000	30	90	3600

2.2 Substrate surface modification

To deposit MIP as an ultrathin film on substrates, surface modification of the substrates is an important issue and therefore needs to be considered. The surface of the substrates should be hydrophilic rather than hydrophobic so that the whole surface of the substrates would be wetted by the MIP solution. Hence, the most important thing is to modify the surface of the substrates before depositing MIP as an ultrathin film on the substrates. Moreover, the other important thing is to reduce fluorescence generated from the substrates to identify the formation of MIP as an ultrathin film on the substrates by Raman spectroscopy.

2.2.1 Plasma treatment

To have an uniform film rather than MIP islands on the substrates, the improvement of hydrophilic properties of the substrates is crucial. Therefore, the wetting capability of the substrates needs to be addressed. One way to achieve this wetting capability is oxygen-plasma treatment. A PF-100 Series plasma system (Plasma Etch, Inc.) was used for oxygen-plasma treatment. In this system, the flow rate of oxygen gas was between 40 to 50 SCCM and the maximum RF power supply was 300 W. The plasma

processing period was 5 s.

2.2.2 Siloxane-based polymer (PDMS) coated substrates

Siloxane-based polymer (PDMS) coated substrates were made to reduce fluorescence emission from substrates. PDMS was made by mixing base monomer and curing agent conjointly in a 10:1 (weight:weight) ratio. The mixture was sonicated for 2100 s. The parameters such as spin speed, spin time, and cure time were applied to deposit PDMS onto glass and Si substrates. The parameters are shown in Tables 2.8 and 2.9

2.2.3 Carbon-based photoresist coated substrates

An epoxy-based negative photoresist polymer, SU-8, was also used to cover fluorescence emission from substrates. SU-8 2010 series was purchased from MicroChem. Several parameters were used to deposit SU-8 onto the glass and Si substrates. The polymer was polymerized with SF-100 Intelligent micro patterning system, LLC. The parameters are stated in Tables 2.10 and 2.11.

A positive photoresist, S1813, was also deposited onto glass and Si substrates to check whether it could block fluorescence from these substrates. S1813 was purchased from MicroChem. Several parameters were used to deposit S1813 onto the glass and Si substrates. The parameters used in this process are mentioned in Tables 2.12 and 2.13 .

2.2.4 Metal coating

Metal coated substrates were prepared to reduce fluorescence emission from the substrates. Al was deposited on glass slides and Si substrates using a thermal metal evaporator built in house (courtesy of Prof. M. Clouter, Department of Physics, Memorial

Table 2.8: PDMS on glass slides thermally cured at 100 °C: varying spin speed, spin time, and cure time

Sample	Spin Speed (rpm)	Spin Time (s)	Cure Time (s)
1	100	60	360
2	200	60	360
3	300	60	360
4	400	60	360
5	500	60	360
6	600	60	360
7	700	60	360
8	800	60	360
9	900	60	360
10	1000	60	360
11	1100	60	360
12	1200	60	360
13	1300	60	360
14	1400	60	360
15	1500	60	360
16	1600	60	180
17	1700	60	180
18	1800	60	180
19	1900	60	180
20	2000	60	180
21	1000	30	360
22	1100	30	360
23	1200	30	360
24	1300	30	360
25	1400	30	360
26	1500	30	360

Table 2.9: PDMS on Si thermally cured at 100 °C: varying spin speed

Sample	Spin Speed (rpm)	Spin Time (s)	Cure Time (s)
1	400	60	360
2	500	60	360
3	600	60	360
4	700	60	360
5	800	60	360
6	900	60	360
7	1000	60	360
8	1300	60	360
9	1600	60	360
10	1900	60	360
11	2200	60	360
12	2500	60	360
13	2800	60	360
14	3000	60	360
15	3500	60	360
16	4000	60	360
17	4500	60	360
18	5000	60	360
19	5500	60	360
20	6000	60	360
21	6500	60	360
22	7000	60	360

Table 2.10: SU-8 on glass slides exposed for 60 s: varying spin speed

Sample	Spin Speed (rpm)	Spin Time (s)	Exposure time (s)
1	500	60	60
2	1000	60	60
3	2000	60	60

Table 2.11: SU-8 on Si substrates exposed for 60 s: varying spin speed

Sample	Spin Speed (rpm)	Spin Time (s)	Exposure time (s)
1	500	60	60
2	1000	60	60
3	2000	60	60

Table 2.12: S1813 on glass slides thermally cured for 60 s at 100 °C: varying spin speed

Sample	Spin Speed (rpm)	Spin Time (s)	Cure Time (s)
1	500	60	60
2	1000	60	60
3	2000	60	60

Table 2.13: S1813 on Si substrates thermally cured for 60 s at 100 °C: varying spin speed

Sample	Spin Speed (rpm)	Spin Time (s)	Cure Time (s)
1	500	60	60
2	1000	60	60
3	2000	60	60

University). The chamber pressure of the thermal metal evaporator was 4 x 10^{-4} torr, and the thickness of the Al layer was approximately 500 nm as measured by quartz crystal microbalance (QCM, Infinicon from Kurt J. Lesker Company).

Additional metal coated slides (Ag/Au/silica spheres on glass slides) were prepared by other members of the Merschrod group to enable SERS measurement with the ultrathin film MIP. The procedure of the metal coated slides is described below. First, 460 nm silica spheres were dispersed in methyl ethyl ketone and were spin coated at 3000 rpm for 45 s on the glass slide. Then, first Au and then Ag were deposited using the thermal metal evaporator. During deposition, the chamber pressure was 3 x 10^{-4} torr and the evaporation rate was 0.7 to 1.5 Å/s. The deposited metal thicknesses was 200 nm of Ag and 22 nm of Au as measured by QCM.

All other metal coated slides were taken from another group member to test the formation of the ultrathin film MIP [124].

2.2.5 Treatment of the Ag/Au/silica spheres on glass substrate

To deposit MIP as an ultrathin film on the Au/Ag/Silica spheres on glass substrate, it is very important to improve the interaction between MIP and Ag/Au/Silica sphere. This interaction could be improved by increasing hydrophilic properties of the surface of the Au/Ag/Silica spheres substrate. Hydrophilicity of the surface was improved by using a 10 mmol solution of 11-mercaptoundecanoic acid (Sigma-Aldrich) in 95% ethanol [125, 126]. The substrate was immersed for 24 h. Then, the substrate was washed by using ultra pure water.

2.3 MAA-based modified ultrathin film MIPs on modified substrates

2.3.1 PDMS coated substrates

MAA-based modified MIP recipes (modified procedure 1 and modified procedure 2) were deposited as an ultrathin film on the PDMS on glass substrates and Si substrates. The films were made with varying parameters and polymerized by using 400 W EC silver series UV light source flood lamp system and hot plate at 60 ^{o}C. The parameters used in the making of the films are described in Tables 2.14, 2.15, and 2.16 .

2.3.2 MAA-based ultrathin film MIPs on metal coated substrates

Some metal coated ultra thin MIP films were made using MAA-based bulk MIP recipe. The MIP solution was spread on the metal coated slides by using the spin

Table 2.14: MAA-based modified ultrathin film MIPs on PDMS on glass slides (modified procedure 1) exposed for 30 s: varying spin speed

Sample	PDMS spin		MIP spin		MIP exposure
	speed (rpm)	time (s)	speed (rpm)	time (s)	time (s)
1	400	60	100	30	30
2	400	60	300	30	30
3	500	60	100	30	30
4	500	60	300	30	30
5	800	60	100	30	30
6	800	60	300	30	30

Table 2.15: MAA-based modified ultrathin film MIPs on PDMS on Si substrates (modified procedure 1) exposed for 120 s: varying spin speed

Sample	PDMS spin		MIP spin		MIP exposure
	speed (rpm)	time (s)	speed (rpm)	time (s)	time (s)
1	700	60	100	30	120
2	800	60	100	30	120
3	800	60	200	30	120
4	800	60	300	30	120

Table 2.16: MAA-based modified ultrathin film MIPs on PDMS on Si substrates (modified procedure 2) spun for 30 s and thermally cured for 14400 s

Sample	PDMS spin		MIP spin		MIP exposure
	speed (rpm)	time (s)	speed (rpm)	time (s)	time (s)
1	500	60	100	30	14400

Table 2.17: MAA-based ultrathin film MIPs on different types of metal coated slides spun at 1000 rpm for 60 s and exposed for 300 s

Sample	Metal coated slides
1	Al on glass
2	Al on Si
3	Al on plastic
4	Ag on plastic
5	Ag/Cu on plastic
6	Cu on plastic
7	Au/SU8 on plastic
8	Au/Ag on plastic

Table 2.18: MAA-based ultrathin film MIPs on metal coated slide spun at 1000 rpm for 60 s and exposed for 300 s: varying annealed temperature

Sample	Metal coated slide	Annealed temperature (°C)
1	Ag/Cr on glass	250
2	Ag/Cr on glass	300
3	Ag/Cr on glass	350
4	Ag/Cr on glass	400

coater named Model WS-650SZ-6NPP/LITE (Laurell Technologies Corporation), and the film was then polymerized by using SF-100 Intelligent micro patterning system, LLC. The parameters used making of the other metal coated ultrathin films with MAA-based MIP recipe are shown in Table 2.17 and Table 2.18.

2.3.3 MAA-based modified ultrathin film MIPs on metal coated substrates

MAA-based modified bulk MIP (modified procedure 1) was deposited as an ultra thin film on the Ag/Au/Silica spheres substrate. Model WS-400B-6NPP/LITE (Laurell Technologies Corporation) spin coater was used to spread MIP solution on the substrate. The films were made using spin speed 500 rpm and spin time 30 s. A few films were then polymerized using a hot plate at 50 °C for 10 mins, and the other films were polymerized using the SF-100 system (Intelligent micro patterning, LLC).

2.4 Preparation of stock phenanthrene solution

Two phenanthrene stock solutions of 1.6 ppm were prepared using different sonication times. The phenanthrene solutions were prepared by adding 1.6 mg solid phenanthrene to 1 L ultrapure water (18 MΩ·cm, Barnstead Thermolyne). The first solution was sonicated for 60 mins, and the second solution was sonicated for 240 mins in order to dissolve all phenanthrene in the water. Also, different concentrations of aqueous phenanthrene solution (e.g. 0.4, 0.6, 0.8, 1.0, 1.2, and 1.4 ppm) were prepared to check the reuptake capabilities of template from different template concentrations. The solutions were prepared by adding 0.4, 0.6, 0.8, 1.0, 1.2, and 1.4 mg solid phenanthrene to 1 L ultrapure water (18 MΩ·cm, Barnstead Thermolyne).

2.5 Template/analyte removal and reuptake of MAA-based modified bulk MIPs

The template was removed from MAA-based modified bulk MIPs (modified procedure 1 and 2). The MAA-based modified bulk MIP (modified procedure 1) was washed with 95 % acetonitrile 0 to 17 times, and the other MAA-based bulk MIP (modified procedure 2) was washed with the same solvent 0 to 18 times. Then the bulk MIPs were washed with water and dried at room temperatures.

To reuptake the template molecule from the water with MAA-based modified bulk MIPs (modified procedure 1 and 2), phenanthrene stock solutions were used. The MAA-based modified bulk MIP (modified procedure 1) was immersed into the first 1.6 ppm aqueous phenanthrene (template) solution for 0 to 18 mins and the MAA-based modified bulk MIP (modified procedure 2) was immersed into the second 1.6 ppm aqueous phenanthrene (template) solution for 0 to 45 mins in order to capture

the template from the solution. Then the bulk MIPs were washed with water and dried at room temperatures.

2.6 Template/analyte removal and reuptake of ultrathin films

2.6.1 Template/analyte removal and reuptake of MAA-based modified ultrathin film MIP on PDMS on Si substrates (modified procedure 1)

Removal of template was done with the MAA-based modified MIP ultra thin films (modified procedure 1). Films were washed with 95 % acetonitrile for 0 to 15 times. Then, the films were washed with water and dried at room temperatures. After, the films were immersed into second 1.6 ppm aqueous phenanthrene solution for 0 to 8 mins in order to uptake the template from the solution. The films were then rinsed with water and dried at room temperatures after every immersion.

In order to check the reuptake capabilities of template from different template concentrations, MAA-based modified ultrathin film MIPs (modied procedure 1) were immersed into different concentrations of aqueous phenanthrene solution for 6 mins after removal of template. The concentrations of the aqueous phenanthrene solution was 0.4, 0.6, 0.8, 1.0, 1.2, 1.4, and 1.6 ppm.

2.6.2 Template/analyte removal and reuptake of PDMS-based MIP thin film

To remove template molecule from the PDMS-based ultrathin film MIPs, the films were consecutively washed several times with either 1500 μL acetonitrile each time or 700 μL 95 % ethanol each time.

Reuptake studies were done for those films which template was removed using acetonitrile. The films were immersed into second 1.6 ppm aqueous phenanthrene solution for 0 to 48 mins in order to rebind the template from the solution.

2.7 Raman Spectroscopy

To confirm the formation of the bulk MIP, the ultrathin film MIP, and the corresponding NIPs, and to monitor template removal and analyte uptake, a Raman spectrometer (Renishaw inVia, UK) was used. In this system, a laser beam of 830 nm was focused onto the sample through a Leica DM 2500 microscope using a 50x objective. Moreover, 20x was used to focus several samples. 100% of laser power was used for most samples. Cases where lower power was used are indicated in the subsequent chapters. The exposure time of the Raman spectra was 10 s for most samples. Cases where other exposure times were used are indicated in the subsequent chapters. The Raman spectrometer was calibrated in static mode by using a silicon wafer which has a Raman peak at 520.5 cm^{-1}. Extended mode was used to collect data, covering 100 to 1800 cm^{-1} in most cases. However, a few samples' spectra were recorded using a range from 100 to 3200 cm^{-1}. To analyse the Raman spectra of the samples, Renishaw WiRE 3.4 and Igor Pro 6.31 (Wavemetrics) software were used.

2.8 AFM

Atomic Force Microscopy (AFM) was used to characterize the morphology and the thickness of ultrathin film MIPs. Also, some of the Ag/Cr film thicknesses were measured by using a contact mode AFM with a silicon cantilever tip (CSC37/Cr-Au, MikroMasch) with force constants of 0.1 to 0.4 N/m and a resonant frequency of 17 to 24 kHz. The Asylum research MFP-3D procedures within Igor were used to take images and extract data such as thickness and roughness. Images were taken using contact mode with a scan rate of 1 Hz and set point of 0 V. In order to measure the thickness of the film, the film was scratched in a small area by applying a higher set point of 1 V.

2.9 Profilometer

KLA-Tencor AlphaStep Development Series Stylus Profiler, a contact profiler, was also used to measure some ultrathin film MIPs and Ag/Cr thin film thicknesses. The wavelength of the diode laser beam used in the profiler is 635 nm. The profiler has the ability to measure the height of the film thickness from under 10 Å to 1.2 mm. In order to measure the height of the film thickness, the film was first scratched with an Olfa cutter 300 snap-off blade. The film was then scanned across the scratched area. The scan was performed at a scan rate 0.4 mm/sec with 750 data points over 0.6 mm.

Chapter 3

Characterization and Modification of Bulk MIPs

3.1 Introduction

This chapter focuses on the characterization and modification of bulk MIPs made using different procedures. In addition to briefly describing the evaluation of procedure modifications, the chapter also presents findings on the removal and reuptake of template molecules by modified bulk MIPs. The goal of this chapter is to determine a proper procedure for MIPs suitable for making ultrathin films on different substrates. Bulk MIP formation is observed from the Raman spectra of the samples. Bulk NIP formation was also recorded to compare the Raman bands of NIPs and MIPs.

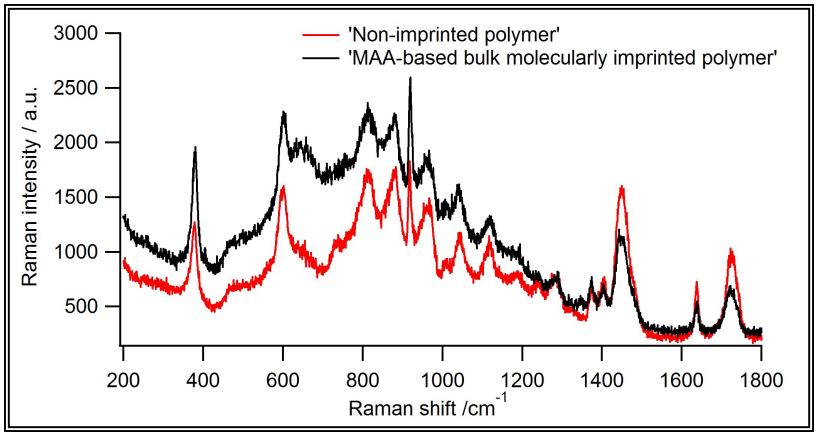

Figure 3.1: Raman spectra of MAA-based bulk non-imprinted and molecularly imprinted polymers

3.2 MAA-based polymer

3.2.1 Raman spectra of the MAA-based bulk MIP and NIP

The observed Raman spectra of the MAA-based bulk molecularly imprinted polymer and non-imprinted polymers are shown in Figure 3.1. The figure indicates that the polymer peaks are obtained at 376, 601, 811, 857, 888, 958, 1042, 1125, 1277, 1288, 1409, 1442, 1454, 1636, and 1722 cm^{-1}. This is consistent with the reported literature spectra [86]. There are small peaks at 712 and 1350 cm^{-1} in the MIP spectrum which do not appear in the NIP spectrum; these match with phenanthrene peaks, as discussed in the next section. The template peaks are not always as strong as in this spectrum; other example spectra are given in Figure A.1 in Appendix A.

3.2.2 Raman spectrum of the template molecule

Figure 3.2 shows the spectrum of solid phenanthrene (the template molecule) against the spectrum for the MIP. Phenanthrene peaks are observed at 251, 397, 410, 443, 501, 548, 586, 618, 712, 763, 791, 827, 832, 875, 1005, 1040, 1143, 1167, 1204, 1243,

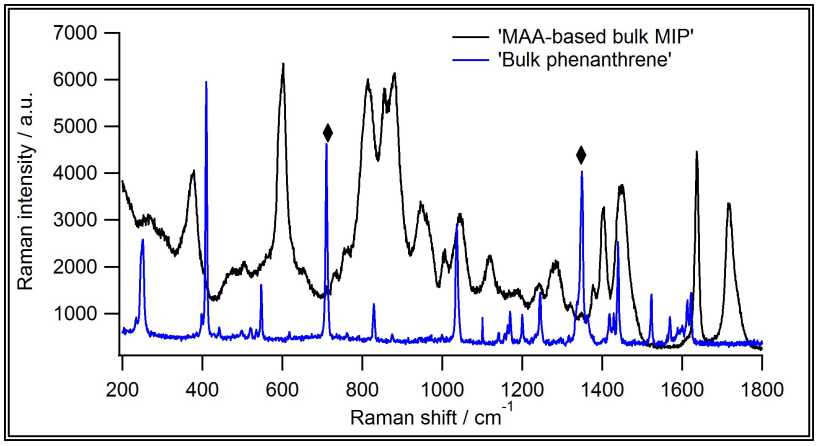

Figure 3.2: Comparison between the Raman spectra of MAA-based bulk MIP and phenanthrene. Diamonds indicate phenanthrene peaks

1304, 1350, 1416, 1425, 1441, 1524, 1570, 1616, and 1624 cm^{-1}. The most intense peaks are at 251, 410, 548, 712, 827, 1040, 1350, 1441, and 1624 cm^{-1}. The medium intensity peaks are at 1143, 1170, 1202, 1243, 1524, 1570, and 1616 cm^{-1}. The rest of the peaks are weak. This is consistent with the reported literature spectra [127]. The peak at 1350 cm^{-1} is assigned to a C-C stretching and HCC bending mode [127]. The peak at 712 cm^{-1} has not been assigned in the literature but it is consistently observed in the solid phenanthrene, MIP-template, and MIP-analyte spectra [127].

3.3 MAA-based polymer with modified procedures

3.3.1 Modified procedure 1

The original procedure for forming the MIP and NIP from the literature was modified as indicated in section 2.1.2, allowing for initial contact between the monomers and the template before addition of the crosslinker and initiator. Initially the solvent (porogen) volume was kept the same as in the original procedure, with this modification denoted modified procedure 1. The characteristic polymer peaks of the NIP

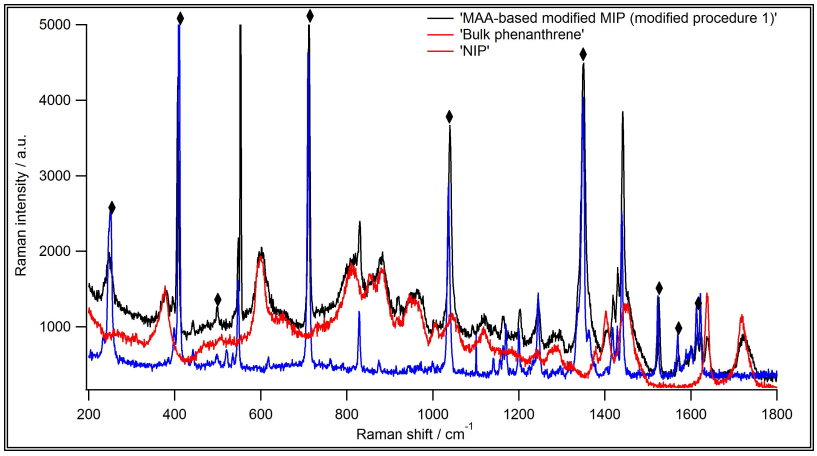

Figure 3.3: Comparison between the Raman spectra of MAA-based modified MIP (modified procedure 1), NIP, and phenanthrene. Diamonds indicate phenanthrene peaks

appear at 376, 601, 811, 857, 888, 958, 1042, 1125, 1277, 1288, 1409, 1442, 1454, 1636, and 1722 cm^{-1} as seen for the original polymer preparation procedure. Those same polymer peaks are seen for the MIP. Additional peaks in the MIP spectrum at 251, 410, 548, 712, 1040, 1350, 1524, 1570, and 1616 cm^{-1} are attributed to phenanthrene. The peaks at 410 and 548 cm^{-1} are assigned to CCC bending [127]. The very strong peaks at 1040 and 1350 cm^{-1} are assigned to C-C stretching and HCC bending, respectively [127]. The medium intensity peaks at 1570 and 1616 cm^{-1} are assigned to C-C stretching [127]. The other indicated peaks at 251, 712, and 1524 cm^{-1} are not assigned in the literature but they are observed consistently in the MIP-template, MIP-analyte and phenanthrene spectra [127].

3.3.2 Modified procedure 2

A second modification was tested, with the same pre-mixing of the template with monomer but with a lower overall solvent volume. The characteristic polymer bands are present at 376, 601, 811, 857, 888, 958, 1042 1125, 1277, 1288, 1409, 1442, 1454, 1636, and 1722 cm^{-1}, matching the bands seen in the previous procedures. Alongside

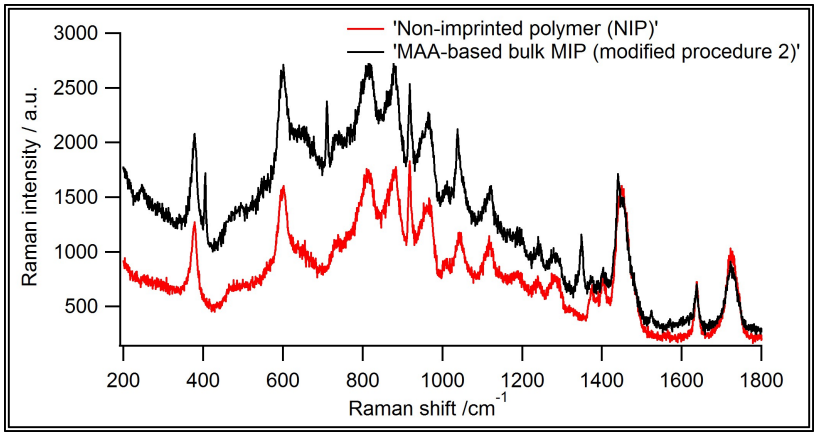

Figure 3.4: Raman spectra of MAA-based modified MIP (modified procedure 2) and NIP

the NIP spectrum in Figure 3.4 is that of the corresponding MIP, with characteristic polymer peaks at the same position. Template peaks (phenanthrene) are observed at 407, 712, 1040, 1350, and 1524 cm^{-1}.

3.3.3 Comparison between modified procedures 1 and 2

Figure 3.5 shows the comparison between the Raman spectra of MAA-based modified MIPs with procedures 1 and 2. The characteristic polymer peaks and the phenanthrene peaks of the two MIPs are observed at the same position.

3.4 Evaluation of procedure modifications

It can be seen from Figure 3.1 that most peaks originated from MAA-based bulk MIP and NIP are the same. The template peaks are not very strong, and measurements taken in different places of the MAA-based MIP show different template. For example, Figure 3.1 shows only very small peaks for phenanthrene whereas Figure 3.2 and Figure A.1 show several peaks for phenanthrene.

There may be two reasons behind this phenomenon. First, the functional monomer

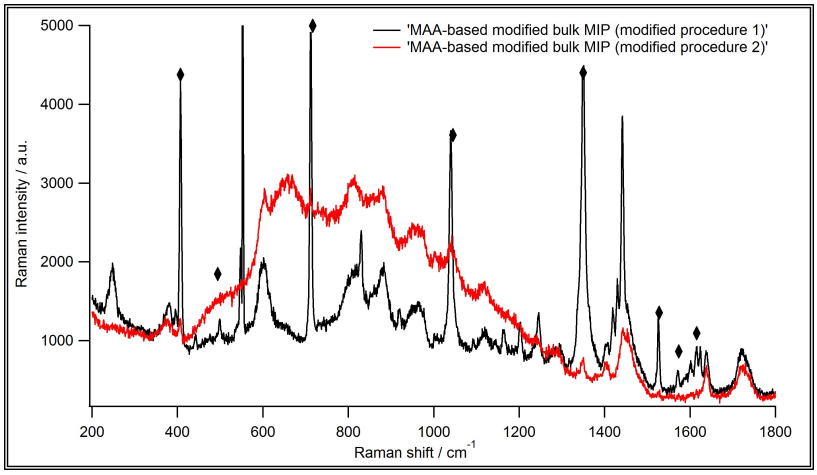

Figure 3.5: Comparison between the Raman spectra of MAA-based modified MIPs with procedures 1 and 2. Diamonds indicate phenanthrene peaks

and the template did not react properly, and therefore the incomplete complexation between the template and the functional monomer was formed in the prepolymerization mixture solution. As a result, good interactions between the functional monomer and the template, a fundamental condition to obtain potential recognition or binding sites in the MIP polymer matrix, was not present everywhere in the bulk polymer. The presence of good monomer-template interactions in the prepolymerization mixture is important in order to maintain the quality and quantity of molecularly imprinted polymer recognition sites (template molecules) in the polymer matrix [61, 63].

Second, the excitation laser for the Raman did not penetrate the entire sample. Though the polymer was placed on a glass slide when the Raman spectra was taken, the glass fluorescence was not observed, meaning that the laser did not go through the bulk MIP. If the template is not distributed evenly throughout the MIP sample, some of the spectra may reflect a region of the MIP where no template is present. Therefore, the laser would not identify any peaks of the template.

The presence of template molecules in the MAA-based modified bulk MIP (mod-

ified procedure 1) can be seen from Figure 3.3. This spectrum confirms the formation of the MIP (with template) as well as the NIP. The different mixing process for this MAA-based modified MIP (modified procedure 1) improves the formation of the MIP because the functional monomer and the template have additional time to interact. As a result, there may be more and more evenly distributed complexation between the template and the functional monomer in the pre-polymerization mixture. Therefore, the Raman spectra show easily identified peaks of the template.

This is also true for the formation of MAA-based modified bulk MIP (modified procedure 2). However, while Figure 3.5 shows that the intensity of most of the polymer peaks of the two MIPs are relatively the same, the intensity of the template peaks (phenanthrene) of MAA-based modified bulk MIP (modified procedure 1) are higher than that of MAA-based modified bulk MIP (modified procedure 2). The use of different volume of solvent while making these two MIPs may be the reason for the phenomenon.

Volume of the solvent plays an important role in the formation of bulk MIP [63]. The creation of large pores which is required to assure good flow through properties in the macroporous polymers depends on the volume of the solvents. Increasing the volume of solvents enlarges the pore volume which can provide good flow through of the solution in the polymer matrix [63]. This may be the reason for the higher intensity of the template peaks of modified procedure 1.

Since MIPs made with modified procedure shows better template signal,therefore, the removal and reuptake study is further carried out considering the MIPs made with modified procedure. The significant template/analyte peaks used for determining the presence of the template/analyte during removal and reuptake are 548, 712, 1040, and 1350 cm^{-1}.

Table 3.1: Template removal from MAA-based modified bulk MIP (modified procedure 1)

Template peak (cm^{-1})	Before washing	After washing		
		4×	8 ×	17 ×
548	1.3(0.14)	1.9(0.36)	2.0(0.25)	2.3(0.26)
1040	2.1(0.13)	2.4(0.22)	2.4(0.10)	2.6(0.27)
1350	2.5(0.08)	1.9(0.09)	1.8(0.23)	1.6(0.05)

3.5 Removal and reuptake template of MAA-based modified bulk MIPs (modified procedures 1 and 2)

The template was removed from MAA-based modified bulk MIP (modified procedure 1) by rinsing with acetonitrile as described in experimental chapter. Table 3.1 and Figure 3.6 show the changes of the intensity of average (standard deviation) scaled peaks of the template after removing the template (phenanthrene) from the MAA-based modified bulk MIP (modified procedure 1). The scaled peaks are relative Raman intensities. Template peaks are divided by the polymer peak at 1636 cm^{-1}. Only one peak of the template gradually decreases after washing the bulk MAA-based MIP. For example, the scaled peak intensity of 1350 cm^{-1} is 2.5 (0.08) before washing and 1.6 (0.05) after washing 17 times.

The changes of the intensity of average (standard deviation) scaled peaks of the template after reuptaking the template (phenanthrene) is summarized in Table 3.2 and Figure 3.7. The concentration of the template solution is 1.6 ppm. Only one peak of the template gradually increases after immersion of the MAA-based modified bulk MIP (modified procedure 1) into the aqueous phenanthrene solution. For example, the scaled peak intensity of 1350 cm^{-1} is 1.6 (0.05) before immersion and 2.1 (0.21) after 18 mins of immersion.

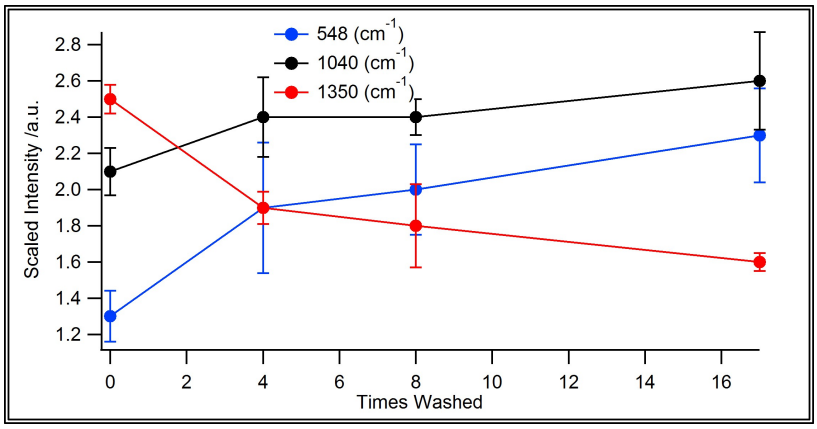

Figure 3.6: Graph of the average scaled peak intensity of the template versus times washed for the MIP prepared with modified procedure 1.

Table 3.2: Template reuptake of MAA-based modified bulk MIP (modified procedure 1)

Template peak (cm^{-1})	17 × washed	9 min immersion	18 min immersion
548	2.3(0.26)	2.3(0.23)	1.6(0.08)
1040	2.6(0.27)	2.8(0.03)	2.2(0.13)
1350	1.6(0.05)	2.0(0.19)	2.1(0.21)

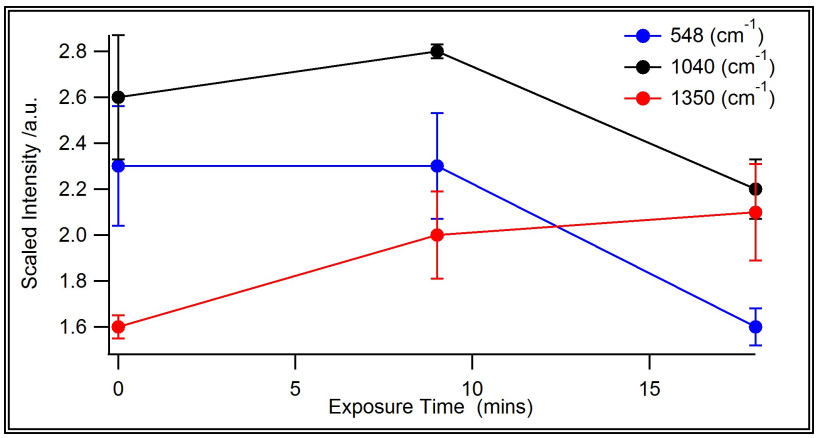

Figure 3.7: Graph of the average scaled peak intensity of the template versus exposure times for the MIP prepared with modified procedure 1.

Table 3.3: Template removal from MAA-based modified bulk MIP (modified procedure 2)

Template peak (cm^{-1})	Before washing	After washing		
		2 ×	4 ×	18 ×
712	3.8(0.43)	3.6(0.26)	2.8(0.96)	2.8(0.60)
1040	3.0(0.35)	2.9(0.14)	2.8(0.07)	2.6(0.24)
1350	1.3(0.13)	1.3(0.28)	1.2(0.22)	1.0(0.17)

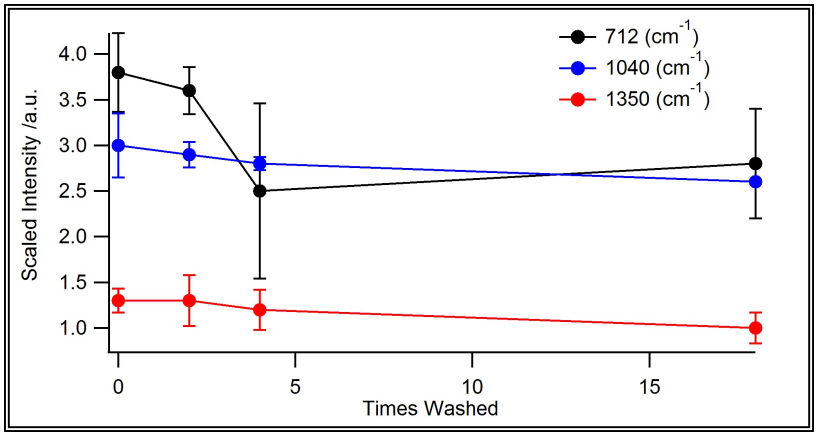

Figure 3.8: Graph of the average scaled peaks intensity of the template versus times washed for the MIP prepared with modified procedure 2.

The other peaks at 548 and 1040 cm^{-1} show counterintuitive results for removal and reuptake process of the template.

Removal of the template was also done with MAA-based modified bulk MIP (modified procedure 2). Table 3.3 and Figure 3.8 show the changes of the intensity of average (standard deviation) scaled peaks of the template after removing the template (phenanthrene) from the MAA-based modified bulk MIP (modified procedure 2). In this case, three peaks of the template gradually decrease after 18 times washing the bulk MIP. For example, the scaled peak intensities of 1350, 1040, and 712 cm^{-1} are respectively 1.3 (0.13), 3.0 (0.35), and 3.8 (0.43) before washing and 1.0 (0.17), 2.63 (0.24), and 2.76 (0.60) after washing 18 times.

The changes of the intensity of average (standard deviation) scaled peaks of the template after reuptaking the template (phenanthrene) is summarized in Table 3.4

Table 3.4: Template reuptake of MAA-based modified bulk MIP (modified procedure 2)

Template peak (cm^{-1})	18 × washed	10 min immersion	45 min immersion
712	2.8(0.60)	3.0(0.16)	3.1(0.34)
1040	2.6(0.24)	2.8(0.14)	2.7(0.44)
1350	1.0(0.17)	1.3(0.08)	1.4(0.25)

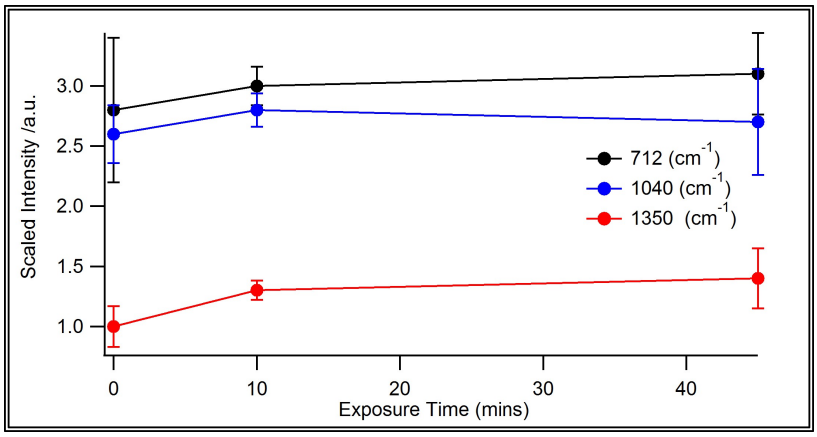

Figure 3.9: Graph of the average scaled peaks intensity of the template versus exposure times for the MIP prepared with modified procedure 2.

and Figure 3.9. The scaled peak intensities of the template gradually increase after 45 mins immersing the MAA-based modified bulk MIP (modified procedure 2) into aqueous phenanthrene solution. For example, the scaled peaks intensities of 1350, 1040, and 712 cm^{-1} are respectively 1.0 (0.17), 2.6 (0.24), and 2.8 (0.60) before exposure and 1.4 (0.25), 2.7 (0.44), and 3.1 (0.34) after 45 mins of immersion.

3.6 Discussion

It can be seen from Figure 3.6 and Figure 3.7 that there is disorder between peak intensities of the template after removing and reuptaking the template from MAA-based modified bulk MIPs (modified procedures 1). Only the peak at 1350 cm^{-1} gradually decreases after removing and increases after uptaking the template. This bulk MIP polymer matrix has non-covalently bonded binding sites. The common

disadvantage of the non-covalently bonded binding sites is that the population of the binding sites are heterogeneous [57]. This is created by random co-polymerization of a cross-linker and template-functional monomer complexes. As a result, the polymer chains around the template are aligned in different ways and there is no control over it [128]. These different ways are also responsible for forming different cross-linking densities around the binding sites, thus resulting in different degrees of accessibility which could create different kinds of binding sites [128]. Another reason is that some of the peaks can overlap with the NIP peaks. For instance, this bulk MIP has the peak at 1040 cm^{-1} which can overlap with the NIP peak at 1042 cm^{-1}. There is no peak for polymers at the range of 1300 cm^{-1}. Therefore the peak at 1350 cm^{-1} can be a unique peak for the template in this MIP.

In contrast, it can be seen from Figure 3.8 and Figure 3.9 that there is a positive order of peak intensities of the template after its removal and reuptake. This bulk MIP may have homogeneous binding sites rather than heterogeneous binding sites in the polymer matrix. As a result, there is a positive consistency of the removal and reuptaking of the template from the polymer matrix.

Moreover, there can be another reason for the disordered values of reuptaking the template with MAA-based modified bulk MIP (modified procedure 1). The first solution used for rebinding the template with the bulk MIP was sonicated for 60 mins. Since phenanthrene (template) is hydrophobic, it is only slightly soluble in water. Phenanthrene could not dissolve properly in the first solution with 60 mins of sonication, such that the reuptake experiments for the MIP with modified procedure 1 may have been performed with a lower concentration of phenanthrene than expected. On the other hand, the second solution used for reuptaking the template with the MAA-based modified bulk MIP (modified procedure 2) was sonicated for 240 mins. This may improve the solubility of phenanthrene molecules in the water. This

solubility may provide positive order of the reuptaking the template with MAA-based modified modified bulk MIP (modified procedure 2).

3.7 Conclusion

In this chapter, I present procedures for MIP formation and their evaluation based on better template molecule signal. Bulk MIPs made with my modified procedure show better template signal. In addition, these bulk MIPs show appropriate changes in peak intensities of the template molecule upon removal and reuptake. Based on the results from this chapter, the following chapter focuses on ultrathin films for the original procedure and modified procedure 1 only. Although template peaks of the original procedure (MAA-based bulk MIP) are not always strong, the procedure is used to make ultrathin films to explore the films' morphologies and to measure the films' thicknesses.

Chapter 4

Structural Properties of Ultrathin Films of MIPs

4.1 Introduction

This chapter focuses on the structural properties of the ultrathin films of MIPs. It describes the morphology and roughness of different ultrathin films of MIPs. Ultrathin film MIPs were made using a spin coater to apply two of the different formulations tested for bulk MIPs in Chapter 2. In addition to varying the formulation, the effects of several film formation parameters (spin speed and time, and exposure time) are studied.

4.2 MAA-based ultrathin film MIP on glass and Si

The morphology of MAA-based ultrathin films was recorded. Furthermore, the films' thicknesses were also measured. The films' morphologies, and the films' thicknesses

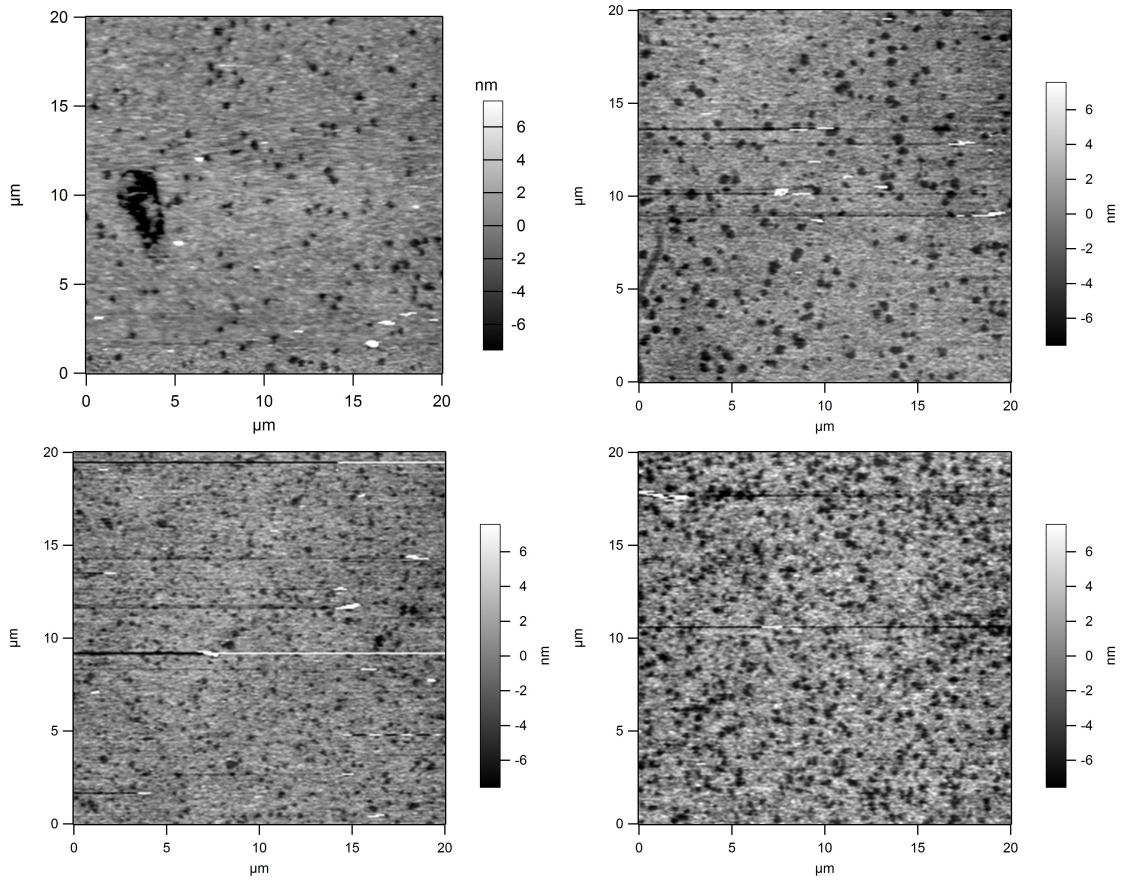

Figure 4.1: AFM morphology of MAA-based ultrathin films prepared by spin coating at a) 1000 rpm, b) 1100 rpm, c) 1800 rpm, and d) 2000 rpm

are described below.

4.2.1 AFM

The morphology of the MAA-based ultrathin films is shown in Figure 4.1. It can be seen from these figures that the films are porous and pores are distributed all over the films. Different MAA-based ultrathin film samples present different pore density.

The roughness of the MAA-based ultrathin film MIPs is shown in the Table 4.1. In this table, there is no order of roughness values of the films with increasing spin speed. Different films have different roughness.

Table 4.1: Roughness of MAA-based ultrathin film MIPs

Sample	Spin Speed (rpm)	Roughness (nm)
1	500	0.0
2	800	4.0
3	1000	1.9
4	1100	4.3
5	1400	3.8
6	1800	3.3
7	2000	3.3

Table 4.2: Surface area of the MAA-based ultrathin film MIPs

Sample	Spin Speed (rpm)	Surface Area (%)	
		Average	Standard Deviation
1	1000	102.6	0.2
2	1100	101.2	0.2
3	1800	104.1	0.3
4	2000	100.1	0.03

Surface area of the MAA-based ultrathin film MIPs is shown in the Table 4.2. It can be seen from this table that the surface area of the films changes with different spin speeds.

While the AFM cannot detect interior pores, for these ultrathin films many pores are exposed to the AFM probe. Figure 4.2 shows the changes of the average (standard deviation) surface area of the MAA-based ultrathin films with increasing spin speed. The surface area is given as a percentage relative to the area of a flat surface, so that a perfectly flat surface would come in at 100 % and rougher and/or more porous films would have an area of higher than 100 %.

AFM section analysis to measure film thickness is illustrated in Figure 4.3. It can be seen from this figure that the film was scratched in two areas. By taking a section across one of these areas, one can measure the depth of the scratched. Note that there is substantial pileup of material at both sides of the scratched area, as seen in both the white areas in the image and in the peaks in the section plot. Therefore,

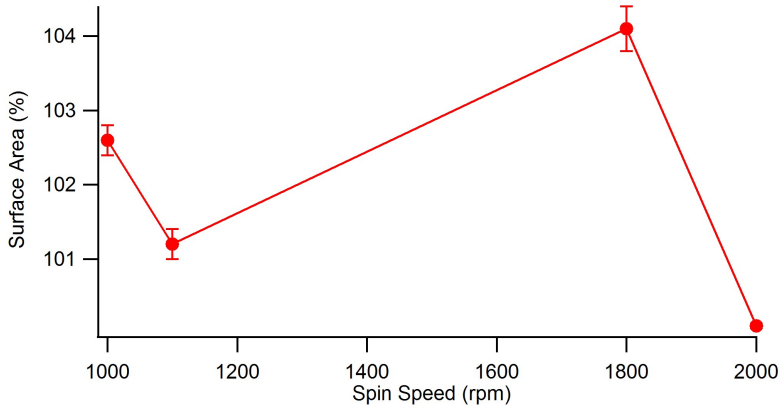

Figure 4.2: Graph of the changes of the surface area of the MAA-based ultrathin films with increasing spin speed

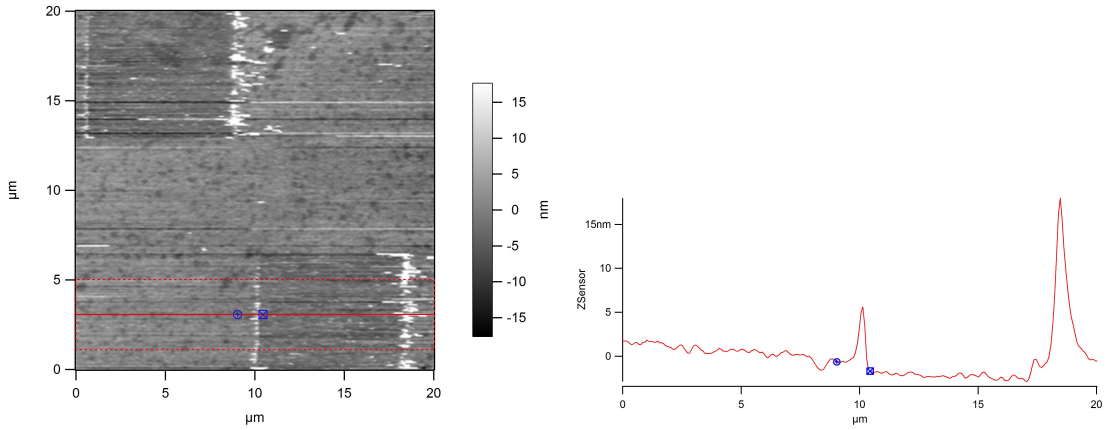

Figure 4.3: AFM section analysis of the MAA-based ultrathin film MIP

when measuring the thickness of the film one must measure from beyond the pileup region, as indicated by the blue markers in the plot.

Table 4.3 and Figure 4.4 show the effect of spin speed on the thickness of the films, with a dramatic drop in thickness when going above 1000 rpm.

Figure 4.5 shows the effect of polymerization conditions on the surface morphology of the few MAA-based ultrathin film MIPs. As can be seen in Figure 4.5, the films have harder layers of polymer. The film was not perfectly scratched after scratching 10 times.

Table 4.3: Thickness of the MAA-based ultrathin film MIPs

Spin Speed (rpm)	Thickness (nm)	
	Average	Standard deviation
1000	18.5	2.1
1100	8.5	4.9
1800	5.5	2.1
2000	4.2	0.8

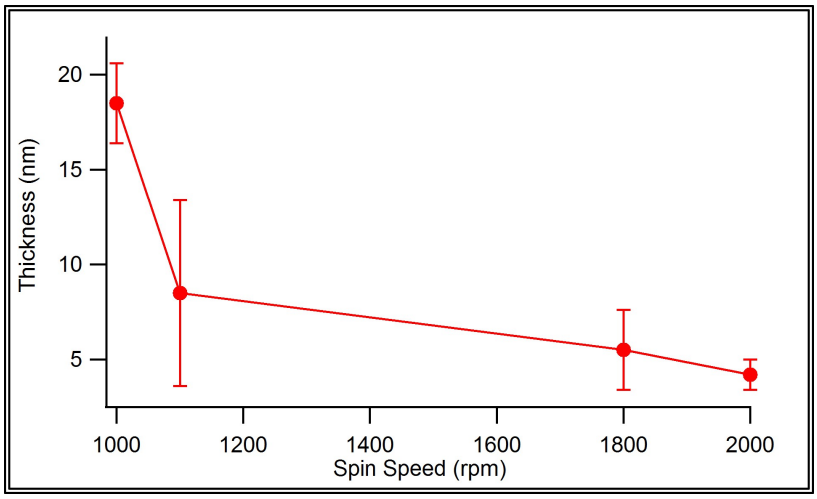

Figure 4.4: Graph of the changes of the thickness of the MAA-based ultrathin film MIPs with increasing spin speed

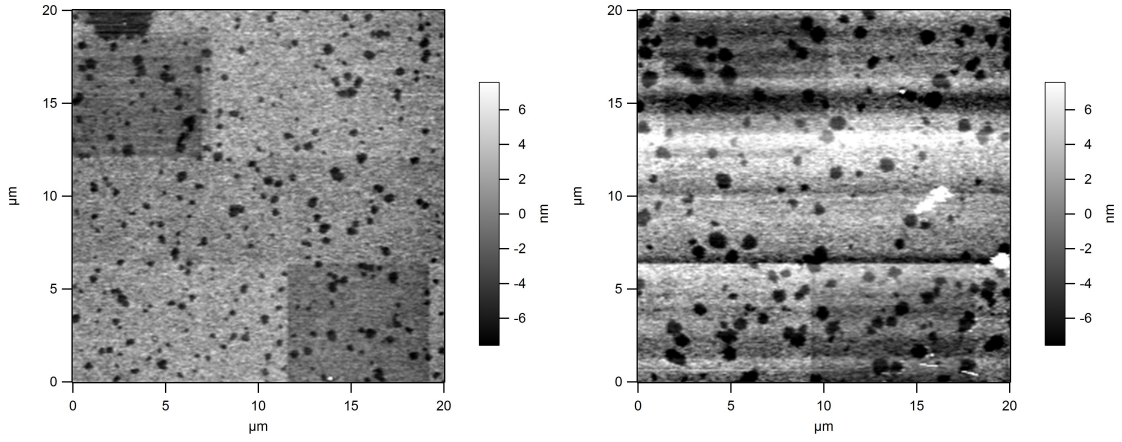

Figure 4.5: The effect of polymerization conditions on the surface morphology of the MAA-based ultrathin film MIPs. Both films were spun at 1000 rpm, and the left film was polymerized by using 400 W EC Silver SERIES UV Light Source Flood Lamp System at 90 °C and the right film was polymerized by using hot plate at 100 °C

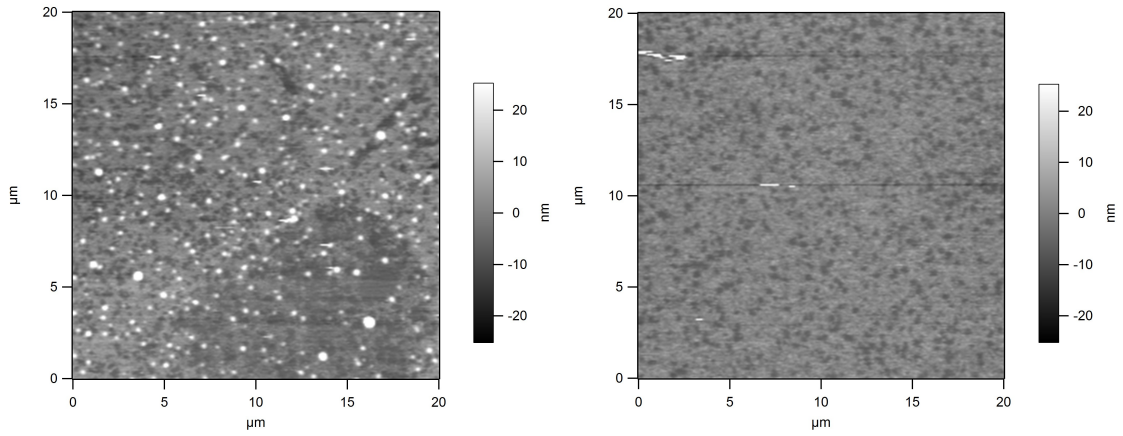

Figure 4.6: The effect of spin speed on the morphology of the films on glass

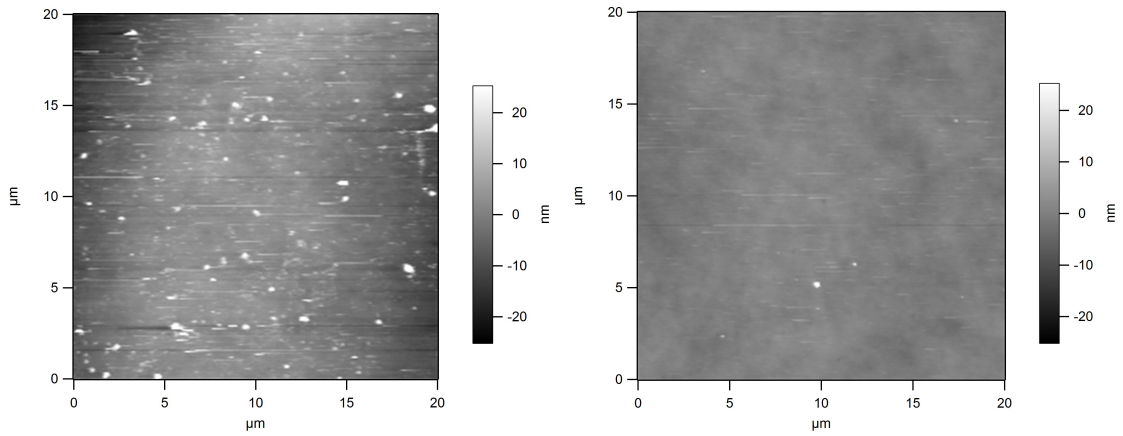

Figure 4.7: The effect of spin speed on the morphology of the films on Si

Figure 4.6 shows the effect of spin speed on the morphology of the films. In this figure, the white regions is defined as surface deposition of template molecules [129]. These films were deposited on the glass slides. This effect is also found for MAA-based ultrathin film MIPs on Si substrates showing in Figure 4.7.

4.2.2 Discussion

The results of the AFM morphology of the ultrathin film show that different spin speeds make the different surface morphology of the films. The spin speeds used for those films are 1000, 1400, 1800, and 2000 rpm. It shows that higher spin speed

provides more uniform pore distribution all over the surface of the film rather than lower spin speed. The roughness results in Table 4.1 show that there is no consistency between the roughness and spin speed. Higher spin speed causes slight decrease in surface roughness. This is consistent with the reported literature [129].

It can be seen from Figure 4.2 that surface area of the ultrathin films changes with increasing spin speed. Different spin speeds produce different surface areas of the films. This is related to film morphology since different spin speeds produce different morphologies. The thickness table and figure also illustrate that spin speed plays an important role in making ultra thin film. Higher spin speed produces ultra thin film. This result is consistent with the reported literature [130, 131].

The surface morphology of the ultrathin film can be affected by the different polymerized conditions. The films shown in Figure 4.5 were spun at 1000 rpm and polymerized by using 400 W EC Silver SERIES UV Light Source Flood Lamp System at 90 °C and hot plate at 100 °C. It is very probable that temperature can affect the surface morphology of the films. The films are thicker and can have a softer top layer which lies on a harder layer. Most of the literature state that polymerization conditions such as temperature plays an important role in making MIP polymer. It is also suggested that relatively low temperatures, around 60 °C with longer reaction times, increase the reproducibility of MIP polymer and the selectivity of the formed binding sites in the polymer [60,61,63,132]. It can also be applicable for ultrathin films because results from the current study shows that temperature affects the physical properties of the thin film. Therefore, higher temperatures make the films harder.

The results of the effect of spin speed on the morphology of the ultrathin films on the glass and Si substrates reveals that the rotation speed plays a significant role in the surface deposition of additional MIP. In Figure 4.6 and Figure 4.7, the left hand side films were spun at 1000 rpm whereas the right hand side films were spun

at 2000 rpm. It shows that lower spin speed yields films with more surface deposition of additional MIP, whereas higher spin speed provides less deposition of additional MIP on the surface. The white regions almost disappear from the surface as higher spin speeds are applied to make the ultrathin films. This result is consistent with the reported literature [129].

4.3 MAA-based modified ultrathin film MIPs (modified procedure 1) on glass

The morphology of MAA-based modified ultrathin films was recorded. Furthermore, the films' thickness were also measured. The films' morphology, and the films' thickness are summarized below.

4.3.1 AFM and profilometer measurements

The morphology of the MAA-based modified ultrathin film is shown the Figure 4.8. It can be seen from this figure that the film is porous and pores are distributed all over the films. The white regions are further MIP deposits on top of the MIP film.

AFM section analysis to measure the thickness of the MAA-based modified MIP ultrathin films is shown in Figure 4.9. The film was scratched by a blade. It can be seen from this figure that the depth of the scratched area was measured.

The height of the film thickness of MAA-based modified MIP ultrathin film was also measured with a profilometer as shown in Figure 4.10.

The thickness measured by AFM and profilometer of some MAA-based modified ultrathin films is shown in Table 4.4 and Figure 4.11. Different films' thicknesses can be obtained by different spin speeds, ranging from 305 nm (200 rpm) to 38 nm (400 rpm).

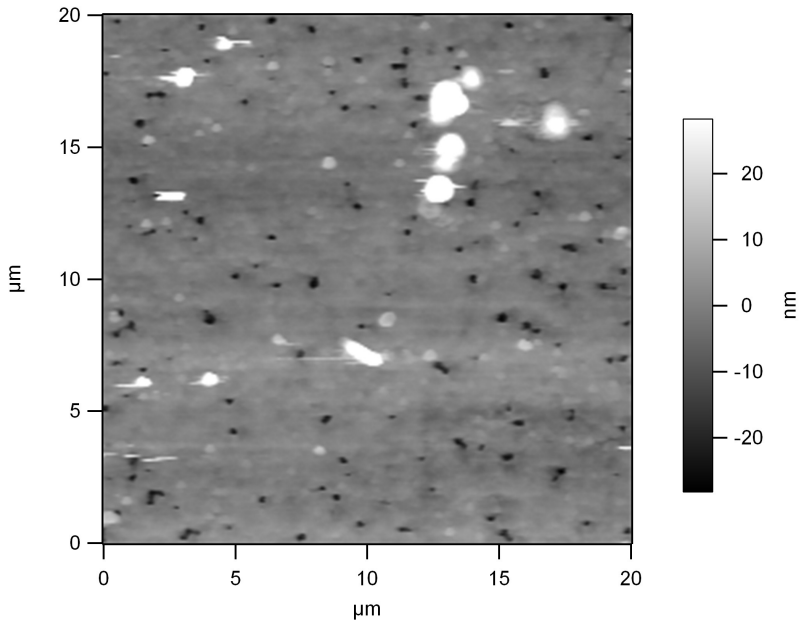

Figure 4.8: The surface morphology of the MAA-based modified MIP thin film on the glass substrate

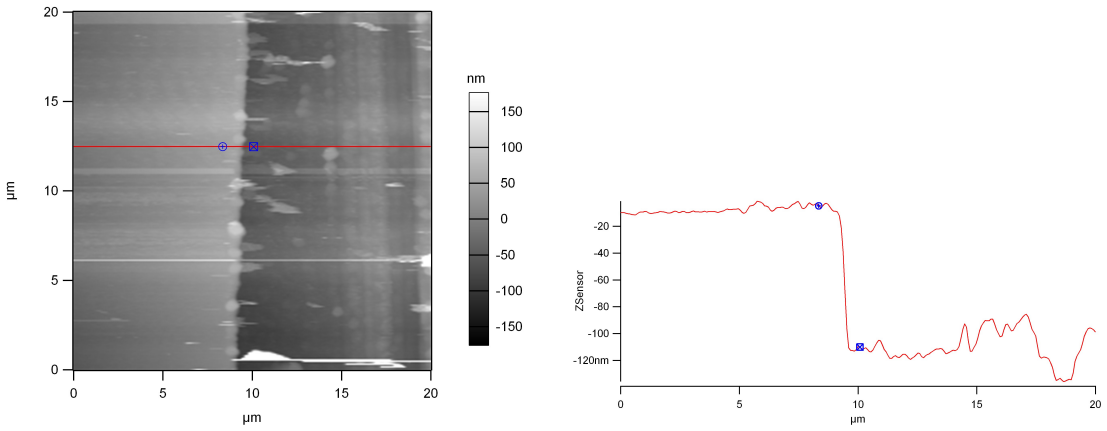

Figure 4.9: AFM section analysis of the MAA-based modified MIP ultrathin film. The red line at left shows the place where the section at right was taken. The height is measured between the blue circle and blue square in the section at right.

Table 4.4: AFM and profilometer thickness of the MAA-based modified MIP ultrathin films.

Spin Speed (rpm)	Average thickness (std. dev.) in nm	
	AFM	profilometer
200	305 (3.5)	303 (46.0)
300	134 (58.6)	156 (42.0)
400	38 (0.7)	41 (10.8)

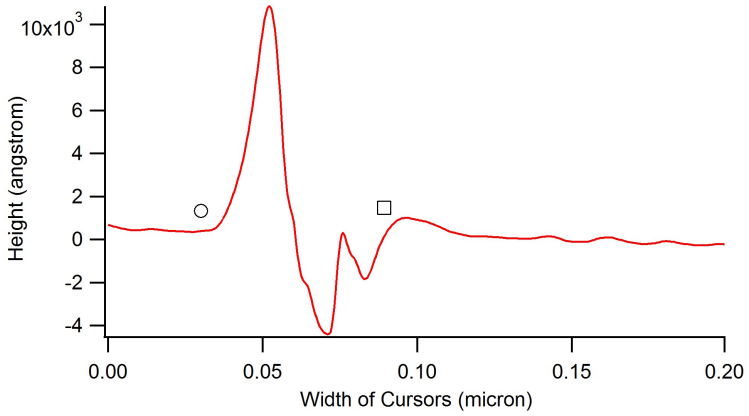

Figure 4.10: Cross section of the surface of the MAA-based modified MIP ultrathin film on the glass substrate. The height is measured between the circle and square in the section at right.

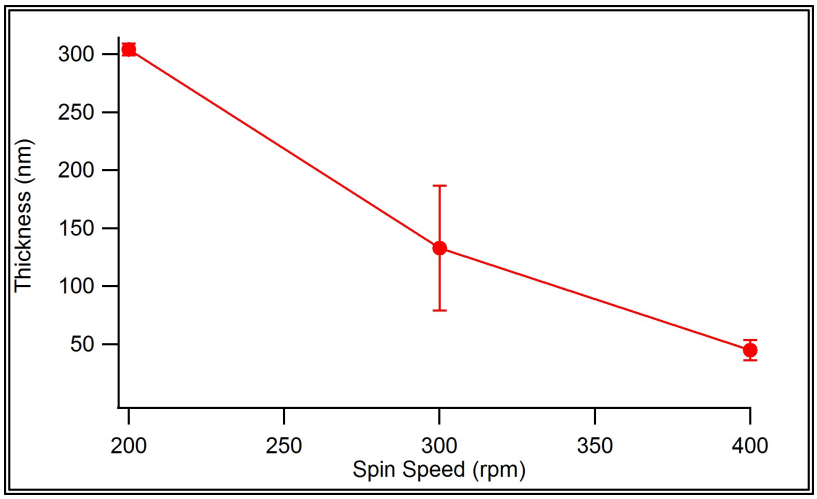

Figure 4.11: Graph of the thicknesses of the MAA-based modified MIP ultrathin films with increasing spin speed

4.3.2 Discussion

Table 4.4 and Figure 4.11 show that higher spin speed produces thinner film. Moreover, it is also shown that the thickness of the films measured by AFM and profilometer are relatively similar.

4.4 Conclusion

Based on the discussion from this chapter, different surface morphology of the ultrathin films of MIPs are produced by using different spin speeds and time, and exposure time. For example, higher spin speed provides more uniform pore distribution all over the surface of the film rather than lower spin speed; higher spin speed produces thinner film; higher temperatures make the films harder; and higher spin speed provides less deposition of additional MIP on the surface, whereas lower spin speed produces films with more surface deposition of additional MIP. Building on the results from this chapter, the following chapter focuses on the making of ultrathin films of MIPs on different substrates. This includes the characterization of ultrathin films of MIPs and substrate modification methods.

Chapter 5

Spectroscopic Characterization of Ultrathin Films of MIPs

5.1 Introduction

This chapter focuses on the making of ultrathin films of MIPs on different substrates. It also characterizes the formation of ultrathin film MIPs and determines the sensing parameters of template removal and reuptake for ultrathin film MIPs using a spectroscopic method. To make MAA-based bulk MIP and MAA-based modified bulk MIP (modified procedure 1) as an ultrathin film, several substrates were used, starting with glass and Si wafers. Substrate modifications are used to reduce the fluorescence of some substrates such as glass and Si wafers.

5.2 MAA-based ultrathin film MIP on glass

The Raman spectrum of MAA-based ultrathin film MIPs was recorded. The Raman spectrum is described below.

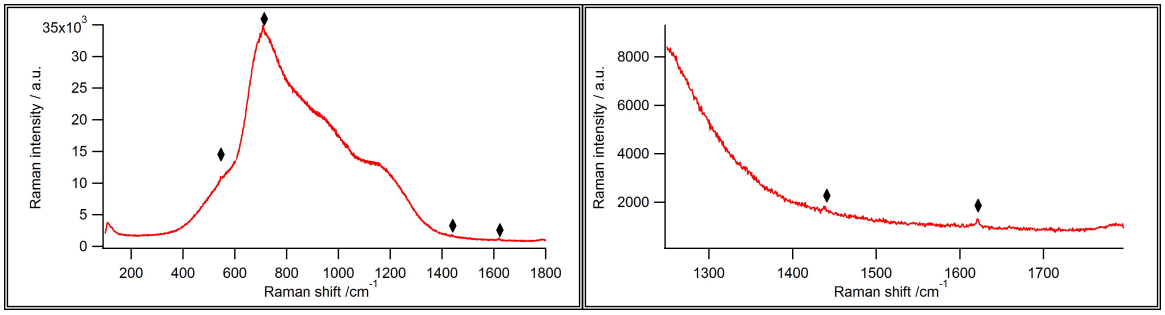

Figure 5.1: Raman spectrum of an MAA-based ultrathin film MIP, with a zoom of the spectrum at right. Diamonds indicate phenanthrene peaks.

5.2.1 Raman Spectroscopy

The first step in developing ultrathin film MIPs is to confirm that the polymerization occurs properly even under non-bulk conditions. For example, solvent evaporation is quite different than in the bulk or in bulk-like thicker films [133] given the much larger surface area-to-volume ratio. Raman spectroscopy indicates that the MIP forms even in this new format, as shown in Figure 5.1. Although the spectrum is influenced by the glass fluorescence, some of the peaks can be assigned for the film at approximately 548, 712, 1442, and 1622 cm^{-1}. The peaks at 1442 and 1622 cm^{-1} are more apparent in Figure 5.1 at right. The peak at 548 cm^{-1} is assigned to CCC bending [127]. The peak at 1620 cm^{-1} is assigned to C=C stretching vibration [127]. The peak at 712 cm^{-1} is not assigned in the literature but it is consistently observed in the solid phenanthrene, MIP-template, and MIP-analyte spectra [127]. The peak at 1442 cm^{-1} is a polymer peak.

5.2.2 Discussion

Figure 5.1 shows the formation of MAA-based ultrathin film MIP on the glass. The ultrathin film MIP has some of the template peaks. Also, one polymer peak is observed at 1442 cm^{-1} whereas other polymer peaks are not observed. The spin speed used for

making this thin film is 800 rpm. It is stated in the literature that the spin coating mechanism can play an important role in making the final surface of the film [130]. Therefore, proper testing of spin coating is required. The spin speed used in this study may change the orientation of the monomer and template binding sites, and the template may persist at the surface of the film. Since the film was transparent, the laser went through the film. As a result, the spectra show a higher intensity of the glass fluorescence. The other polymer and template peaks were not observed for this reason.

5.3 MAA-based ultrathin film MIPs (modified procedure 1)

The Raman spectra of MAA-based modified ultrathin film MIPs were recorded to confirm the formation of the MIP under these new (spin-coated) conditions. Spectra were acquired for films on glass and Si substrates. The Raman data are summarized below.

5.3.1 Raman Spectroscopy

The observed Raman spectra of a few MAA-based modified ultrathin film MIP on the glass slides are shown in Figure 5.2. Characteristic main polymer peaks are present at approximately 376, 601, 811, 857, 888, 958, 1125, 1277, 1288, 1409, 1442, 1454, 1636, and 1722 cm^{-1}. The peaks indicated with diamonds are for the template molecule. The indicated peaks are observed at 251, 410, 548, 712, 1040, 1350, and 1524 cm^{-1}. The peaks at 410 and 548 cm^{-1} are assigned to the CCC bending [127]. The very strong peaks at 1040 and 1350 cm^{-1} are assigned to the C-C stretching and HCC bending, respectively [127]. The other indicated peaks at 251, 712, and 1524 cm^{-1}

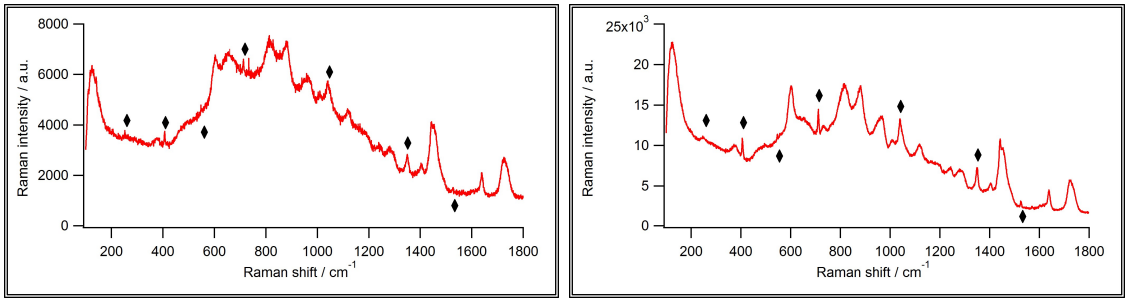

Figure 5.2: Raman spectra of MAA-based modified ultrathin film MIPs. The left film was made using 400 rpm spin speed and 300 s exposure time. The right film was made using 500 rpm spin speed and 300 s exposure time. Diamonds indicate phenanthrene peaks.

are obtained from matching to the solid phenanthrene spectrum [127].

Checking the Raman spectra of these MIP polymer films on the glass was very difficult because of the fluorescence of the glass. Therefore, the films were scratched off of the glass to check the spectra in order to ensure the formation of the films. The Raman spectrum of one film was able to be taken without scratching the film out of the glass surface and is shown in Figure 5.3. The characteristic main polymer peaks and the template peaks are present in this polymer film. The template peaks are indicated in the figure with the small black diamonds .

Figure 5.4 shows the Raman spectrum of the formation of a MAA-based MIP modified ultrathin film on a Si substrate. The presence of the characteristic polymer peaks and template peaks are indicated in the picture. Since the intensity of the Si peak (520 cm^{-1}) is higher than that of the polymer and template peaks, another graph with a different range of Raman shift is shown at right in Figure 5.4 to see the peaks clearly. Some of the polymer peaks and template peaks of this range are indicated with symbols.

Figure 5.5 shows the formation of MAA-based modified ultrathin film MIPs. This is the one example of the formation of the ultrathin films on the Si substrates.

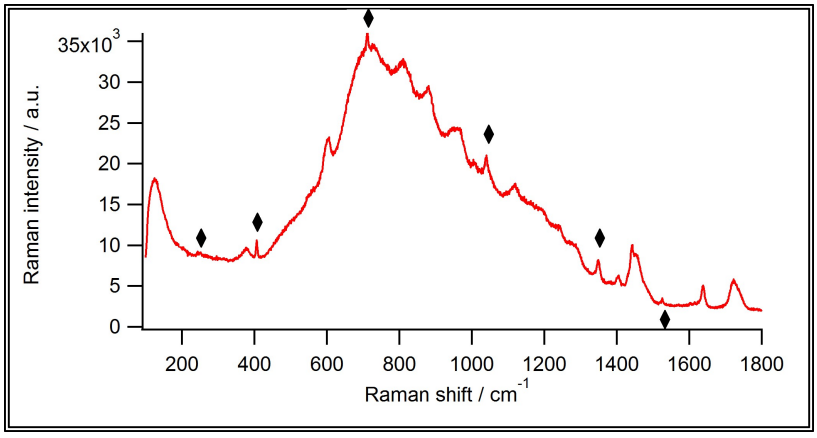

Figure 5.3: The Raman spectrum of a MAA-based modified ultrathin film MIP on glass. The film was made using 100 rpm spin speed and 60s exposure time. The broad envelope is due to glass fluorescence, but MIP and template peaks are clearly visible. Diamonds indicate phenanthrene peaks.

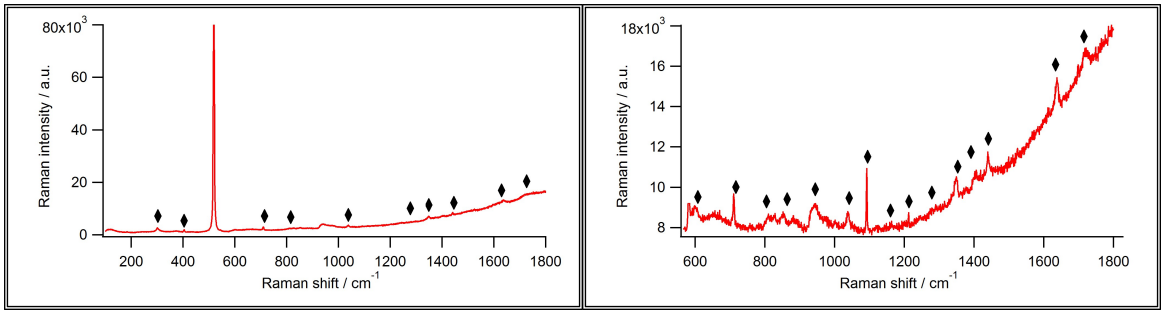

Figure 5.4: The Raman spectrum of a MAA-based modified ultrathin film MIP observed on Si, with a zoom of the spectrum at right. Diamonds indicate phenanthrene peaks.

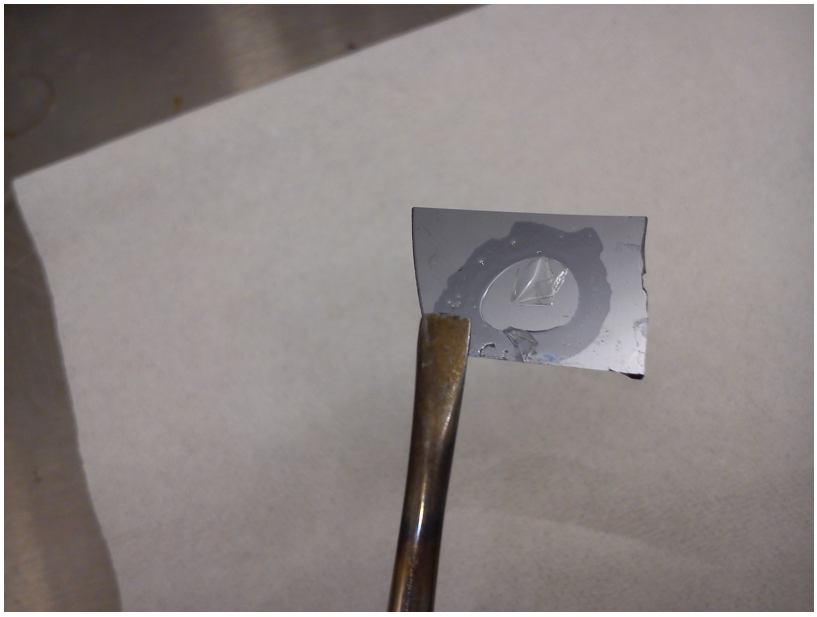

Figure 5.5: A photograph showing the formation of a MAA-based modified ultrathin film MIP on a Si substrate. The Si chip is approximately 2.5×1.8 cm^2 in size.

5.3.2 Discussion

The results obtained from several MAA-based modified ultrathin film MIPs indicate that the films were formed on the glass substrate. Since the glass has high fluorescence, the films were scratched off of the glass to check the peaks of these thin films, and placed on an Al wrapped glass slide. The baseline of the Raman spectra of the two films is slightly higher, however the peaks are considerably visible. The difference of the Raman intensity of the films can originate from the different focusing of the films.

In Figure 5.3, the Raman spectra show MAA-based modified ultrathin film MIP (modified procedure 1) was formed on the glass slide. The film was spun at 100 rpm for 60 sec. The template peaks and the polymers peaks are visible on the glass with the big fluorescence. Note that lower spin speed makes thicker films. Since the film was very thick, the peaks were visible with the presence of the glass fluorescence. The problem of the thick film was that crack formed on the film once being made. This result indicates the instability of the thicker films.

Figure 5.4 shows the Raman spectrum of the film on the Si substrate, spun at 200 rpm for 30 sec. The problem of the film was that it did not form on the whole surface of the Si substrates. The film was formed in one place as delamination occurs. Figure 5.5 shows the delaminated film on the Si substrate. The reason for the delaminated film can be the weak interfacial bond strength between the Si surface and MIP polymer surface. Since the film was not attached to the Si surface, improvement of wettability of the substrate surface is necessary to enhance the adhesion layer between the MIP and substrate. A previous study [94] shows that silanization can be used to improve the wettability of the Si substrates and to enhance adhesion layer by introducing polymerizable groups onto the Si surface. Also, oxygen plasma treatment can increase the wettability of the substrates [134, 135].

To make MIP as an ultrathin film, we have to worry about substrate effects, such as the fluorescence which can swamp the signal (described in section 5.2.2) and the wetablity of the substrates (described in section 5.3.2). Therefore, substrates need to be modified before depositing MIP as an ultrathin film. Substrate modifications are described in the next section.

5.4 Substrate selection

The substrate used to support a thin film can greatly impact its functionality [134]. In this thesis I focus on two main features of substrate selection and preparation: pre-treatments to improve the interaction between the substrates and the MIP, and substrate modifications which can reduce the fluorescence of some substrates. The results of the substrate selection to support the MIP as an ultrathin film are presented below.

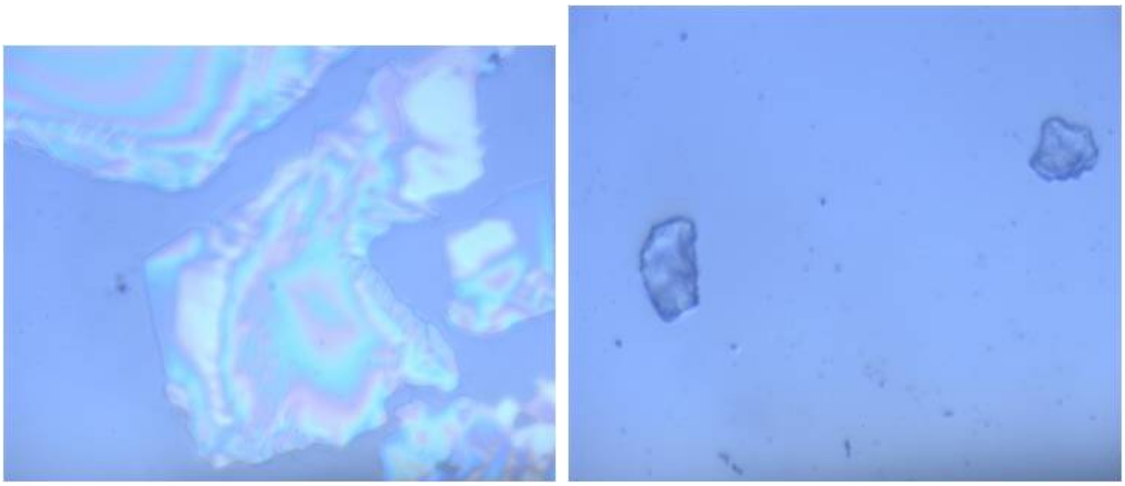

Figure 5.6: Optical micrographs of ultrathin MIP films on untreated (left) and plasma treated (right) glass slides. The images 300×200 microns in size.

5.4.1 Plasma treatment for improved wettability

Exposure of glass and Si to an oxygen plasma increases its hydrophilicity [134, 135]. The result of the improvement of wettability of the substrate surface is shown in Figure 5.6. The left hand side picture shows MIP islands on an untreated substrate. These arise from poor wetting of the substrate during the initial precursor solution deposition prior to spin coating, and from subsequent delamination and cracking during and after delamination. In contrast, the right hand side picture shows the improvement of the MIP film on a substrate which has been plasma treated. During the deposition of the precursor solution for spin coating, the increased wettability was immediately evident. The resulting film is also clearly more uniform and does not show cracks. The two objects visible in the micrograph are contaminant particles; a view was selected which showed these objects to facilitate visualization. A clean area appears "blank" because the film quality is so good. The presence of MIP was confirmed by Raman, as shown in Figure 5.2.

5.4.2 Fluorescence suppression: PDMS coatings

Both glass slides and Si wafers are convenient and relatively low cost substrates for preparing thin films. However, they both show significant fluorescence signals when excited with an 830 nm laser, as seen in Figure 5.7. In the case of glass, the fluorescence appears as a large envelope over the range of 600 to 1400 cm^{-1}. For Si, the fluorescence appears as a broad peak from 1500 to 2700 cm^{-1}. This is a significant problem, swamping the Raman signal from the film and the analyte.

The first approach tested to suppress this fluorescence was to apply a thin film of polydimethylsiloxane (PDMS) to the substrate before spin-coating any MIP films. The Raman spectrum of PDMS on glass substrates is shown in Figure 5.8. The Raman bands of PDMS are observed at 488, 617, 687 709, 786, 860, 1263, and 1412 cm^{-1}. The peak at 488 cm^{-1} is assigned to Si-O-Si symmetric stretching [136]. The peak at 687 cm^{-1} is assigned to Si$-CH_3$ symmetric rocking [136]. The peak at 709 cm^{-1} is assigned to Si-C symmetric stretching [136]. The peak at 786 cm^{-1} is assigned to CH_3 asymmetric rocking and Si-C asymmetric stretching [136]. The peaks at 860 cm^{-1} is assigned to CH_3 symmetric rocking [136]. The peak at 1263 cm^{-1} is assigned to CH_3 symmetric bending [136]. The peak at 1412 cm^{-1} is assigned to CH_3 asymmetric rocking [136]. Although the peak at 617 cm^{-1} is not present in the literature, it is observed for PDMS in the main Raman spectrum.

Figure 5.8 contains Raman spectra for glass slides with different thicknesses of PDMS. The different thicknesses are achieved by changing spin speed, with a higher spin speed corresponding to a thinner film. The spin curve for PDMS is provided in Figure A.4 in Appendix A.2.

Not surprisingly, a thicker PDMS film suppresses more fluorescence: the spectrum in Figure 5.8 with the lowest spin speed shows the clearest PDMS features and none of the fluorescence envelope observed in Figure 5.7. Similar effects are observed on

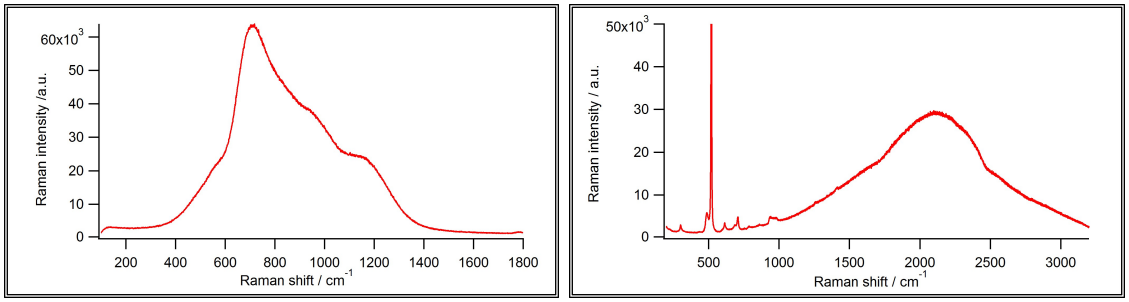

Figure 5.7: Raman spectra of glass (left) and Si (right) substrates showing the strong fluorescence signal when excited with an 830 nm laser.

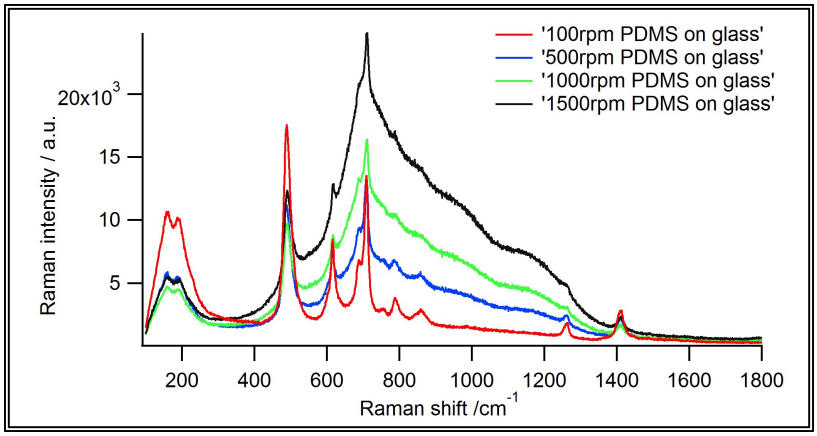

Figure 5.8: Raman spectra showing the effect of different thicknesses of the PDMS films on the reduction of fluorescence emission from the glass substrate.

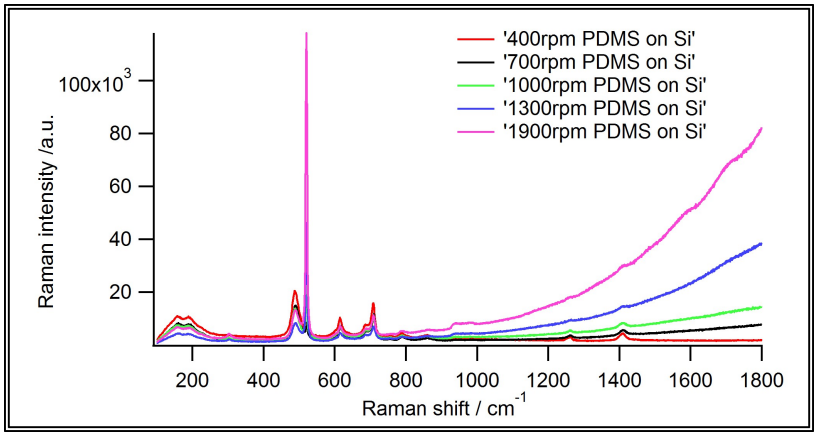

Figure 5.9: Raman spectra showing the effect of different thicknesses of the PDMS films on the reduction of fluorescence emission from Si substrate.

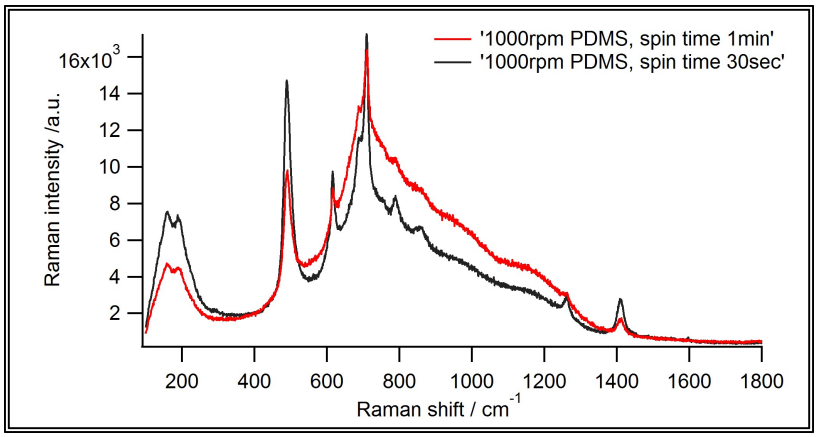

Figure 5.10: The effect of different spin times of the PDMS films on the detection of the glass fluorescence.

Si substrates, as shown in Figure 5.9. Si fluorescence is suppressed with the thickest PDMS film (lowest spin speed), with more fluorescence apparent for Si substrates with thinner PDMS films (higher spin speeds).

Spin time also makes a difference. Figure 5.10 shows spectra for PDMS films on glass prepared at the same spin speed for for 30 seconds vs 1 minute. The red spectrum was spun at 1000 rpm for 1 min whereas the film with the black spectrum was spun at 1000 rpm for 30 sec. The shorter spin time lead to clearer film peaks and reduced fluorescence.

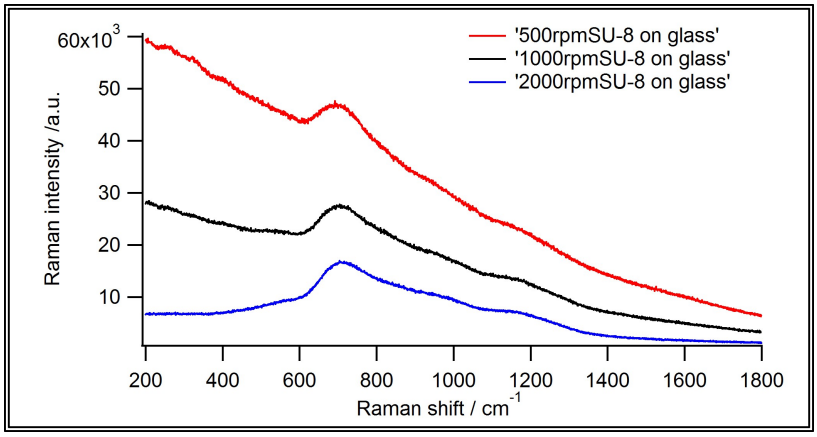

Figure 5.11: Raman spectra showing the effect of different thicknesses of the SU-8 films on the reduction of fluorescence emission from glass substrate.

5.4.3 Fluorescence suppression: photoresist coatings

As a second approach to fluorescence suppression, I evaluated two different photoresist films, SU-8 and S1813, at different thicknesses. For the purposes of this study, the primary difference between these two is viscosity and hence the thickness range which can be achieved. Spin curves for these two materials are provided in Figure A.2 and Figure A.3 in Appendix A.1. The Raman spectra of three thicknesses of SU-8 on glass substrates is shown in Figure 5.11. Figure 5.12 shows the three thicknesses of SU-8 on Si substrates. Thicker SU-8 films do suppress the fluorescence somewhat, but there is still significant fluorescence (note the large scale on the vertical axis).

Figure 5.13 shows the Raman spectra of S1813 on the glass substrates. The figure compares the thickness of S1813 films on the glass substrates with the reduction of fluorescence of the glass substrate. Figure 5.14 shows the Raman spectra of s1813 films on the Si substrates. The figure indicates the relation between the thickness of SU-8 films and the fluorescence of Si substrate.

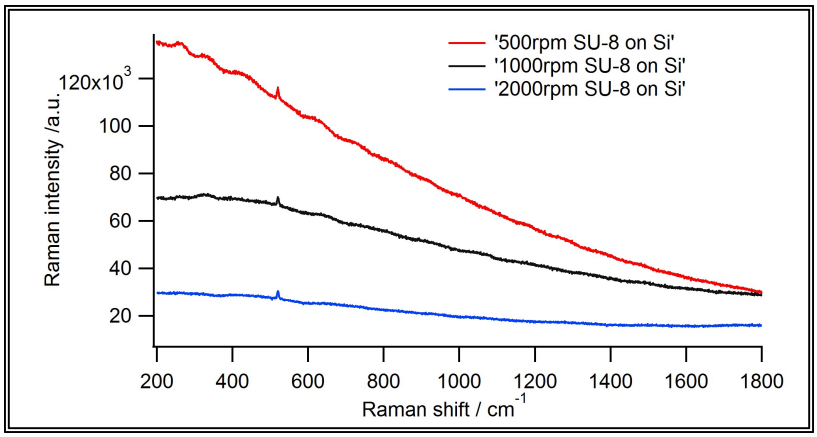

Figure 5.12: Raman spectra showing the effect of different thicknesses of the SU-8 films on the reduction of fluorescence emission from Si substrate

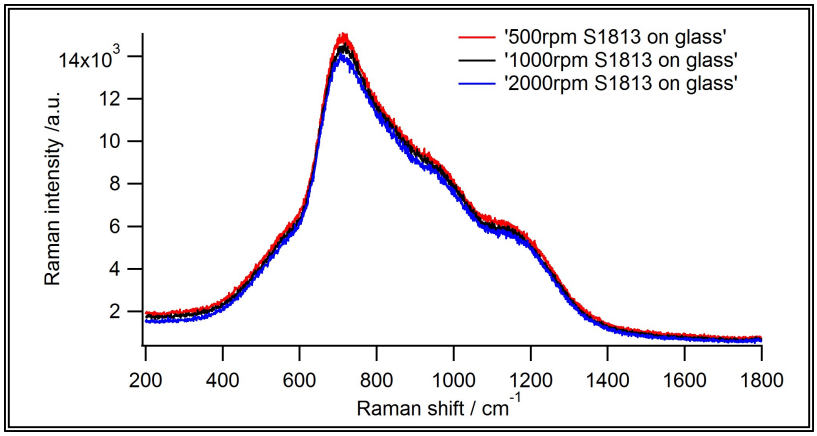

Figure 5.13: Raman spectra showing the effect of different thicknesses of the S1813 films on the reduction of fluorescence emission from glass substrate

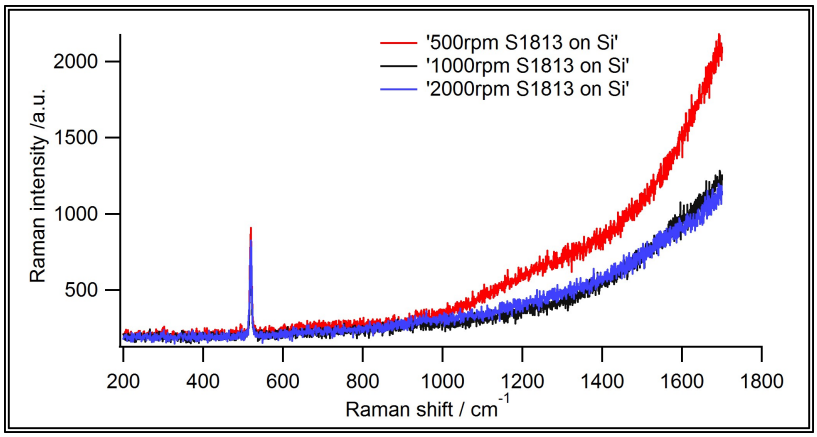

Figure 5.14: Raman spectra showing the effect of different thicknesses of the S1813 films on the reduction of fluorescence emission from Si substrate

5.5 Evaluation of substrate treatments

The result obtained from the plasma treatment shows that it can play an important role in improving the interaction between the substrate and the polymer interface. Oxygen plasma treatment makes the surface hydrophilic and removes contaminants from the surface [134, 135], which improves surface wettability and increases bonding strength between the MIP and the substrate. Plasma treatment is a chemical etching process where a new species is formed at the surface because of the chemical reaction that is taking place between the surface of a solid substrate and a gas atom, ion, or radical. The process is finally completed with the removal of the product molecule from the substrate [135]. The process can develop polar groups which can lead to the strong bonds within the surface layers providing a highly hydrophilic surface [134]. As can be seen in Figure 5.6, MIP islands form on the substrate before plasma treatment. When MIP solution is used after plasma treatment, it spreads all over the surface. This indicates that the strength of the intermolecular bonds between the substrate and the polymer interface is increased.

Reduction of fluorescence by covering the glass and Si surface with PDMS film reveals that thicker films block the glass and Si fluorescence better than the thinner films. As can be seen in Figure 5.8 and Figure 5.9, the spectra of the glass fluorescence observed at the range from 600 to 1400 cm^{-1}, and the spectra of the Si fluorescence observed at the range from 1500 to 2700 cm^{-1} increase with the increment of the spin speed as the films are becoming thinner. Also, it is noticeable in Figure 5.8 that the PDMS peak intensities are decreased as the glass fluorescence intensity is increased. In Figure 5.9, Si peak intensity (520 cm^{-1}) and fluorescence intensity increase as the spin speed increases. This result demonstrates that thicker films can obstruct the emission of light by the glass and Si substrate.

The effect of different spin times of the PDMS films on the emission of the glass

fluorescence is that less spin time to spread the film on the surface suppresses more fluorescence. For instance, in Figure 5.10, the film spun at 1000 rpm for 1 min (red spectrum) shows higher glass fluorescence than the film spun at 1000 rpm for 30 sec (black spectrum). This shows that the longer spin time can make a thinner film, which is also reported in the literature [122].

The SU-8 films on glass and Si substrates have considerably higher baselines in their Raman spectra. The Raman peaks of the SU-8 films ranged from 600 to 1500 cm^{-1} [137]. In Figure 5.11, the intensity of the Raman peaks of the SU-8 films is very low. It seems that SU-8 is itself auto fluorescent. The reported literature states that SU-8's auto fluorescence level is high compared to other photo patterned polymers [138]. Therefore, the Raman peaks of the SU-8 film are not visible due to the higher intensity of the fluorescence. Also, glass fluorescence is observed from Figure 5.11. In Figure 5.12, the Si peak is visible at 520 cm^{-1} but SU-8 peaks are not visible. Some broad peaks are seen at the 200 to 600 cm^{-1} range in the figure.

The obtained result for the effect of different thicknesses of the S1813 films on glass slides indicates that neither thicker nor thinner films reduce or cover the glass fluorescence. Here, the glass fluorescence is observed over the 600 to 1400 cm^{-1} range for both thicker and thinner films. In Figure 5.14, increasing spin speed decreases the fluorescence of Si substrates. Increasing spin speed makes the film thinner, therefore we are demonstrating that thinner films suppress the fluorescence from the underlying substrate better. This phenomenon can be explained from thin-film interference: the thinner S1813 films happen to be of appropriate thickness to block the wavelength range corresponding to the fluorescence emission from the Si substrate.

Based on the results from this section, the ultrathin film MIPs in subsequent sections will be prepared on thicker PDMS film on glass and Si slides.

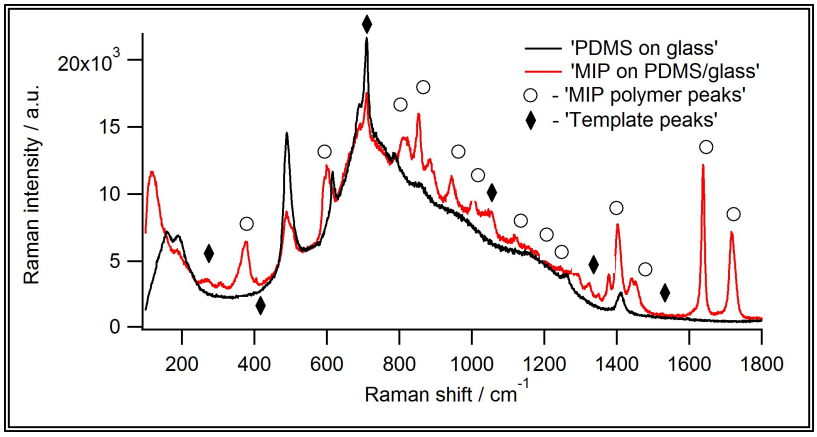

Figure 5.15: The comparison between the Raman spectrum of MAA-based modified ultrathin film MIP (modified procedure 1) on the PDMS/glass substrate and the Raman spectrum of PDMS on the glass

5.6 MAA-based modified ultrathin film MIP on PDMS/glass and PDMS/Si substrates

A Raman spectrum of the MAA-based modified ultrathin film MIP (modified procedure 1) on a PDMS/glass substrate is shown in Figure 5.15. The Raman bands of PDMS are observed at 488, 617, 687 709, 786, 860, 1263, and 1412 cm^{-1}. The characteristic MIP polymer peaks are present at approximately 376, 601, 811, 857, 888, 958, 1125, 1277, 1288, 1409, 1442, 1454, 1636, and 1722 cm^{-1}. The indicated peaks are for the template molecule at 251, 407, 712, 1040, 1350, and 1524 cm^{-1}. It can be seen from the figure that some of the polymer peaks and template peaks are overlapped with the PDMS peaks. For example, the 712 cm^{-1} template peak and 857 cm^{-1} polymer peak are overlapped with the 709 and 860 cm^{-1} PDMS peaks. Template peaks and MIP polymer peaks are indicated with small black diamonds and white circle.

The Raman spectrum of the formation of MAA-based modified ultrathin film MIP (modified procedure 1) on a PDMS/Si substrate is shown in Figure 5.16. The

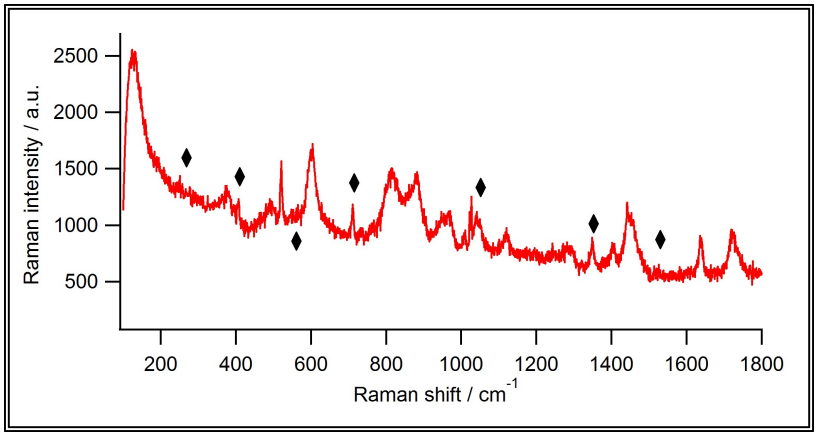

Figure 5.16: The Raman spectrum of MAA-based modified ultrathin film MIP (modified procedure 1) on the PDMS/Si substrate

characteristic main polymer peaks are present at approximately 376, 601, 811, 857, 888, 958, 1125, 1277, 1288, 1409, 1442, 1454, 1636, and 1722 cm^{-1}. The indicated peaks are for the template molecule and are observed at 251, 548, 407, 712, 1040, 1350, and 1524 cm^{-1}. The Si peak is observed at 520 cm^{-1}.

5.7 Discussion

The result obtained from the Raman spectrum of the MAA-based modified ultrathin film MIP (modified procedure 1) on the PDMS/glass substrate shows that the film was formed on the PDMS. The PDMS film was spun at 800 rpm for 60 sec onto the glass slide, and the film was spun at 100 rpm for 30 sec onto the PDMS. Though the glass fluorescence is observed at 600 to 1400 cm^{-1}, the template and the polymer peaks are visible in the film. The intensities of the template and polymer peaks in the range from 600 to 1400 cm^{-1} are lower because of the higher intensity of the glass fluorescence. The film was formed in a couple of places on the PDMS surface.

PDMS surface was plasma etched to improve hydrophilicity or wettability as plasma treatment provides silanol (Si-OH) groups and removes methyl groups ($Si-CH_3$)

of PDMS repeating units. As a result, the PDMS surface turns into a hydrophilic surface [134]. Some other literatures state that the hydrophobicity of the PDMS surface reduced by plasma treatment regains in less than an hour. It is suggested that thermal aging and chemical treatment make PDMS surface hydrophilic for long time [139,140]. These treatments can also be applied to make better hydrophilic PDMS surface for longer time. In our case, plasma treatment improved the wettability of the PDMS surface.

Another reason for not forming the film of the whole surface can be the weak interaction between the substrate and the polymer. The reported literature states that substrate interactions can significantly influence the thermal properties of the ultra thin polymer films. Thermal expansivities with thermal expansion coefficient depends on film thickness and changes with the film thickness [141]. Thermal expansion coefficient could also be different for the different multi layer film thickness.

On the other hand, the result obtained from the Raman spectrum of the MAA-based modified ultrathin film MIP (modified procedure 1) on the PDMS/Si substrate shows the formation of the film on the substrate. The film was spun at 100 rpm for 30 sec on the PDMS which was spun at 800 rpm for 60 sec on the Si. Since the film is uniformly spread over the surface, the PDMS peaks are not visible in the spectrum. The template and the polymer peaks are visible in the spectrum.

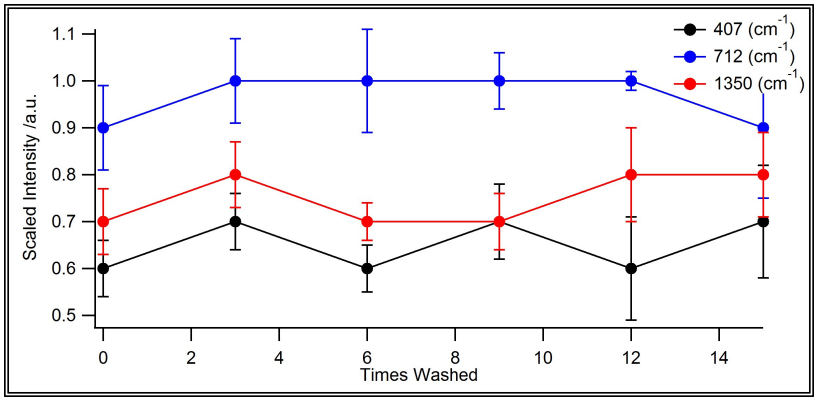

Figure 5.17: Graph of the average scaled peak intensity of the template vs times washed for the MIP prepared at 100 rpm.

5.8 Removal and reuptake of template of MAA-based modified ultrathin film MIP (modified procedure 1) on PDMS/Si substrate

The template was removed from different thickness of MAA-based modified ultrathin film MIPs (modified procedure 1). These films were made by using spin speed at 100, 200, and 300 rpm. Figure 5.17, Figure 5.18, and Figure 5.19 show the changes of the intensity of average (standard deviation) scaled peaks of the template after removing the template (phenanthrene) from the MAA-based modified ultrathin film MIPs.

The reuptake of template was also done with the same MAA-based modified ultrathin film MIPs (modified procedure 1). Figure 5.20, Figure 5.21, and Figure 5.22 show the changes of the intensity of average (standard deviation) scaled peaks of the template after reuptaking the template (phenanthrene) with the MAA-based modified ultrathin film MIPs.

Figure 5.23 shows the reproducibility of the MAA-based modified ultrathin film MIPs (modified procedure 1). The films were made by using the same spin speed (300 rpm), spin time (30 s), and cure time (120 s).

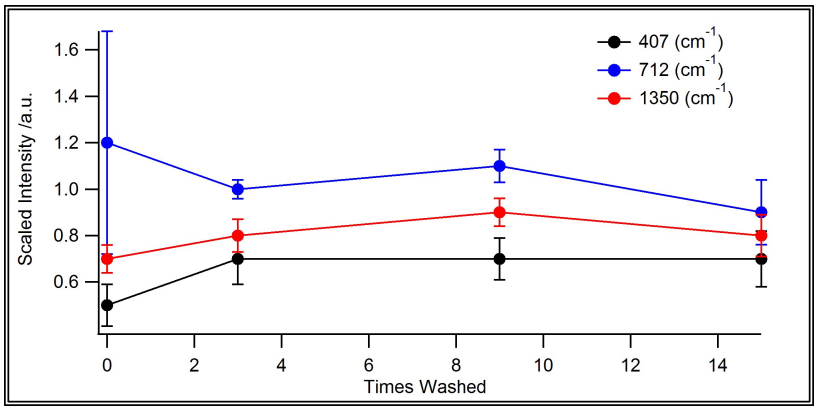

Figure 5.18: Graph of the average scaled peak intensity of the template vs times washed for the MIP prepared at 200 rpm.

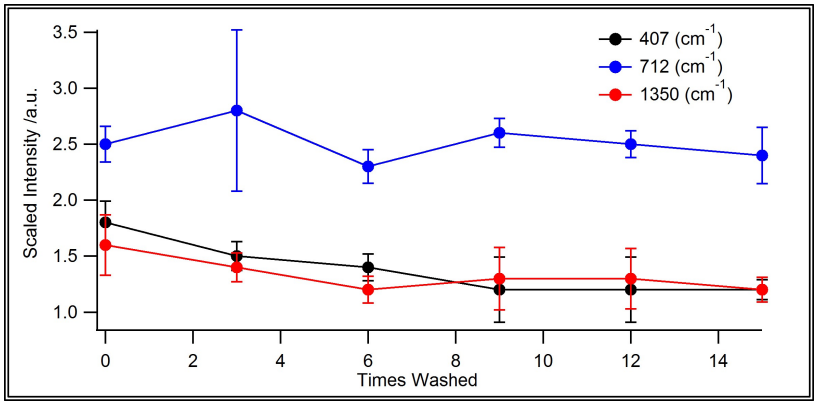

Figure 5.19: Graph of the average scaled peak intensity of the template vs times washed for the MIP prepared at 300 rpm.

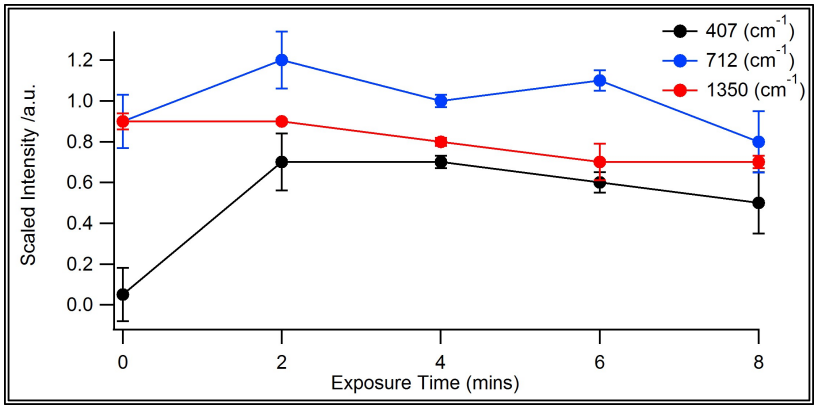

Figure 5.20: Graph of the average scaled peak intensity of the template vs exposure time for the MIP prepared at 100 rpm.

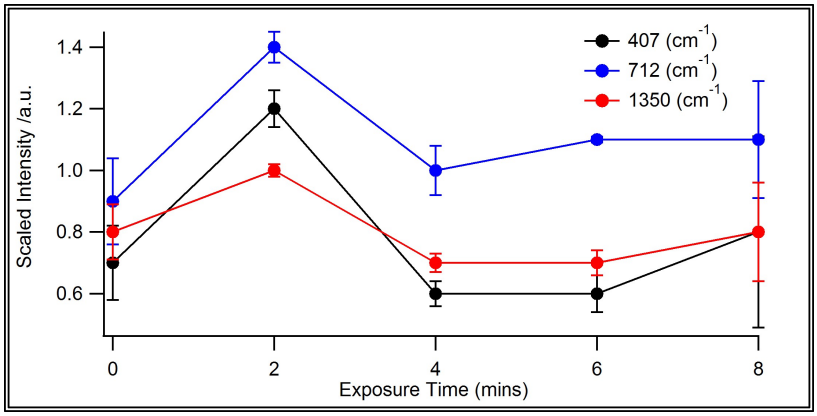

Figure 5.21: Graph of the average scaled peak intensity of the template vs exposure time for the MIP prepared at 200 rpm.

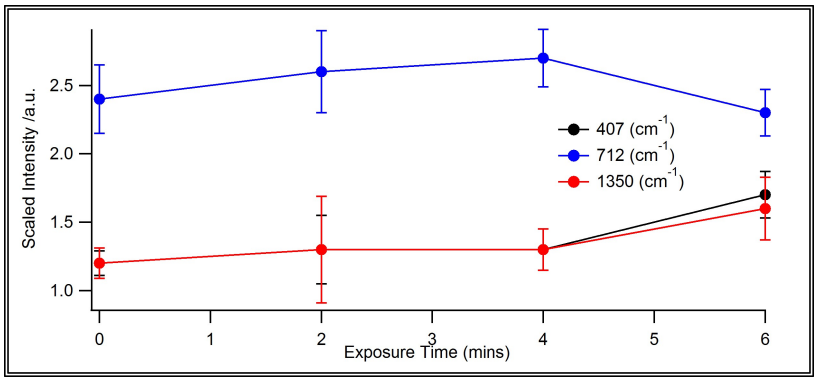

Figure 5.22: Graph of the average scaled peak intensity of the template vs exposure time for the MIP prepared at 300 rpm.

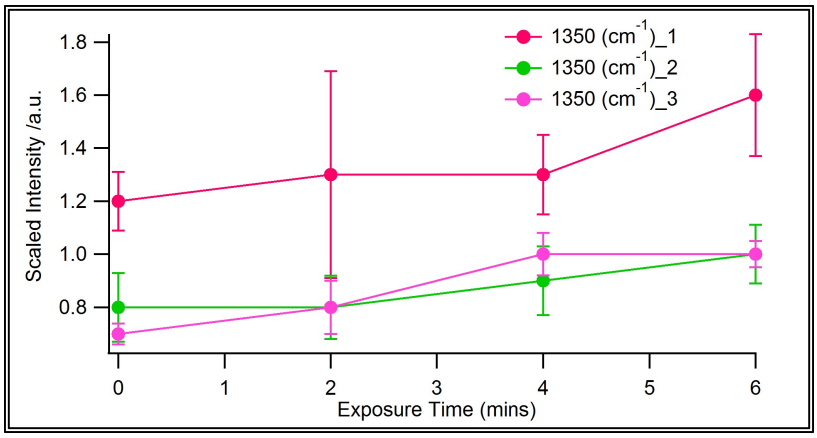

Figure 5.23: Graph of the average scaled peak intensity of the template vs exposure time for three ultrathin MIP films all prepared at 300 rpm for 30 s with a cure time of 120 s.

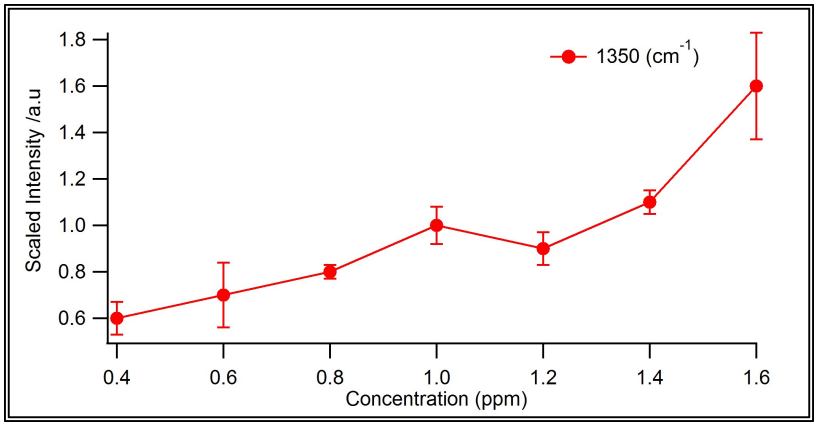

Figure 5.24: Graph of the reuptake capabilities of template of the MAA-based modified ultrathin film MIPs (modified procedure 1) from different template concentrations.

Figure 5.24 shows the reuptake capabilities of template of the MAA-based modified ultrathin film MIP (modified procedure 1) from different template concentrations.

5.8.1 Discussion

It can be seen from Figures 5.17 and 5.18 that there is a disorder between peak intensities of the template after removing the template from MAA-based modified ultrathin film MIPs. The peaks at 407, 712, and 1350 cm^{-1} do not gradually decreases after removing the template. Also, this result is consistent with the reuptake of template from aqueous template/analyte solution. It can be seen from Figure 5.20 and Figure 5.21 that the peaks at 407, 712, and 1350 cm^{-1} do not gradually increases after reuptaking the template.

In contrast, it can be seen from Figures 5.19 and 5.22 that there is a positive order of peak intensities of the template after its removal and reuptake. The peaks at 407, 1350 cm^{-1} gradually decrease after removing the template. Also,the peaks at 407 and 1350 cm^{-1} gradually increase after reuptaking the template. The reason of this phenomenon is that increasing spin speed makes the film thinner which can provide

more homogeneity of the film. The first two films was made by using 100 and 200 rpm spin speed. On the other hand, the last film was made by using 300 rpm spin speed. Increasing spin speed can improve the homogeneity of the film. Therefore, removal and reuptake of template follow a positive pattern for the last film. The other peak at 712 cm^{-1} does not follow the removal and reuptake pattern because it overlaps with the PDMS peak present at 709 cm^{-1}.

It can be seen from Figure 5.23 that thinner films can be reproducible. The peak at 1350 cm^{-1} of the three films gradually increases after reuptaking the template from aqueous template/analyte solution. Although the scaled peak intensity is slightly different for the first films, the other two films reuptake the same intensity of the peaks. Figure 5.24 shows MAA-based modified ultrathin film MIPs reuptake different peak intensity of the template from different concentrations of aqueous template/analyte solutions. The peak at 1350 cm^{-1} gradually increases with increasing the concentration of aqueous template/analyte solution. For instance, the scaled peak intensity at 1350 cm^{-1} is 0.6 (0.19) at 0.4 ppm concentration and 1.7 (0.17) at 1.6 ppm concentration.

5.9 Conclusion

Based on the discussion from this chapter, the baseline of the Raman spectra of ultrathin film MIPs formed on glass substrate is slightly higher since glass has high fluorescence. Various non-fluorescent substrates reduce fluorescence emission from the substrates such as glass and Si wafers. Among all non-fluorescent substrates, PDMS-coated Si substrates perform better for deposition of ultrathin film MIP than PDMS-coated glass substrates. Also, S1813 coated Si substrate has lower baseline spectra than that of SU-8 coated Si substrate. In case of S1813 coated Si substrate,

substrate fluorescence decreased by increasing spin speed. Increasing spin speed produced thinner S1813 film on the Si substrate. Plasma treatment improves the surface wettability of different substrates. It reveals that higher spin speed can improve the homogeneity of the film, and thinner films can be reproducible. The diagnostic unique peak for phenanthrene's removal and reuptake is 1350 cm^{-1}, and the suitable reuptake time for template (phenanthrene) is 0 to 6 mins.

Chapter 6

Conclusions and Future Work

6.1 Summary

Film fabrication was improved by increasing the surface wettability. Plasma treatment was applied to increase the surface wettability. Non-fluorescent substrates were designed and created in order to reduce fluorescence emission from the substrates. PDMS-coated Si substrates performed well to deposit ultrathin film MIP than PDMS-coated glass substrates. Also, S1813 coated Si substrate has lower baseline spectra than that of SU-8 coated Si substrate. In case of S1813 coated Si substrate, substrate fluorescence decreased by increasing spin speed. Increasing spin speed produced thinner S1813 film on the Si substrate. This result indicated that thin film can interfere with the obstruction of the fluorescence.

Ultrathin film MIP preparation was optimized following a new procedure. The effect of different spin speeds on ultrathin film MIP structure was explored. Different spin speeds produced different film morphologies. For example, pore density was different for different films. Also, different spin speeds produced different film thicknesses. The ultrathin films' thicknesses ranged from 300 nm to 4 nm. Higher spin

speed produced the thinner films of the ultrathin film. For instance, 45 nm and 4 nm film thickness were generated by using 1000 rpm and 2000 rpm spin speed, respectively. Our results found that thinner films were more reproducible than the thicker films of the ultrathin films.

Sensing parameters were determined for ultrathin film MIPs. Suitable reuptake times were studied to reuptake analyte from aqueous template/analyte solution. The suitable reuptake time for template (phenanthrene) was 0 to 6 mins. A diagnostic analyte peak was identified in order to recognize the unique peak for analyte's removal and reuptake. The peak at 1350 cm^{-1} was unique for phenanthrene's removal and reuptake.

6.2 Future work

For making ultrathin film MIPs on PDMS/Si substrates, we had limitations in the spin speeds that we considered because of low signal of target analyte without incorporating a SERS substrate. When we use higher spin speed to make ultrathin film MIPs on the PDMS on Si substrate, PDMS does not enhance the analyte signal. As a result, it is difficult to diagnose analyte peaks of MIP on the PDMS on Si substrate. Also, it is difficult to measure film thickness on the PDMS/Si substrate.

Since thinner films of S1813 on Si substrate suppress the fluorescence from the underlying substrate better, these films can be used to test the depositing MIP as an ultrathin film. Also, future work should be carried out with the incorporation of ultrathin film MIP with metal coated substrates (SERS substrates). Different metal coated substrates of ultrathin film MIP and different thicknesses of ultrathin film MIP should be studied. Moreover, selectivity of analyte (e.g. multianalyte detection) should be studied. To test the efficiency and performance of the MIP-SERS substrates,

a field trial on the substrates with real environmental samples could be a worthy option.

Appendix A

Supporting information for bulk MIPs

Figure A.1 shows the recorded Raman spectrum of the MAA-based MIP and MAA-based modified bulk MIP (modified procedure 1). The polymer peaks are found at approximately 376, 601, 811, 857, 888, 958,1042, 1125, 1277, 1288, 1409,1442, 1454, 1636, and 1722 cm^{-1}. Additional peaks at 251, 410, 548, 712, 1040, 1350, 1524, 1570, and 1616 cm^{-1} are attributed to phenanthrene. The peaks are indicated in the spectrum. In this figure, MAA-based bulk MIP has low intensity phenanthrene peaks, whereas MAA-based modified bulk has high intensity phenanthrene peaks.

A.1 supporting information for SU-8 and S1813 polymer

Figure A.2 and Figure A.3 show the spin curve of the polymer. It can be seen from the figure that film thickness decreases with increasing spin speed. Data of the two films' thicknesses is from the manufacturer (MicroChem).

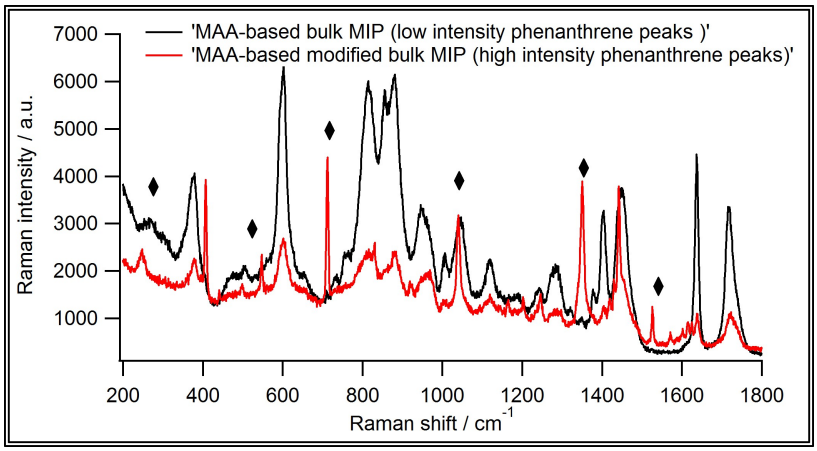

Figure A.1: Raman spectrum of MAA-based bulk MIP and MAA-based modified bulk MIP (modified procedure 1)

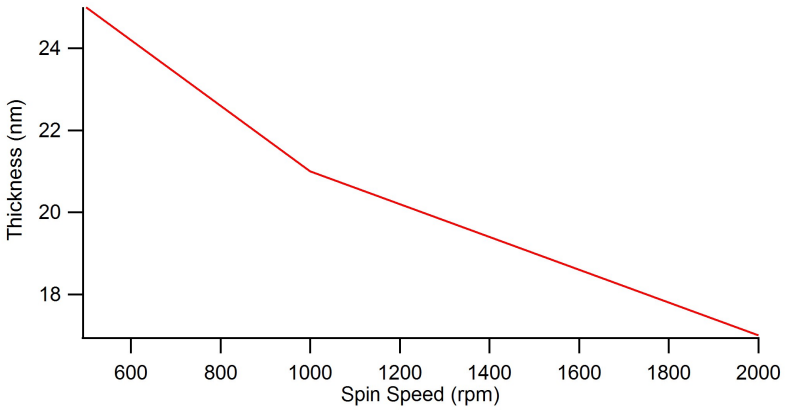

Figure A.2: Spin curve of SU-8 polymer film

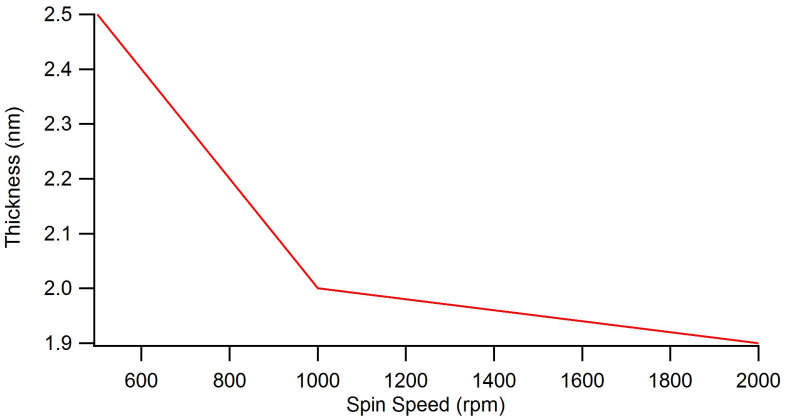

Figure A.3: Spin curve of S1813 polymer film

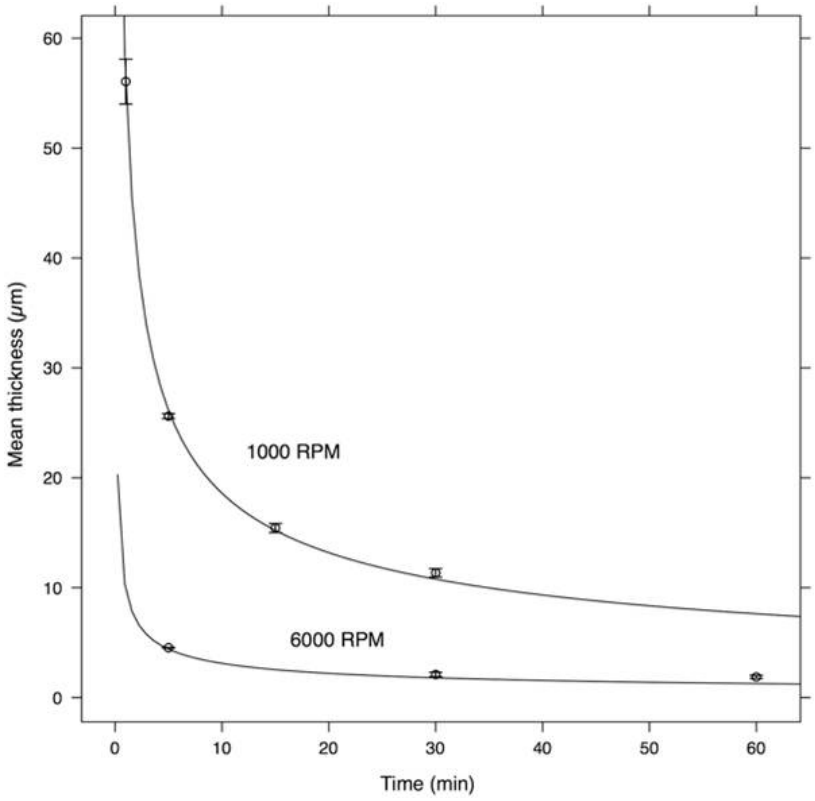

Figure A.4: Thickness of PDMS films under two different speeds. "Used under Public Domain". Koschwanez JH, Carlson RH, Meldrum DR (2009) Thin PDMS Films Using Long Spin Times or Tert-Butyl Alcohol as a Solvent.

A.2 Supporting information for PDMS polymer

Figure A.4 shows the spin curve of PDMS polymer film. It can be seen from the figure that film thickness decreases with increasing spin speed.

Appendix B

PDMS-based MIP

B.1 PDMS-based MIP thin film

Different protocols were used to make PDMS-based MIP thin films. The films were characterized by Raman spectroscopy. The results of the characterization are summarized below. Furthermore, the results of the template removal and reuptake of PDMS-based MIP thin films by using different solvents are described below.

B.1.1 Raman Spectroscopy

The Raman spectrum of PDMS-based MIP thin film (protocol 1) is shown in Figure B.1. The spectrum is heavily influenced by the glass fluorescence. Some shoulders are present in the spectrum. The shoulders are observed at 496, 667, and 865 cm^{-1}. Those peaks are for PDMS.

The Raman spectrum of PDMS-based MIP thin film (protocol 2) is shown in Figure B.2. The spectrum is heavily influenced by the glass fluorescence. Some shoulders are present at 496, 618, 711, and 1408 cm^{-1} in the spectrum . Those peaks are for PDMS.

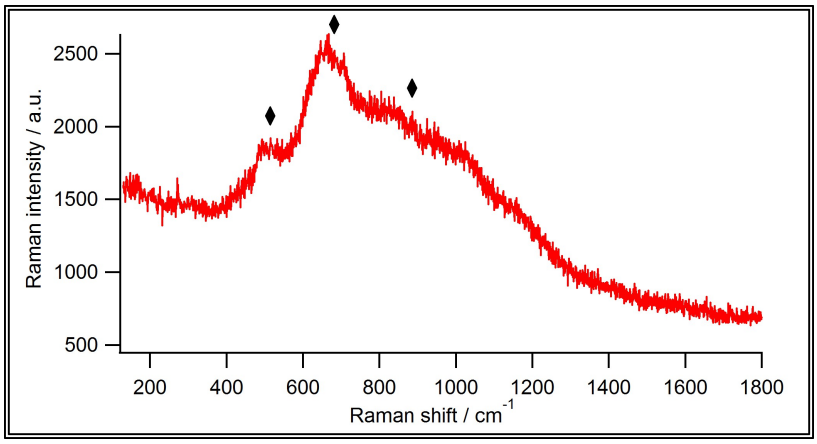

Figure B.1: The Raman spectrum of PDMS-based MIP thin films (protocol 1) on Al wrapped glass substrate

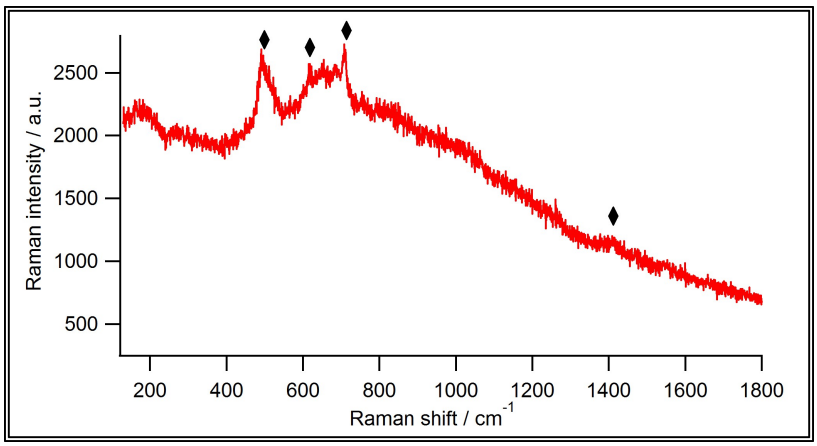

Figure B.2: The Raman spectrum of PDMS-based MIP thin films (protocol 2) on Al wrapped glass substrate

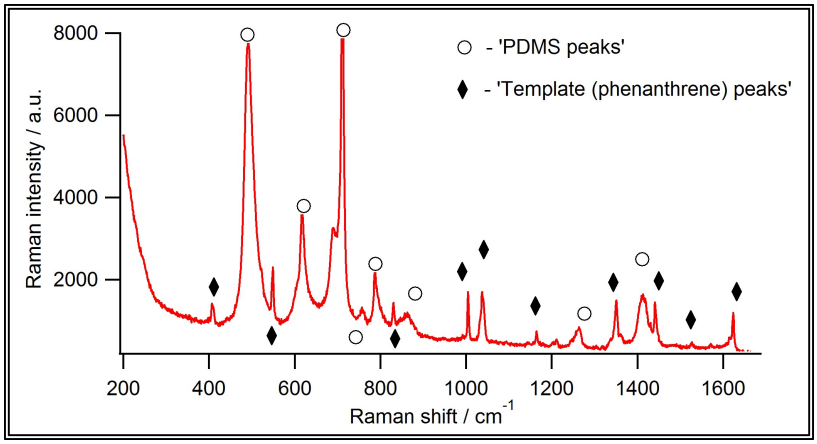

Figure B.3: The Raman spectrum of PDMS-based MIP thin films (protocol 3) on Al wrapped glass substrate

Figure B.3 shows the Raman spectrum of the formation of PDMS-based MIP thin films. The Raman bands of PDMS are observed at 488, 617, 687 709, 786, 860, 1263, and 1412 cm^{-1}. The template (phenanthrene) peaks are observed at 407, 548, 832, 1006, 1040, 1164, 1350, 1443, 1524, and 1624 cm^{-1}. PDMS and template peaks are indicated with white circle and black diamonds in the spectrum.

The Raman spectra of two different PDMS-based MIP thin films made using different spin speeds are shown in Figure B.4. It can be seen from the figure that different spin speeds produce different intensities of the template peaks. The peaks are indicated with small black diamonds in the spectra.

B.1.2 Removal and reuptake

The results of the Raman spectra of template removal of PDMS-based MIP thin film (protocol 3) with 95 % ethanol are shown in Figure B.5. In the figure, the red spectrum shows the Raman spectrum of the thin film before washing, and the black spectrum shows the Raman spectrum of the thin film after 5 times washing. The intensities of the two spectra are very different. The template peaks are indicated

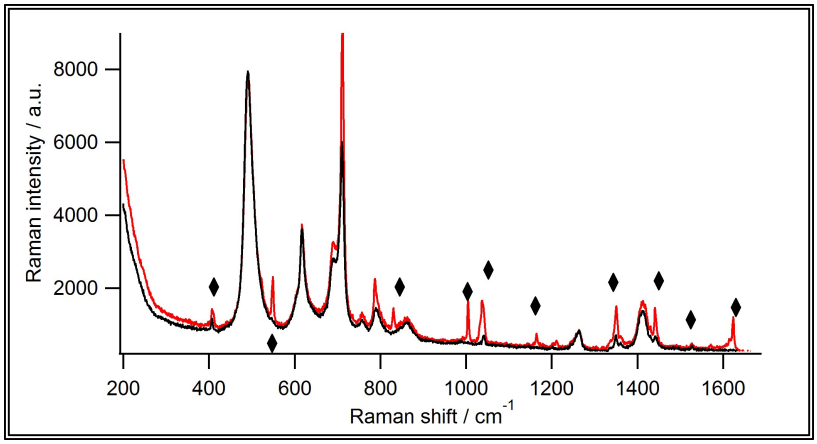

Figure B.4: The effect of spin speed on the intensities of the template peaks. The film with red spectrum spun at 800 rpm, and the film with black spectrum spun at 500 rpm.

with small black diamonds.

The results of the Raman spectra of template removal of PDMS-based MIP thin film (protocol 3) are shown in Figure B.6. In the figure, the red spectrum shows the Raman spectrum of the thin film before washing with acetonitrile; the green spectrum shows the Raman spectrum of the thin film after washing 2 times; the black spectrum shows the Raman spectrum of the thin film after washing 7 times; the blue spectrum shows the Raman spectrum of the thin film after washing 12 times; and the yellow spectrum shows the Raman spectrum of the thin film after washing 17 times. The intensities of the template peaks of the five spectra are not similar. The template peaks are indicated with small black diamonds.

The results of the Raman spectra of template reuptake of PDMS-based MIP thin film (protocol 3) are shown in Figure B.7. In the figure, the red spectrum shows the Raman spectrum of the thin film after 17 times washing with acetonitrile; the green spectrum shows the Raman spectrum of the thin film after 8 mins immersion into aqueous template solution; the black spectrum shows the Raman spectrum of the thin film after 33 mins immersion; the blue spectrum shows the Raman spectrum of

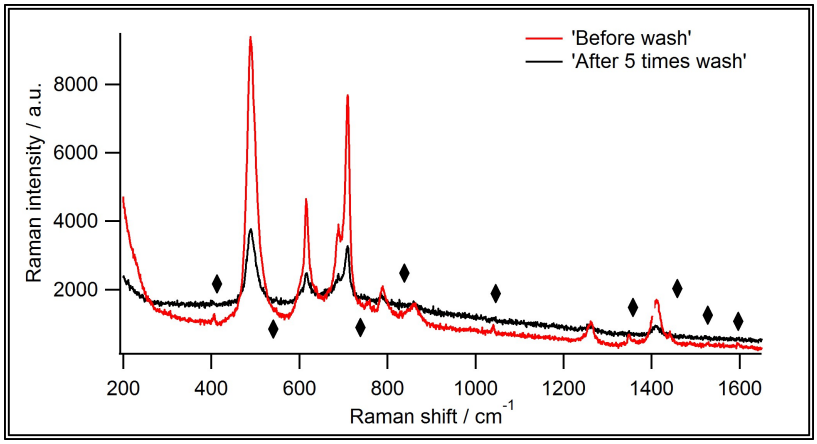

Figure B.5: The comparison between the Raman spectrum of the PDMS-based MIP thin film (protocol 3) before and after template removal.

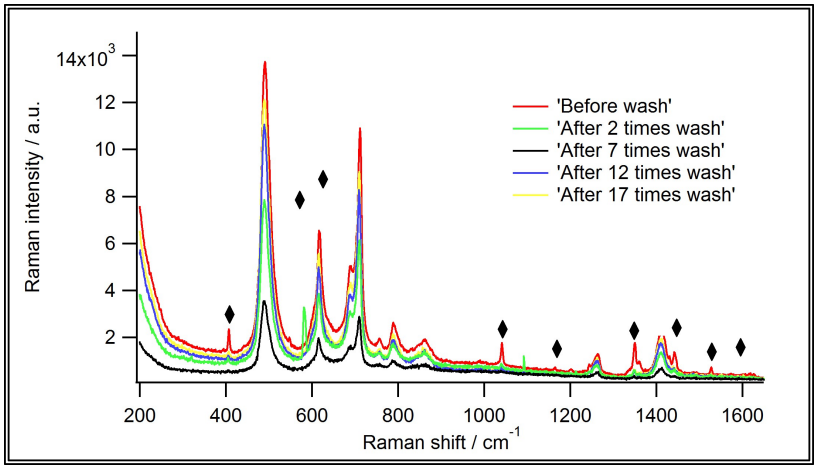

Figure B.6: The comparison between the Raman spectrum of the PDMS-based MIP thin film (protocol 3) before and after template removal.

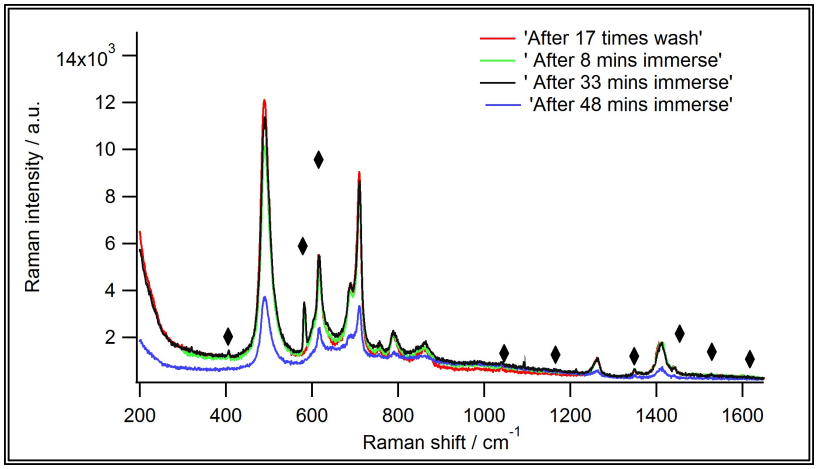

Figure B.7: The comparison between the Raman spectrum of the PDMS-based MIP thin film (protocol 3) before template removal and after template reuptake

the thin film after 48 mins immersion. There is no order of the template intensities. The template peaks are indicated with small black diamonds.

B.2 Discussion

Figure B.1, Figure B.2, and Figure B.3 show three specta which indicate the formation of PDMS-based MIP thin films. Though the first two spectra show some peaks of PDMS but the third one shows all the peaks of PDMS and phenanthrene. The reason of this phenomenon is the ratio of the precursors used to make the last film was different than the ratio involved in preparation of the first two films. Also, sonication was used to mix the reagents together for the third protocol while making the film. The results reveal that the PDMS-based MIP thin film was formed using protocol 3.

The result of the effect of spin speed on the intensities of the template peaks show that higher spin speed can play a role on the intensities of the template peaks. Higher spin speed produces more intense template peaks. The film with the red spectrum has higher intense template peaks than that of the film with the black spectrum. The

reason of the phenomenon can be higher spin speed which makes the film thinner, and the cavity matrix of the template (phenanthrene) that can take place at the top of the surface in the thin film rather than the thicker film.

The result of the template removal of PDMS-based MIP thin film with 95 % ethanol shows that the intensities of the PDMS peaks and template peaks decrease when washed for 5 times. It indicates that the solvent removes both polymer and template. The results of the template removal of PDMS-based MIP thin film with acetonitrile shows no order of the template removal. Some spectra show similar intensities of the template peaks, but some spectra indicate that the intensities of the template peaks and PDMS peaks decrease in the spectra.

The result obtained from the template reuptake after the immersion of the film into aqueous phenanthrene solution shows that reuptaking the template is not working. The compatibility of PDMS with organic solvents has been reported in the literature [142]. It indicates that PDMS solvent compatibility is significant when the potential PDMS-based microfluidic devices are considered. Solubility of the solvent in PDMS has a effect on the swelling of the PDMS. This swelling could be a problem in making the PDMS-based MIP, because PDMS-based MIP could be swollen when rinsed for template removal. As a result, it could lose its original template cavity shape. This could also impact the rebinding process of template.

The reported paper states that low solubility solvent such as acetonitrile and ethanol have a low solubility in PDMS. Therefore, these solvents can be used in PDMS microfluidic systems when carrying synthetic reactions in these solvents [142]. In contrast, in our PDMS-based MIP thin film case, the solvent such as concentrated ethanol used to remove the template, intensities of the polymer peaks change. It means the amount of the polymer materials could be changed. In case of ethanol, it may be useful to use a low concentration of ethanol for removing the template

as well as to check how the removal process works. On the other hand, in case of acetonitrile there may be some solvent effect as the template in the film was dissolved with toluene, but the template was removed by acetonitrile. Since toluene is a high solubility solvent in PDMS, it may be useful to use the same solvent while making the polymer film as well as removing the template from the polymer film. Also, other low solubility solvent may be useful for the template removal.

Appendix C

Metal supported ultrathin film MIP

Since we have a limitations in the spin speeds of making ultrathin film MIPs on PDMS/Si substrates because of low signal of target analyte without incorporating a SERS substrate, we used metal coated substrates as a SERS substrates to make ultrathin film MIP. We mentioned earlier in the Introduction chapter that, in the MIP-SERS concept, the MIP concentrates the target analyte adjacent to a SERS-active surface which can enhance the Raman signal of the analyte molecule by a factor of 10^{10}. As a result, we can easily diagnose the analyte signal of ultrathin film MIP. Moreover, high selectivity, sensitivity, and portability in sensing applications can be maintained as well as the cost and size of the sensor can be reduced introducing a proper MIP-SERS sensing format.

Table C.1: Thickness of the Ag/Cr films

Annealed temperature (°C)	AFM thickness (nm)	profilometer thickness (nm)
250	86	120
300	50	48.5
350	97	113
400	101	115

C.1 Metal coated films

The thickness of a few Ag/Cr films was measured by AFM and profilometer. The results of the films' thicknesses are described below. The films were prepared by Md. Majibur Rahman [124].

C.1.1 AFM and profilometer

Table C.1 shows the Ag/Cr films' thicknesses measured by AFM and profilometer. It can be seen from these table that different annealed temperature produces different thickness of the films. Unannealed Ag/Cr film thickness measured by AFM and profilometer are respectively 59 nm and 45.9 nm.

C.1.2 Metal coated MAA-based ultrathin film MIP on Al/-glass, Al/Si, and Al/plastic substrate

The comparison between the Raman spectrum of MAA-based ultrathin film MIP on Al/glass substrate, and the Raman spectrum of Al/glass substrate is shown in Figure C.1. In this figure, the two Raman spectra are very similar. Also, fluorescence is observed in the range of 600 to 1200 cm^{-1} for both spectra.

The comparison between the Raman spectrum of MAA-based ultrathin film MIPs on Al/Si substrate and the Raman spectrum of Al/Si substrate is shown in Figure C.2. In this figure, two raman spectra are almost similar. Fluorescence is observed at

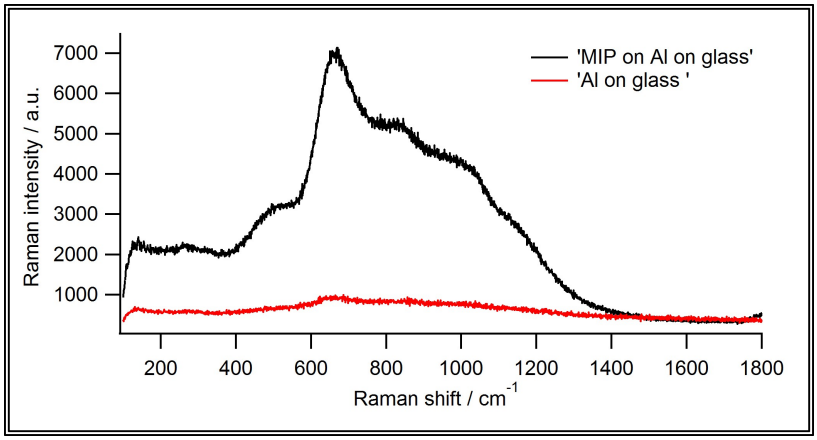

Figure C.1: Comparison between the Raman spectrum of MAA-based ultrathin film MIP on Al/glass substrate and the Raman spectrum of Al/glass substrate.

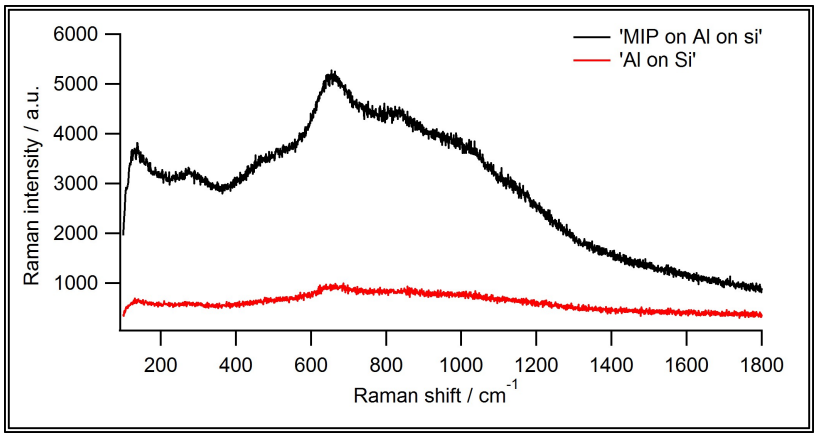

Figure C.2: Comparison between the Raman spectrum of MAA-based ultrathin film MIP on Al/Si substrate and the Raman spectrum of Al/Si substrate.

the range 600 to 1200 cm^{-1} for both spectra.

The comparison between the Raman spectrum of MAA-based ultrathin film MIPs on Al/plastic substrate, the Raman spectrum of Al/plastic substrate, and the Raman spectrum of plastic is shown in Figure C.3. In this figure, plastic peaks are observed at 282, 303, 382, 441, 460, 575, 631, 703, 795, 860, 1001, 1095, 1119, 1188, 1293, 1418, 1463, 1585, 1617, and 1726 cm^{-1}. The other two spectra are totally different from this spectra where the plastic peaks are not observed. Fluorescence is observed at the range 600 to 1200 cm^{-1} for the two spectra.

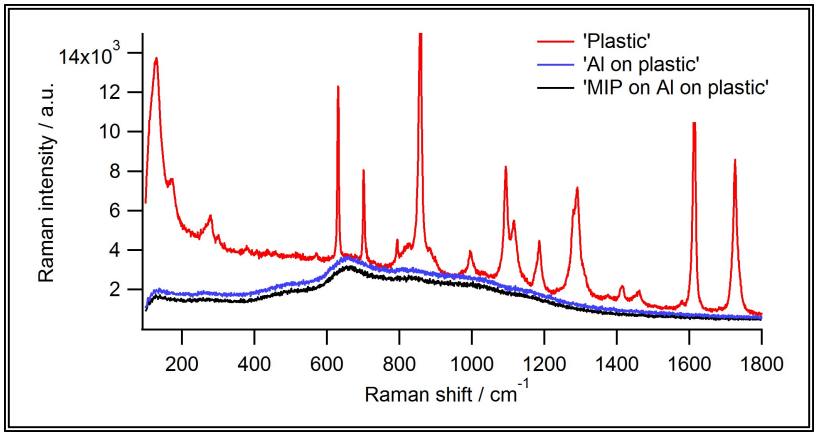

Figure C.3: Comparison between the Raman spectrum of MAA-based ultrathin film MIPs on Al/plastic, the Raman spectrum of Al/plastic, and the Raman spectrum of plastic substrates.

C.1.3 Metal coated MAA-based ultrathin film MIP on Ag/-plastic and Ag/Cu on plastic substrates

In Figure C.4, the black spectrum shows the MAA-based ultrathin film MIP on Ag /plastic substrate. The indicated peaks are observed at 222, 370, 416, 458, 518, 633, 660, 695, 741, 770, 837, 802, 858, 934, 1033, 1131, 1155, 1180, 1249, 1402, 1328, 1610, and 1724 cm^{-1}. The peaks are indicated with small black diamonds. The red spectrum show the all plastic peaks which are overlapped with the ultrathin film. Also, the blue spectrum shows the MAA-based bulk MIP peaks. Most of the peaks of the bulk MIP are overlapped with the plastic peaks.

Figure C.5 shows the comparison between the Raman spectrum of MAA-based ultrathin film MIP on the Ag/Cu on plastic substrate, and the Raman spectrum of Ag/Cu on plastic substrate. It can be seen from the figure that some peaks are present in the both spectra. Also, significant fluorescence is observed at the range 600 to 1200 cm^{-1} for the spectra of the thin film.

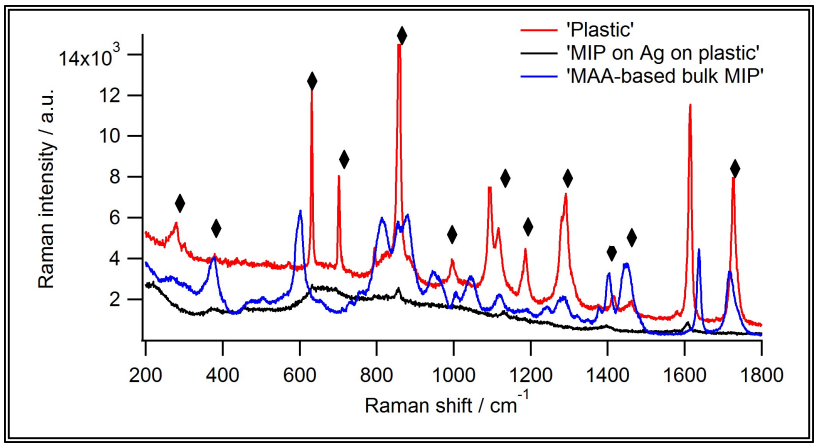

Figure C.4: Comparison between the Raman spectrum of plastic, MAA-based ultrathin film MIP on Ag/plastic substrate, and MAA-based bulk MIP.

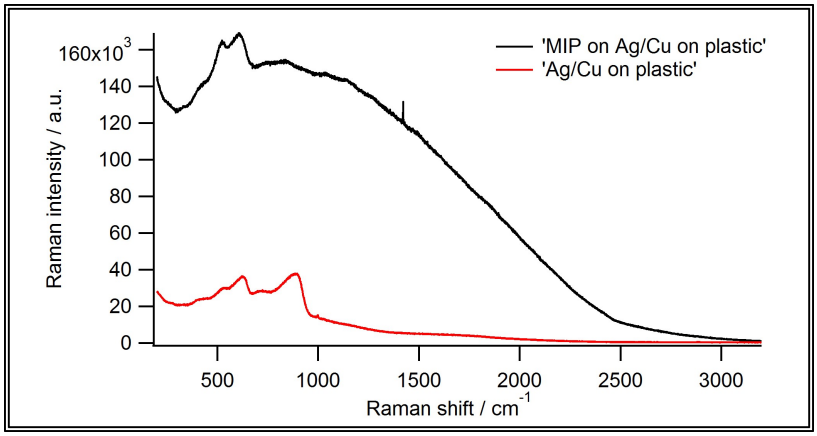

Figure C.5: Comparison between the Raman spectrum of MAA-based ultrathin film MIP on the Ag/Cu on plastic and the Raman spectrum of Ag/Cu on plastic substrates.

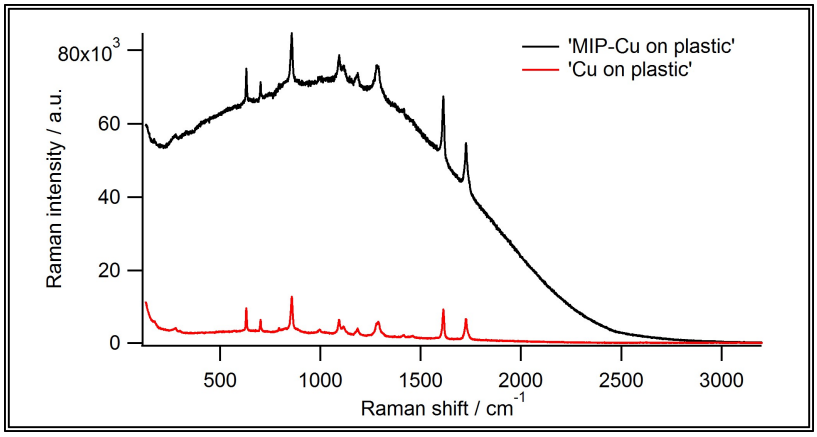

Figure C.6: Comparison between the Raman spectrum of MAA-based ultrathin film MIP on Cu/plastic and the Raman spectrum of Cu/plastic substrates.

C.1.4 Metal coated MAA-based ultrathin film MIP on Cu/-plastic substrate

The comparison between the Raman spectrum of MAA-based ultrathin film MIP on Cu/plastic, and the Raman spectrum of Cu/plastic substrates is shown in Figure C.6. In this figure,plastic peaks and MIP thin film are observed at exactly same position. The positions are 282, 303, 382, 441, 460, 575, 631, 703, 795, 860, 1001, 1095, 1119, 1188, 1293, 1418, 1463, 1585, 1617, and 1726 cm^{-1}.

C.1.5 Metal coated MAA-based ultrathin film MIP on Au/SU-8 on plastic substrate

Figure C.7 shows the comparison between the Raman spectrum of MAA-based ultrathin film MIP on the Au/SU8 on plastic, and the Raman spectrum of Au/SU8 On plastic substrates. As can be seen in Figure C.7, plastic peaks and ultrathin film MIP peaks are present at 282, 303, 382, 441, 460, 575, 631, 703, 795, 860, 1001, 1095, 1119, 1188, 1293, 1418, 1463, 1585, 1617, and 1726 cm^{-1}.

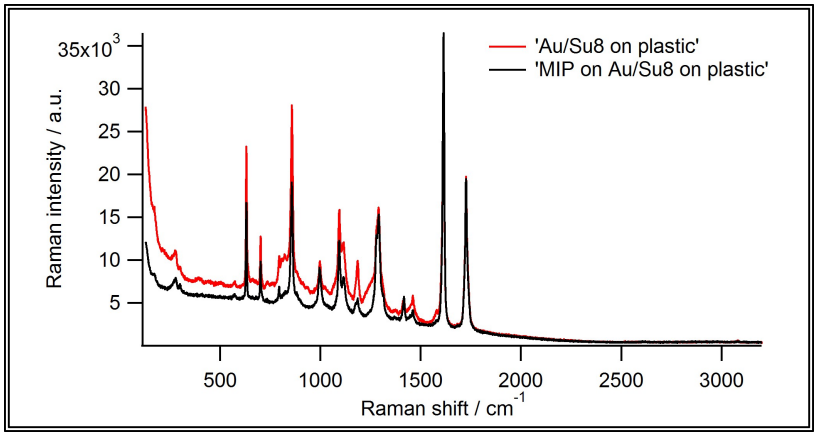

Figure C.7: Comparison between the Raman spectrum of MAA-based ultrathin film MIP on the Au/SU8 on plastic and the Raman spectrum of Au/SU8 on plastic substrates.

C.1.6 Metal coated MAA-based ultrathin film MIP on Au/Ag on glass substrate

The comparison between the Raman spectrum of MAA-based ultrathin film MIP on the Au/Ag on glass, and the Raman spectrum of Au/Ag on glass substrates is shown in Figure C.8. Some peaks are observed at the same position in the two spectra. Those peaks are observed at 141, 227, 670, 838, and 985 cm^{-1}. Some peaks are present only in the ultrathin film spectrum. Those peaks are observed at 546, 2864, and 2897 cm^{-1}. Also, the two spectra are heavily influenced by the glass fluorescence.

C.1.7 Metal coated MAA-based ultrathin film MIP on Ag/Cr on glass substrate

The Raman spectrum of MAA-based ultrathin film MIP on the Ag/Cr (250°C) on glass substrate is shown in Figure C.9. In the figure, some shoulders are present at 220, 554, 936, 1160, 1576, 1614, and 2593 cm^{-1}. Those shoulders are indicated with small black diamonds.

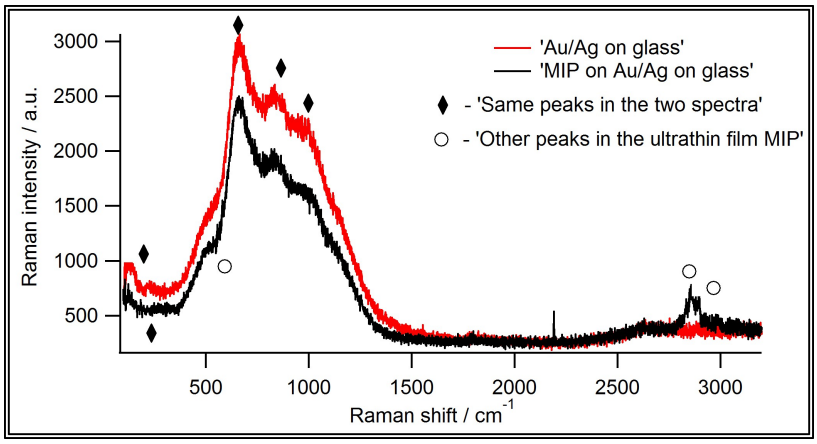

Figure C.8: The comparison between the Raman spectrum of MAA-based ultrathin film MIP on the Au/Ag on glass and the Raman spectrum of Au/Ag on glass substrates.

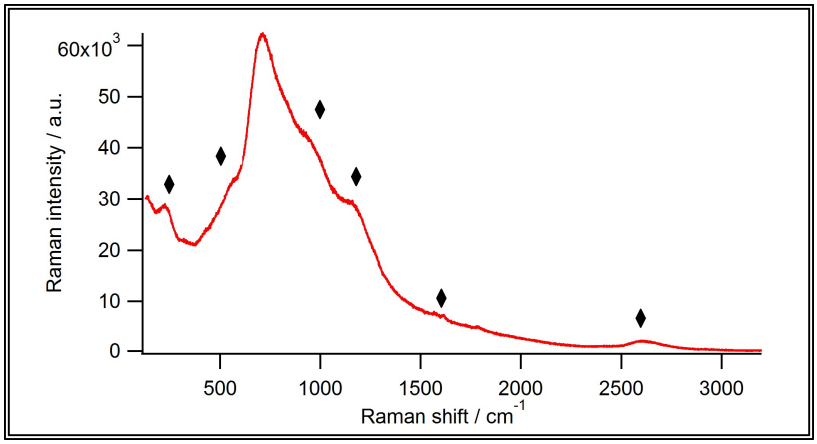

Figure C.9: The Raman spectrum of MAA-based ultrathin film MIP on the Ag/Cr (250°C) on glass substrate.

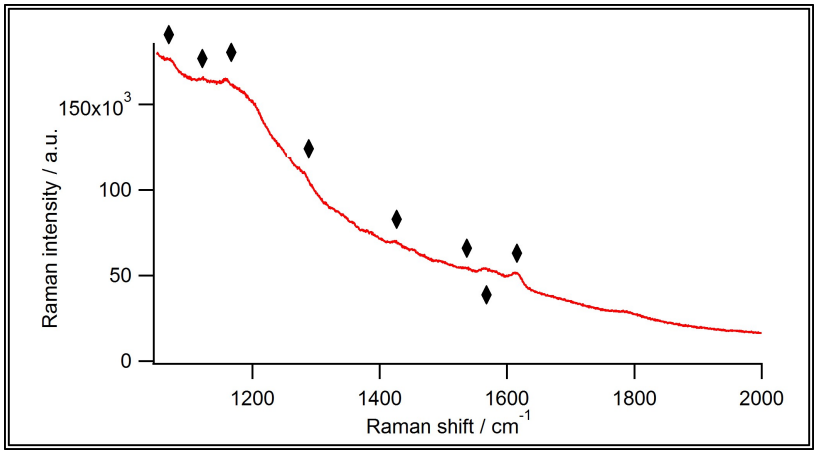

Figure C.10: Different range of the Raman spectrum of MAA-based ultrathin film MIP on the Ag/Cr (250°C) on glass substrate.

Figure C.10 shows the different range of the Raman spectrum of the previous film. It can be seen from the figure that some different peaks are observed in this range. The peaks are present at 1066, 1124, 1160, 1278, 1426, 1536, 1565, and 1626 cm^{-1}.

The Raman spectrum of MAA-based ultrathin film MIP on the Ag/Cr (300°C) on glass substrate is shown in Figure C.11. In the figure, some peaks are present at 194, 345, 616, 741, and 1163 cm^{-1}. Those peaks are indicated with small black diamonds.

The Raman spectrum of MAA-based ultrathin film MIP on the Ag/Cr (350°C) on glass substrate is shown in Figure C.12. In the figure, some shoulders are observed at 1145, 1783, and 2608 cm^{-1}. The spectrum is heavily influenced by the glass fluorescence.

Figure C.13 shows the Raman spectrum MAA-based ultrathin film MIP on the Ag/Cr (400°C) on glass substrate. It can be seen from the figure that some shoulders are observed at 1145, 1783, and 2608 cm^{-1}. The spectrum is also heavily influenced by the glass fluorescence.

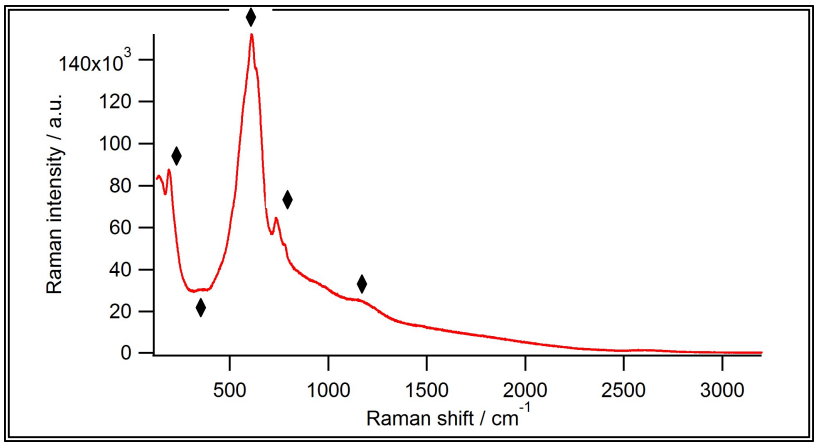

Figure C.11: The Raman spectrum of MAA-based ultrathin film MIP on the Ag/Cr (300°C) on glass substrate.

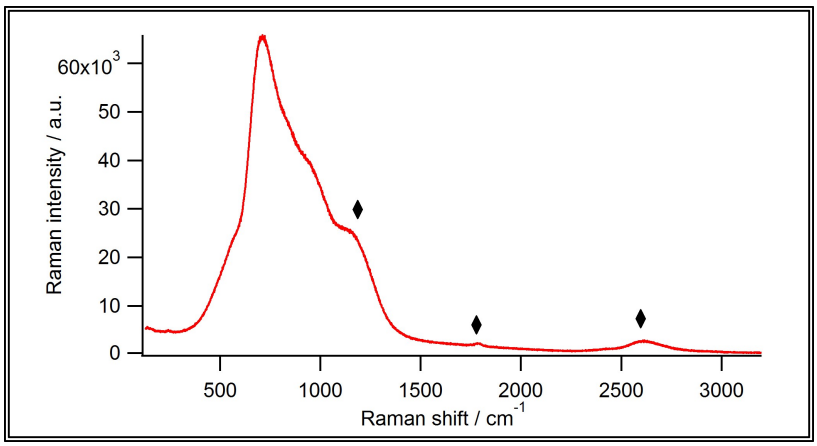

Figure C.12: The Raman spectrum of MAA-based ultrathin film MIP on the Ag/Cr (350°C) on glass substrate.

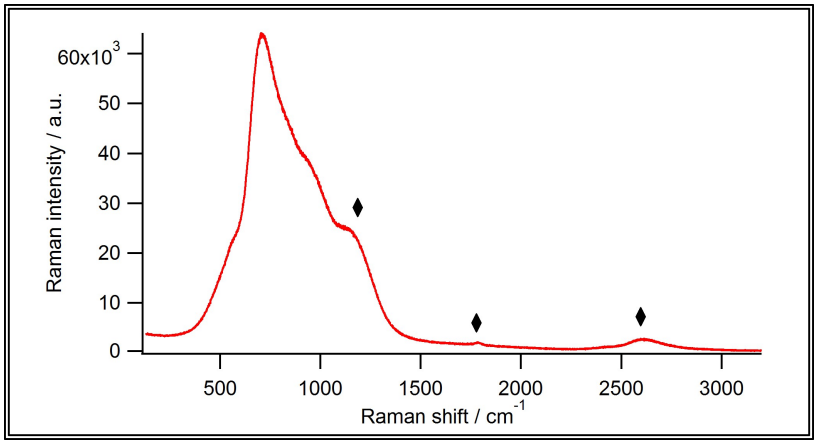

Figure C.13: The Raman spectrum of MAA-based ultrathin film MIP on the Ag/Cr (400°C) on glass substrate

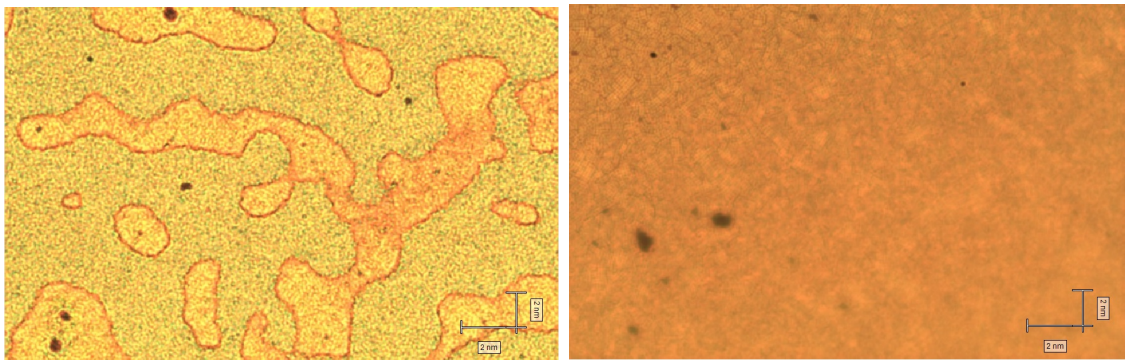

Figure C.14: The images of the Ag/Au/Silica spheres substrates with MIP solution before and after making the substrate hydrophilic. The left figure shows MIP islands on the substrate before making it hydrophilic and The right figure shows MIP film after making it hydrophilic.

C.2 Treatment of the Ag/Au/silica spheres on glass substrate

Figure C.14 shows the results of the treatment of the of Au/Ag/Silica spheres on glass substrates. The left figure shows MIP islands on the substrate before making it hydrophilic. On the other hand, the right figure shows the spread of the MIP solution on the substrate.

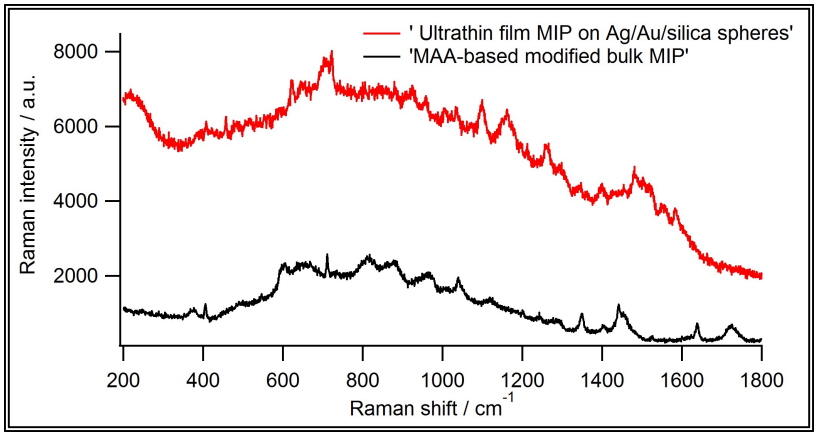

Figure C.15: Comparison between the Raman spectrum of MAA-based modified ultrathin film MIP (modified procedure 1) on the Ag/Au/Silica spheres on glass substrate and the Raman spectrum of MAA-based modified bulk MIP (modified procedure 1)

C.2.0.1 Metal coated MAA-based modified ultrathin film MIP (modified procedure 1) on the Ag/Au/Silica spheres on glass substrate

The result of the Raman spectrum of the formation of MAA-based modified ultrathin film MIP (modified procedure 1) on the Ag/Au/Silica spheres on glass substrate is shown in Figure C.15. The red spectrum shows the Raman spectrum of the ultrathin film on the substrate, and the black spectrum shows the Raman spectrum of the MAA-based modified bulk MIP (modified procedure 1). The peaks observed in the red spectrum are 388, 412, 458, 488, 502, 533, 600, 630, 649, 706, 724, 833, 864, 925, 963, 1009, 1036, 1102, 1135, 1265, 1298, 1345, 1385, 1445, 1470, 1520, 1555, 1590, and 1705 cm^{-1}. The polymer peaks observed in the black spectrum are present at 376, 601, 811, 857, 888, 958, 1042 1125, 1277, 1288, 1409, 1442, 1454, 1636, and 1722 cm^{-1}. The template peaks are present in the black spectrum at 407, 712, 1040, 1350, and 1524 cm^{-1}.

C.3 Discussion

It can be seen from Table C.1 that there is no order between the AFM and profilometer thickness. Ag/Cr film thickness measured by AFM increases as the annealing temperature increases, whereas the film thickness measured by profilometer shows that film thickness decreases with increment of annealing temperature with a exception of 300 °C for both cases. This difference indicates various methods of measuring film thickness. AFM and profilometer have different methods to measure film thickness. In order to measure film thickness, AFM measurements require scratching the film first and then measuring how much the film is scratched, whereas the film thickness is measured by crossing the edge of the film for the profilometer. Therefore, it could be possible that the AFM tip never really scratches away all of the film materials or it scratches away too much. Also, the film thickness measurements were taken only one place for both cases, thus resulting in more variability.

Figure C.1 and Figure C.1 show the high fluorescence of the glass. Some bands are observed at around 480, 853, 1004 cm^{-1}. The fluorescence can also be obtained from Al in the glass. The comparison between the Raman spectra of MAA-based ultrathin film MIP on the Al/plastic, Al/plastic, and plastic substrates shows that Al on the plastic and MIP on Al on the plastic have high fluorescence whereas plastic has different Raman peaks. Also, the plastic peaks are not observed in the spectrum of Al on the plastic due to the high fluorescence. The reason of this phenomenon may be there is internal reflectance within the plastic film due to the Al on top which then leads to high fluorescence signal. In Figure C.4, plastic has many peaks which are matched with the ultrathin film MIP peaks and MAA-based bulk MIP peaks. Therefore, identification of the polymer and template peaks of ultrathin film MIP on the Ag/plastic substrate can be difficult.

In Figure C.5, two shoulders are observed at 660 and 867 cm^{-1}. These peaks are

caused by the presence of Ag nanoparticles [143]. The spectrum of the ultrathin film MIP on the Ag/Cu on plastic substrate is more heavily influenced by the fluorescence than that of the Ag/Cu film on the plastic as seen in Figure C.6. Also, the peaks observed in the two spectra are overlapped with plastic peaks.

As can be seen in Figure C.7, the peaks of the ultrathin film MIP on the Au/Su8 on plastic substrate are overlapped with the plastic peaks of the Au/Su8 film.

In Figure C.8 shows some peaks are overlapped with each other in both spectra, whereas some peaks are different in the ultrathin film MIP on the Au/Ag on plastic substrate. The peaks at 2864, and 2897 cm^{-1} are obtained from phenanthrene molecule of the ultrathin film because these peaks can originate from C-H stretching vibrations [144]. The peak at 546 cm^{-1} is obtained from phenanthrene because phenanthrene has peak at 547 cm^{-1} [127]. The peak intensities are very low because the spectrum are influenced by the glass fluorescence.

In Figure C.9 and Figure C.10 show several peaks of the ultrathin film on the Ag/Cr (250 °C) on glass substrate. The peaks at 936, 1124, 1278, 1426, and 1626 cm^{-1} are obtained from MIP polymer peaks. These peaks are present at 958, 1125, 1277, 1409, and 1636 cm^{-1} in the MAA-based bulk MIP. Also, the peaks at 554, 1066, 1536, and 1610 cm^{-1} are obtained from phenanthrene molecule. These peaks are present at 548, 1040, 1524, and 1616 cm^{-1} in the bulk MIP. The peaks at 1160, 1565, and 1576 cm^{-1} are also obtained from phenanthrene because phenanthrene has peaks at 1170, 1569, and 1576 cm^{-1} [127]. It can be seen that some of the polymer peaks and template peaks are shifted. The cause of this shift may be due to the bonding interaction between MIP molecules and metal surface [144]. Although the spectrum is heavily influenced by the glass fluorescence, the peaks are visible in the spectrum. In Figure C.11, the peaks at 345 and 616 cm^{-1} can be obtained from MIP polymer peaks. The peaks at 194, 741 and 1163 cm^{-1} can be obtained from

phenanthrene. In Figure C.12 and Figure C.12, some shoulders are observed in the spectra, but high fluorescence is obtained from the glass. It seems that annealing process increases the fluorescence of the glass because the glass fluorescence of the Ag/Cr (400 °C) and Ag/Cr (350 °C) are higher than that of the Ag/Cr (300 °C) and Ag/Cr (250 °C), thus obtaining less peaks for the ultrathin film. It is probably possible that glass fluorescence can dominate the ultrathin film MIP peaks.

In Figure C.14, The result of the treatment of making hydrophilic show that it can play an important role in improving the interaction between the substrate and the polymer interface. MIP solution makes islands on the Ag/Au/Silica spheres on glass substrate before making the surface hydrophilic, but the islands of the solution is disappeared after making the surface hydrophilic. 95 % ethanol solution containing 11-mercaptoundecanoic acid was used for making the substrate hydrophilic. This treatment can create COOH acid terminated self assembled monolayer to modify the surface of the substrate. This also can improve the bonding interaction between the interface of the substrate and polymer solution. Most of the literature states that self assembled monolayers on substrates improves wet-ability, adhesion and adsorption properties of the surface of the substrate [145–148].

In Figure C.15, the peaks observed in the red spectrum at 388, 600, 833, 864, 963, 1036, 1135, 1265, 1298, 1445, and 1705 cm^{-1} can be obtained from MIP polymer peaks. The peaks are present at 376, 601, 811, 857, 958, 1042, 1125, 1277, 1288, 1442, and 1722 cm^{-1} in the bulk polymer. Phenanthrene peaks are present in the red spectrum at 412, 706, 1345, and 1520 cm^{-1}. In the black spectrum, the peaks are present at 407, 712, 1350, and 1524 cm^{-1}. It is possible that most of the peaks of the ultrathin film MIP on the substrate are shifted. The cause of this phenomenon may be due to the bonding interaction between MIP molecules and metal surface [144]. In Figure C.15, the other peaks observed in the red spectrum at 502, 649, 724, 925, and

1102 cm^{-1} can be obtained from noise . The peaks at 458, 488, and 533 cm^{-1}can be obtained from phenanthrene because phenanthrene has a weak peak at 442 cm^{-1} a very weak peak at 498 cm^{-1} , and a medium peak at 547 cm^{-1} [127]. Since the peaks are considerably weak according to the literature, the metal can enhance the peak intensities of phenanthrene in the ultrathin film MIP on the Ag/Au/Silica spheres on glass substrate. In the figure, the red spectrum was taken using only 0.1 % laser power, whereas the bulk MIP spectra was taken using 100 % laser power. The peaks in the red spectrum are visible using 0.1 % laser power, which possibly indicates that the metal can enhance the signal of the template of the MIP. The reported literatures describes the MIP -SERS detection method in which SERS is used as a sensitive and selective method involving the enhancement of the Raman scattering intensities of the template molecule [98, 119, 120, 149]. The glass fluorescence is not observed for the film on the substrate.

C.4 Conclusion

Based on the results from this chapter, Ag/Cr (250 ^{o}C) on glass substrate can be useful as a SERS substrate to make ultrathin film MIP. Although the spectrum of the ultrathin film MIP on the Ag/Cr (250 ^{o}C) on glass substrate is influenced by the glass fluorescence, the polymer and template peaks are visible in the spectrum (described in section C.3). Also, Ag/Au/Silica spheres on glass substrate can be useful as a SERS substrate to make ultrathin film MIP. The substrate does not show any glass fluorescence. The template and polymer peaks are visible in the spectrum. The substrate can enhance the template signal of the ultrathin film MIP (described in section C.3).

Bibliography

[1] K. Srogi. Monitoring of environmental exposure to polycyclic aromatic hydrocarbons: a review. *Environmental Chemistry Letters*, 5(4):169–195, 2007.

[2] C.-E. Boström, P. Gerde, A. Hanberg, B. Jernström, C. Johansson, T. Kyrklund, A. Rannug, M. Törnqvist, K. Victorin, and R. Westerholm. Cancer risk assessment, indicators, and guidelines for polycyclic aromatic hydrocarbons in the ambient air. *Environmental Health Perspectives*, 110(Suppl 3):451, 2002.

[3] A. S. Nagy, J. Szabó, and I. Vass. Occurrence and distribution of polycyclic aromatic hydrocarbons in surface water and sediments of the Danube River and its tributaries, Hungary. *Journal of Environmental Science and Health, Part A*, 49(10):1134–1141, 2014.

[4] G. Witt. Polycyclic aromatic hydrocarbons in water and sediment of the Baltic Sea. *Marine Pollution Bulletin*, 31(4):237–248, 1995.

[5] A. M. Mastral and M. S. Callen. A review on polycyclic aromatic hydrocarbon (PAH) emissions from energy generation. *Environmental Science & Technology*, 34(15):3051–3057, 2000.

[6] J. Nam, B. Song, K. Eom, S. Lee, and A. Smith. Distribution of polycyclic aromatic hydrocarbons in agricultural soils in South Korea. *Chemosphere*, 50(10):1281–1289, 2003.

[7] E. Manoli and C. Samara. Polycyclic aromatic hydrocarbons in natural waters: sources, occurrence and analysis. *TrAC Trends in Analytical Chemistry*, 18(6):417–428, 1999.

[8] A. Ball and A. Truskewycz. Polyaromatic hydrocarbon exposure: an ecological impact ambiguity. *Environmental Science and Pollution Research*, 20(7):4311–4326, 2013.

[9] A. Haritash and C. Kaushik. Biodegradation aspects of polycyclic aromatic hydrocarbons (PAHs): a review. *Journal of Hazardous Materials*, 169(1):1–15, 2009.

[10] Y.-L. Wei, L.-J. Bao, C.-C. Wu, Z.-C. He, and E. Y. Zeng. Association of soil polycyclic aromatic hydrocarbon levels and anthropogenic impacts in a rapidly urbanizing region: Spatial distribution, soil–air exchange and ecological risk. *Science of the Total Environment*, 473:676–684, 2014.

[11] R. Laflamme and R. A. Hites. The global distribution of polycyclic aromatic hydrocarbons in recent sediments. *Geochimica et Cosmochimica Acta*, 42(3):289–303, 1978.

[12] S. K. Samanta, O. V. Singh, and R. K. Jain. Polycyclic aromatic hydrocarbons: environmental pollution and bioremediation. *TRENDS in Biotechnology*, 20(6):243–248, 2002.

[13] H. Soclo, P. Garrigues, and M. Ewald. Origin of polycyclic aromatic hydrocarbons (PAHs) in coastal marine sediments: case studies in Cotonou (Benin) and Aquitaine (France) areas. *Marine Pollution Bulletin*, 40(5):387–396, 2000.

[14] J. Readman, G. Fillmann, I. Tolosa, J. Bartocci, J.-P. Villeneuve, C. Catinni, and L. Mee. Petroleum and PAH contamination of the Black Sea. *Marine Pollution Bulletin*, 44(1):48–62, 2002.

[15] A. Filipkowska, L. Lubecki, and G. Kowalewska. Polycyclic aromatic hydrocarbon analysis in different matrices of the marine environment. *Analytica Chimica Acta*, 547(2):243–254, 2005.

[16] J. Zhou and K. Maskaoui. Distribution of polycyclic aromatic hydrocarbons in water and surface sediments from Daya Bay, China. *Environmental Pollution*, 121(2):269–281, 2003.

[17] A. S. Nagy, J. Szabó, and I. Vass. Occurrence and distribution of polycyclic aromatic hydrocarbons in surface water of the Raba River, Hungary. *Journal of Environmental Science and Health, Part A*, 48(10):1190–1200, 2013.

[18] S. G. Wakeham. Aliphatic and polycyclic aromatic hydrocarbons in Black Sea sediments. *Marine Chemistry*, 53(3):187–205, 1996.

[19] S. Dahle, V. M. Savinov, G. G. Matishov, A. Evenset, and K. Næs. Polycyclic aromatic hydrocarbons (PAHs) in bottom sediments of the Kara Sea shelf, Gulf of Ob and Yenisei Bay. *Science of the Total Environment*, 306(1):57–71, 2003.

[20] P. C. Hartmann, J. G. Quinn, R. W. Cairns, and J. W. King. The distribution and sources of polycyclic aromatic hydrocarbons in Narragansett Bay surface sediments. *Marine Pollution Bulletin*, 48(3):351–358, 2004.

[21] P. Baumard, H. Budzinski, P. Garrigues, H. Dizer, and P. Hansen. Polycyclic aromatic hydrocarbons in recent sediments and mussels (Mytilus edulis) from the Western Baltic Sea: occurrence, bioavailability and seasonal variations. *Marine Environmental Research*, 47(1):17–47, 1999.

[22] M. Notar, H. Leskovšek, and J. Faganeli. Composition, distribution and sources of polycyclic aromatic hydrocarbons in sediments of the Gulf of Trieste, Northern Adriatic Sea. *Marine Pollution Bulletin*, 42(1):36–44, 2001.

[23] R. Law, V. Dawes, R. Woodhead, and P. Matthiessen. Polycyclic aromatic hydrocarbons (PAH) in seawater around England and Wales. *Marine Pollution Bulletin*, 34(5):306–322, 1997.

[24] R. Lohmann, R. Gioia, K. C. Jones, L. Nizzetto, C. Temme, Z. Xie, D. Schulz-Bull, I. Hand, E. Morgan, and L. Jantunen. Organochlorine pesticides and PAHs in the surface water and atmosphere of the North Atlantic and Arctic Ocean. *Environmental Science & Technology*, 43(15):5633–5639, 2009.

[25] X. Luo, B. Mai, Q. Yang, J. Fu, G. Sheng, and Z. Wang. Polycyclic aromatic hydrocarbons (PAHs) and organochlorine pesticides in water columns from the Pearl River and the Macao harbor in the Pearl River Delta in South China. *Marine Pollution Bulletin*, 48(11):1102–1115, 2004.

[26] S. B. Tavakoly Sany, R. Hashim, M. Rezayi, A. Salleh, M. A. Rahman, O. Safari, and A. Sasekumar. Human health risk of polycyclic aromatic hydrocarbons from consumption of blood cockle and exposure to contaminated sediments and water along the Klang Strait, Malaysia. *Marine Pollution Bulletin*, 84(1-2):268–279, 2014.

[27] G. Mastrangelo, E. Fadda, and V. Marzia. Polycyclic aromatic hydrocarbons and cancer in man. *Environmental Health Perspectives*, 104(11):1166, 1996.

[28] E. Aas, T. Baussant, L. Balk, B. Liewenborg, and O. K. Andersen. PAH metabolites in bile, cytochrome P4501A and DNA adducts as environmental risk pa-

rameters for chronic oil exposure: a laboratory experiment with Atlantic cod. *Aquatic Toxicology*, 51(2):241–258, 2000.

[29] J. Sturve, L. Hasselberg, H. Fälth, M. Celander, and L. Förlin. Effects of North Sea oil and alkylphenols on biomarker responses in juvenile Atlantic cod (Gadus morhua). *Aquatic Toxicology*, 78:S73–S78, 2006.

[30] J. P. Incardona, T. K. Collier, and N. L. Scholz. Defects in cardiac function precede morphological abnormalities in fish embryos exposed to polycyclic aromatic hydrocarbons. *Toxicology and Applied Pharmacology*, 196(2):191–205, 2004.

[31] J. Mu, J. Wang, F. Jin, X. Wang, and H. Hong. Comparative embryotoxicity of phenanthrene and alkyl-phenanthrene to marine medaka (Oryzias melastigma). *Marine Pollution Bulletin*, 85(2):505–515, 2014.

[32] M. G. Carls, S. D. Rice, and J. E. Hose. Sensitivity of fish embryos to weathered crude oil: Part I. Low-level exposure during incubation causes malformations, genetic damage, and mortality in larval pacific herring (Clupea pallasi). *Environmental Toxicology and Chemistry*, 18(3):481–493, 1999.

[33] D. M. Pampanin and M. O. Sydnes. *Polycyclic aromatic hydrocarbons a constituent of petroleum: Presence and influence in the aquatic environment*, chapter 5. InTech, 2013.

[34] H. Somerville, D. Bennett, J. Davenport, M. Holt, A. Lynes, A. Mahieu, B. McCourt, J. Parker, R. Stephenson, R. Watkinson, et al. Environmental effect of produced water from North Sea oil operations. *Marine Pollution Bulletin*, 18(10):549–558, 1987.

[35] T. Bakke, J. Klungsøyr, and S. Sanni. Environmental impacts of produced water and drilling waste discharges from the Norwegian offshore petroleum industry. *Marine Environmental Research*, 92:154–169, 2013.

[36] S. Henderson, S. Grigson, P. Johnson, and B. Roddie. Potential impact of production chemicals on the toxicity of produced water discharges from North Sea oil platforms. *Marine Pollution Bulletin*, 38(12):1141–1151, 1999.

[37] D. A. Holdway. The acute and chronic effects of wastes associated with offshore oil and gas production on temperate and tropical marine ecological processes. *Marine Pollution Bulletin*, 44(3):185–203, 2002.

[38] T. I. Røe Utvik. Chemical characterisation of produced water from four offshore oil production platforms in the North Sea. *Chemosphere*, 39(15):2593–2606, 1999.

[39] R. C. Sundt, A. Ruus, H. Jonsson, H. Skarphéðinsdóttir, S. Meier, M. Grung, J. Beyer, and D. M. Pampanin. Biomarker responses in Atlantic cod (Gadus morhua) exposed to produced water from a North Sea oil field: Laboratory and field assessments. *Marine Pollution Bulletin*, 64(1):144–152, 2012.

[40] E. Farmen, C. Harman, K. Hylland, and K.-E. Tollefsen. Produced water extracts from North Sea oil production platforms result in cellular oxidative stress in a rainbow trout in vitro bioassay. *Marine Pollution Bulletin*, 60(7):1092–1098, 2010.

[41] G. Durell, T. Røe Utvik, S. Johnsen, T. Frost, and J. Neff. Oil well produced water discharges to the North Sea. Part I: Comparison of deployed mussels (Mytilus edulis), semi-permeable membrane devices, and the DREAM model predictions

to estimate the dispersion of polycyclic aromatic hydrocarbons. *Marine Environmental Research*, 62(3):194–223, 2006.

[42] J. M. Neff, S. Johnsen, T. K. Frost, T. I. Røe Utvik, and G. S. Durell. Oil well produced water discharges to the North Sea. Part II: Comparison of deployed mussels (Mytilus edulis) and the DREAM model to predict ecological risk. *Marine Environmental Research*, 62(3):224–246, 2006.

[43] G. S. Durell, S. Johnsen, et al. Determining produced water originating polycyclic aromatic hydrocarbons in North Sea waters: comparison of sampling techniques. *Marine Pollution Bulletin*, 38(11):977–989, 1999.

[44] C. Harman, S. Brooks, R. C. Sundt, S. Meier, and M. Grung. Field comparison of passive sampling and biological approaches for measuring exposure to PAH and alkylphenols from offshore produced water discharges. *Marine Pollution Bulletin*, 63(5):141–148, 2011.

[45] A. Fakhru'l-Razi, A. Pendashteh, L. C. Abdullah, D. R. A. Biak, S. S. Madaeni, and Z. Z. Abidin. Review of technologies for oil and gas produced water treatment. *Journal of Hazardous Materials*, 170(2):530–551, 2009.

[46] E. T. Igunnu and G. Z. Chen. Produced water treatment technologies. *International Journal of Low-Carbon Technologies*, doi:10.1093/ijlct/cts049.

[47] E. D. O. R. Lopes, O. B. Weber, and L. Araújo. Short-term effects of produced water on microbial activity in semiarid soil. *Int. J. Curr. Microbiol. App. Sci*, 3(2):395–403, 2014.

[48] R. C. Sundt, D. M. Pampanin, M. Grung, J. Baršienė, and A. Ruus. PAH body burden and biomarker responses in mussels (Mytilus edulis) exposed to

produced water from a North Sea oil field: Laboratory and field assessments. *Marine Pollution Bulletin*, 62(7):1498–1505, 2011.

[49] A. Abrahamson, I. Brandt, B. Brunström, R. C. Sundt, and E. H. Jørgensen. Monitoring contaminants from oil production at sea by measuring gill EROD activity in Atlantic cod (Gadus morhua). *Environmental Pollution*, 153(1):169–175, 2008.

[50] G. Carlsson, L. Norrgren, K. Hylland, and K. Tollefsen. Toxicity Screening of Produced Water Extracts in a Zebrafish Embryo Assay. *Journal of Toxicology and Environmental Health, Part A*, 77(9-11):600–615, 2014.

[51] D. R. Livingstone. Biotechnology and pollution monitoring: use of molecular biomarkers in the aquatic environment. *Journal of Chemical Technology and Biotechnology*, 57(3):195–211, 1993.

[52] A. Marrucci, B. Marras, S. S. Campisi, and M. Schintu. Using SPMDs to monitor the seawater concentrations of PAHs and PCBs in marine protected areas (Western Mediterranean). *Marine Pollution Bulletin*, 75(1):69–75, 2013.

[53] B. J. Richardson, G. J. Zheng, E. S. Tse, S. B. De Luca-Abbott, S. Y. Siu, and P. K. Lam. A comparison of polycyclic aromatic hydrocarbon and petroleum hydrocarbon uptake by mussels (Perna viridis) and semi-permeable membrane devices (SPMDs) in Hong Kong coastal waters. *Environmental Pollution*, 122(2):223–227, 2003.

[54] S. Kröger, S. Piletsky, and A. P. Turner. Biosensors for marine pollution research, monitoring and control. *Marine Pollution Bulletin*, 45(1):24–34, 2002.

[55] R. J. Krupadam, M. S. Khan, and S. R. Wate. Removal of probable human carcinogenic polycyclic aromatic hydrocarbons from contaminated water using molecularly imprinted polymer. *Water Research*, 44(3):681–688, 2010.

[56] P. Spégel, L. Schweitz, and S. Nilsson. Molecularly imprinted polymers. *Analytical and Bioanalytical Chemistry*, 372(1):37–38, 2002.

[57] M. Whitcombe and E. Vulfson. Imprinted polymers. *Advanced Materials*, 13(7):467–478, 2001.

[58] L. Chen, S. Xu, and J. Li. Recent advances in molecular imprinting technology: current status, challenges and highlighted applications. *Chemical Society Reviews*, 40(5):2922–2942, 2011.

[59] J. E. Lofgreen and G. A. Ozin. Controlling morphology and porosity to improve performance of molecularly imprinted sol–gel silica. *Chemical Society Reviews*, 43(3):911–933, 2014.

[60] C. Alexander, H. S. Andersson, L. I. Andersson, R. J. Ansell, N. Kirsch, I. A. Nicholls, J. O'Mahony, and M. J. Whitcombe. Molecular imprinting science and technology: a survey of the literature for the years up to and including 2003. *Journal of Molecular Recognition*, 19(2):106–180, 2006.

[61] H. Yan and K. H. Row. Characteristic and synthetic approach of molecularly imprinted polymer. *International Journal of Molecular Sciences*, 7(5):155–178, 2006.

[62] M. C. Moreno-Bondi, F. Navarro-Villoslada, E. Benito-Pena, and J. L. Urraca. Molecularly imprinted polymers as selective recognition elements in optical sensing. *Current Analytical Chemistry*, 4(4):316–340, 2008.

[63] G. Vasapollo, R. D. Sole, L. Mergola, M. R. Lazzoi, A. Scardino, S. Scorrano, and G. Mele. Molecularly imprinted polymers: present and future prospective. *International Journal of Molecular Sciences*, 12(9):5908–5945, 2011.

[64] M. Yan and A. Kapua. Fabrication of molecularly imprinted polymer microstructures. *Analytica Chimica Acta*, 435(1):163–167, 2001.

[65] K. Haupt and K. Mosbach. Molecularly imprinted polymers and their use in biomimetic sensors. *Chemical Reviews*, 100(7):2495–2504, 2000.

[66] A. Martin-Esteban. Molecularly imprinted polymers: new molecular recognition materials for selective solid-phase extraction of organic compounds. *Fresenius' Journal of Analytical Chemistry*, 370(7):795–802, 2001.

[67] Z. Meng, W. Chen, and A. Mulchandani. Removal of estrogenic pollutants from contaminated water using molecularly imprinted polymers. *Environmental Science & Technology*, 39(22):8958–8962, 2005.

[68] K. Haupt. Molecularly imprinted sorbent assays and the use of non-related probes. *Reactive and Functional Polymers*, 41(1):125–131, 1999.

[69] X. Shen, L. Zhu, N. Wang, L. Ye, and H. Tang. Molecular imprinting for removing highly toxic organic pollutants. *Chemical Communications*, 48(6):788–798, 2012.

[70] Z. Meng, Q. Zhang, M. Xue, D. Wang, and A. Wang. Removal of 2, 4, 6-Trinitrotoluene from "Pink Water" Using Molecularly-Imprinted Absorbent. *Propellants, Explosives, Pyrotechnics*, 37(1):100–106, 2012.

[71] K. Yano and I. Karube. Molecularly imprinted polymers for biosensor applications. *TrAC Trends in Analytical Chemistry*, 18(3):199–204, 1999.

[72] F. L. Dickert and O. Hayden. Molecular imprinting in chemical sensing. *TrAC Trends in Analytical Chemistry*, 18(3):192–199, 1999.

[73] A. Merkoci and S. Alegret. New materials for electrochemical sensing IV. Molecular imprinted polymers. *TrAC Trends in Analytical Chemistry*, 21(11):717–725, 2002.

[74] M. Blanco-López, M. Lobo-Castanon, A. Miranda-Ordieres, and P. Tunon-Blanco. Electrochemical sensors based on molecularly imprinted polymers. *TrAC Trends in Analytical Chemistry*, 23(1):36–48, 2004.

[75] S. Piletsky, E. Piletskaya, A. Elgersma, K. Yano, I. Karube, Y. P. Parhometz, and A. El'skaya. Atrazine sensing by molecularly imprinted membranes. *Biosensors and Bioelectronics*, 10(9):959–964, 1995.

[76] S. Piletsky, E. Piletskaya, T. Sergeyeva, T. Panasyuk, and A. El'Skaya. Molecularly imprinted self-assembled films with specificity to cholesterol. *Sensors and Actuators B: Chemical*, 60(2):216–220, 1999.

[77] C. Xie, B. Liu, Z. Wang, D. Gao, G. Guan, and Z. Zhang. Molecular imprinting at walls of silica nanotubes for TNT recognition. *Analytical Chemistry*, 80(2):437–443, 2008.

[78] A. L. Jenkins, R. Yin, and J. L. Jensen. Molecularly imprinted polymer sensors for pesticide and insecticide detection in water. *Analyst*, 126(6):798–802, 2001.

[79] V. B. Kandimalla and H. Ju. Molecular imprinting: a dynamic technique for diverse applications in analytical chemistry. *Analytical and Bioanalytical Chemistry*, 380(4):587–605, 2004.

[80] K. Haupt and K. Mosbach. Plastic antibodies: developments and applications. *Trends in Biotechnology*, 16(11):468–475, 1998.

[81] Y. Hoshino, H. Koide, T. Urakami, H. Kanazawa, T. Kodama, N. Oku, and K. J. Shea. Recognition, neutralization, and clearance of target peptides in the bloodstream of living mice by molecularly imprinted polymer nanoparticles: a plastic antibody. *Journal of the American Chemical Society*, 132(19):6644–6645, 2010.

[82] C. He, Y. Long, J. Pan, K. Li, and F. Liu. Application of molecularly imprinted polymers to solid-phase extraction of analytes from real samples. *Journal of Biochemical and Biophysical Methods*, 70(2):133–150, 2007.

[83] R. Voicu, K. Faid, A. A. Farah, F. Bensebaa, R. Barjovanu, C. Py, and Y. Tao. Nanotemplating for two-dimensional molecular imprinting. *Langmuir*, 23(10):5452–5458, 2007.

[84] Y. Hu, J. Pan, K. Zhang, H. Lian, and G. Li. Novel applications of molecularly-imprinted polymers in sample preparation. *TrAC Trends in Analytical Chemistry*, 43:37–52, 2013.

[85] G. González Paniagua, P. Hernando Fernández, and J. S. Durand Alegría. A morphological study of molecularly imprinted polymers using the scanning electron microscope. *Analytica Chimica Acta*, 557(1):179–183, 2006.

[86] D. McStay, A. H. Al-Obaidi, R. Hoskins, and P. J. Quinn. Raman spectroscopy of molecular imprinted polymers. *Journal of Optics A: Pure and Applied Optics*, 7(6):S340, 2005.

[87] F. Barahona, E. Turiel, P. A. Cormack, and A. Martín-Esteban. Chromatographic performance of molecularly imprinted polymers: Core-shell micro-

spheres by precipitation polymerization and grafted MIP films via iniferter-modified silica beads. *Journal of Polymer Science Part A: Polymer Chemistry*, 48(5):1058–1066, 2010.

[88] R. J. Ansell and K. Mosbach. Magnetic molecularly imprinted polymer beads for drug radioligand binding assay. *Analyst*, 123(7):1611–1616, 1998.

[89] X. Liu, C. Ouyang, R. Zhao, D. Shangguan, Y. Chen, and G. Liu. Monolithic molecularly imprinted polymer for sulfamethoxazole and molecular recognition properties in aqueous mobile phase. *Analytica Chimica Acta*, 571(2):235–241, 2006.

[90] R. J. Krupadam, B. Bhagat, S. R. Wate, G. L. Bodhe, B. Sellergren, and Y. Anjaneyulu. Fluorescence spectrophotometer analysis of polycyclic aromatic hydrocarbons in environmental samples based on solid phase extraction using molecularly imprinted polymer. *Environmental Science & Technology*, 43(8):2871–2877, 2009.

[91] R. J. Krupadam, E. E. Nesterov, and D. A. Spivak. Highly selective detection of oil spill polycyclic aromatic hydrocarbons using molecularly imprinted polymers for marine ecosystems. *Journal of Hazardous Materials*, 274:1–7, 2014.

[92] X. Song, J. Li, S. Xu, R. Ying, J. Ma, C. Liao, D. Liu, J. Yu, and L. Chen. Determination of 16 polycyclic aromatic hydrocarbons in seawater using molecularly imprinted solid-phase extraction coupled with gas chromatography-mass spectrometry. *Talanta*, 99:75–82, 2012.

[93] H. Kim and G. Guiochon. Comparison of the thermodynamic properties of particulate and monolithic columns of molecularly imprinted copolymers. *Analytical Chemistry*, 77(1):93–102, 2005.

[94] R. H. Schmidt, K. Mosbach, and K. Haupt. A Simple Method for Spin-Coating Molecularly Imprinted Polymer Films of Controlled Thickness and Porosity. *Advanced Materials*, 16(8):719–722, 2004.

[95] K. Das, J. Penelle, and V. M. Rotello. Selective picomolar detection of hexachlorobenzene in water using a quartz crystal microbalance coated with a molecularly imprinted polymer thin film. *Langmuir*, 19(9):3921–3925, 2003.

[96] J. Mathew-Krotz and K. Shea. Imprinted polymer membranes for the selective transport of targeted neutral molecules. *Journal of the American Chemical Society*, 118(34):8154–8155, 1996.

[97] S.-W. Lee, I. Ichinose, and T. Kunitake. Molecular imprinting of azobenzene carboxylic acid on a TiO2 ultrathin film by the surface sol-gel process. *Langmuir*, 14(10):2857–2863, 1998.

[98] E. L. Holthoff, D. N. Stratis-Cullum, and M. E. Hankus. A nanosensor for TNT detection based on molecularly imprinted polymers and surface enhanced raman scattering. *Sensors*, 11(3):2700–2714, 2011.

[99] I. Tokareva, I. Tokarev, S. Minko, E. Hutter, and J. H. Fendler. Ultrathin molecularly imprinted polymer sensors employing enhanced transmission surface plasmon resonance spectroscopy. *Chemical Communications*, (31):3343–3345, 2006.

[100] F. L. Dickert, P. Achatz, and K. Halikias. Double molecular imprinting–a new sensor concept for improving selectivity in the detection of polycyclic aromatic hydrocarbons (PAHs) in water. *Fresenius' Journal of Analytical Chemistry*, 371(1):11–15, 2001.

[101] J. Du and C. Jing. Preparation of thiol modified Fe3O4@ Ag magnetic SERS probe for PAHs detection and identification. *The Journal of Physical Chemistry C*, 115(36):17829–17835, 2011.

[102] L.-L. Qu, Y.-T. Li, D.-W. Li, J.-Q. Xue, J. S. Fossey, and Y.-T. Long. Humic acids-based one-step fabrication of SERS substrates for detection of polycyclic aromatic hydrocarbons. *Analyst*, 138(5):1523–1528, 2013.

[103] P. Sheng, S. Wu, L. Bao, X. Wang, Z. Chen, and Q. Cai. Surface enhanced Raman scattering detecting polycyclic aromatic hydrocarbons with gold nanoparticle-modified TiO2 nanotube arrays. *New Journal of Chemistry*, 36(12):2501–2505, 2012.

[104] Y. Xie, X. Wang, X. Han, X. Xue, W. Ji, Z. Qi, J. Liu, B. Zhao, and Y. Ozaki. Sensing of polycyclic aromatic hydrocarbons with cyclodextrin inclusion complexes on silver nanoparticles by surface-enhanced Raman scattering. *Analyst*, 135(6):1389–1394, 2010.

[105] V. Pino, J. Ayala, A. Afonso, and V. Gonzalez. Determination of polycyclic aromatic hydrocarbons in seawater by high-performance liquid chromatography with fluorescence detection following micelle-mediated preconcentration. *Journal of Chromatography A*, 949(1):291–299, 2002.

[106] K. Kantarovich, I. Tsarfati, L. A. Gheber, K. Haupt, and I. Bar. Reading microdots of a molecularly imprinted polymer by surface-enhanced Raman spectroscopy. *Biosensors and Bioelectronics*, 26(2):809–814, 2010.

[107] K. Kantarovich, A.-S. Belmont, K. Haupt, I. Bar, and L. A. Gheber. Detection of template binding to molecularly imprinted polymers by Raman microspectroscopy. *Applied Physics Letters*, 94(19):194103, 2009.

[108] X. Shi, J. Ma, R. Zheng, C. Wang, and H.-D. Kronfeldt. An improved self-assembly gold colloid film as surface-enhanced Raman substrate for detection of trace-level polycyclic aromatic hydrocarbons in aqueous solution. *Journal of Raman Spectroscopy*, 43(10):1354–1359, 2012.

[109] J. Costa, A. Sant'Ana, P. Corio, and M. Temperini. Chemical analysis of polycyclic aromatic hydrocarbons by surface-enhanced Raman spectroscopy. *Talanta*, 70(5):1011–1016, 2006.

[110] A. Filipkowska, L. Lubecki, and G. Kowalewska. Polycyclic aromatic hydrocarbon analysis in different matrices of the marine environment. *Analytica Chimica Acta*, 547(2):243–254, 2005.

[111] H. Schmidt, N. Bich Ha, J. Pfannkuche, H. Amann, H.-D. Kronfeldt, and G. Kowalewska. Detection of PAHs in seawater using surface-enhanced Raman scattering (SERS). *Marine Pollution Bulletin*, 49(3):229–234, 2004.

[112] M. Muniz-Miranda, C. Gellini, and E. Giorgetti. Surface-enhanced Raman scattering from copper nanoparticles obtained by laser ablation. *The Journal of Physical Chemistry C*, 115(12):5021–5027, 2011.

[113] A. C. Ferrari and D. M. Basko. Raman spectroscopy as a versatile tool for studying the properties of graphene. *Nature Nanotechnology*, 8(4):235–246, 2013.

[114] A. Robinson, S. Harroun, J. Bergman, and C. Brosseau. Portable electrochemical surface-enhanced Raman spectroscopy system for routine spectroelectrochemical analysis. *Analytical Chemistry*, 84(3):1760–1764, 2012.

[115] D. Xu, J. Gu, W. Wang, X. Yu, K. Xi, and X. Jia. Development of chitosan-coated gold nanoflowers as SERS-active probes. *Nanotechnology*, 21(37):375101, 2010.

[116] D. Li, D.-W. Li, J. S. Fossey, and Y.-T. Long. Portable surface-enhanced Raman scattering sensor for rapid detection of aniline and phenol derivatives by on-site electrostatic preconcentration. *Analytical Chemistry*, 82(22):9299–9305, 2010.

[117] Y.-H. Kwon, K. Sowoidnich, H. Schmidt, and H.-D. Kronfeldt. Application of calixarene to high active surface-enhanced Raman scattering (SERS) substrates suitable for in situ detection of polycyclic aromatic hydrocarbons (PAHs) in seawater. *Journal of Raman Spectroscopy*, 43(8):1003–1009, 2012.

[118] Y. Xie, X. Wang, X. Han, W. Song, W. Ruan, J. Liu, B. Zhao, and Y. Ozaki. Selective SERS detection of each polycyclic aromatic hydrocarbon (PAH) in a mixture of five kinds of PAHs. *Journal of Raman Spectroscopy*, 42(5):945–950, 2011.

[119] K. Kantarovich, I. Tsarfati, L. A. Gheber, K. Haupt, and I. Bar. Writing droplets of molecularly imprinted polymers by nano fountain pen and detecting their molecular interactions by surface-enhanced Raman scattering. *Analytical Chemistry*, 81(14):5686–5690, 2009.

[120] P. Liu, R. Liu, G. Guan, C. Jiang, S. Wang, and Z. Zhang. Surface-enhanced Raman scattering sensor for theophylline determination by molecular imprinting on silver nanoparticles. *Analyst*, 136(20):4152–4158, 2011.

[121] P. Jothimuthu, A. Carroll, A. A. S. Bhagat, G. Lin, J. E. Mark, and I. Papautsky. Photodefinable PDMS thin films for microfabrication applications. *Journal of Micromechanics and Microengineering*, 19(4):045024, 2009.

[122] J. H. Koschwanez, R. H. Carlson, and D. R. Meldrum. Thin PDMS films using long spin times or tert-butyl alcohol as a solvent. *PLoS One*, 4(2):e4572, 2009.

[123] A. A. S. Bhagat, P. Jothimuthu, and I. Papautsky. Photodefinable polydimethylsiloxane (PDMS) for rapid lab-on-a-chip prototyping. *Lab on a Chip*, 7(9):1192–1197, 2007.

[124] M. M. Rahman. *Metal Thin Films as SERS Substrates for the detection of PAHs*. PhD thesis, Memorial University of Newfoundland, 2013.

[125] T. Kakiuchi, M. Iida, N. Gon, D. Hobara, S.-i. Imabayashi, and K. Niki. Miscibility of adsorbed 1-undecanethiol and 11-mercaptoundecanoic acid species in binary self-assembled monolayers on Au (111). *Langmuir*, 17(5):1599–1603, 2001.

[126] M. C. Leopold and E. F. Bowden. Influence of gold substrate topography on the voltammetry of cytochrome c adsorbed on carboxylic acid terminated self-assembled monolayers. *Langmuir*, 18(6):2239–2245, 2002.

[127] A. Alajtal, H. Edwards, M. Elbagerma, and I. Scowen. The effect of laser wavelength on the Raman Spectra of phenanthrene, chrysene, and tetracene: Implications for extra-terrestrial detection of polyaromatic hydrocarbons. *Spectrochimica Acta Part A: Molecular and Biomolecular Spectroscopy*, 76(1):1–5, 2010.

[128] H. Kim. *New Insights Into the Binding Site Formation and the Performance of Molecularly Imprinted Polymers*. PhD thesis, University of Akron, 2004.

[129] S. E. Campbell, M. Collins, L. Xie, and J. J. BelBruno. Surface morphology of spin-coated molecularly imprinted polymer films. *Surface and Interface Analysis*, 41(4):347–356, 2009.

[130] D. Bornside, C. Macosko, and L.-E. SCRIVEN. On the modeling of spin coating. *Journal of Imaging Technology*, 13(4):122–130, 1987.

[131] D. B. Hall, P. Underhill, and J. M. Torkelson. Spin coating of thin and ultrathin polymer films. *Polymer Engineering & Science*, 38(12):2039–2045, 1998.

[132] D. A. Spivak. Optimization, evaluation, and characterization of molecularly imprinted polymers. *Advanced Drug Delivery Reviews*, 57(12):1779–1794, 2005.

[133] A. O. Gryshchenko and C. S. Bottaro. Development of Molecularly Imprinted Polymer in Porous Film Format for Binding of Phenol and Alkylphenols from Water. *International Journal of Molecular Sciences*, 15(1):1338–1357, 2014.

[134] S. Bhattacharya, A. Datta, J. M. Berg, and S. Gangopadhyay. Studies on surface wettability of poly (dimethyl) siloxane (PDMS) and glass under oxygen-plasma treatment and correlation with bond strength. *Journal oF Microelectromechanical Systems*, 14(3):590–597, 2005.

[135] Plasma etching. `http://www.ccs.unicamp.br/novosite/ie521/files/2013/08/cap10.pdf`. Accessed: 2014-06-10.

[136] S. C. Bae, H. Lee, Z. Lin, and S. Granick. Chemical imaging in a surface forces apparatus: confocal Raman spectroscopy of confined poly (dimethylsiloxane). *Langmuir*, 21(13):5685–5688, 2005.

[137] Y.-T. Chen and D. Lee. A bonding technique using hydrophilic SU-8. *Journal of Micromechanics and Microengineering*, 17(10):1978, 2007.

[138] C. Cao, S. W. Birtwell, J. Høgberg, H. Morgan, A. Wolff, and D. D. Bang. Gold Nanoparticles-Coated SU-8 for Sensitive Fluorescence-Based Detections of DNA. *Diagnostics*, 2(4):72–82, 2012.

[139] D. T. Eddington, J. P. Puccinelli, and D. J. Beebe. Thermal aging and reduced hydrophobic recovery of polydimethylsiloxane. *Sensors and Actuators B: Chemical*, 114(1):170–172, 2006.

[140] D. Bodas and C. Khan-Malek. Formation of more stable hydrophilic surfaces of PDMS by plasma and chemical treatments. *Microelectronic Engineering*, 83(4):1277–1279, 2006.

[141] J. H. van Zanten, W. E. Wallace, and W.-l. Wu. Effect of strongly favorable substrate interactions on the thermal properties of ultrathin polymer films. *Physical Review E*, 53(3):R2053, 1996.

[142] J. N. Lee, C. Park, and G. M. Whitesides. Solvent compatibility of poly (dimethylsiloxane)-based microfluidic devices. *Analytical Chemistry*, 75(23):6544–6554, 2003.

[143] V. Shinde, P. Jadhav, J. Kim, and P. Patil. One-step synthesis and characterization of anisotropic silver nanoparticles: application for enhanced antibacterial activity of natural fabric. *Journal of Materials Science*, 48(24):8393–8401, 2013.

[144] E. del Puerto, C. Domingo, S. Sanchez-Cortes, J. V. García-Ramos, and R. F. Aroca. Plasmon Enhanced Spectroscopy of N,N'-Dialkylquinacridones Used as Codopants in OLEDs. *The Journal of Physical Chemistry C*, 115(34):16838–16843, 2011.

[145] H. H. Persson, W. R. Caseri, and U. W. Suter. Versatile method for chemical reactions with self-assembled monolayers of alkanethiols on gold. *Langmuir*, 17(12):3643–3650, 2001.

[146] Y. Arima and H. Iwata. Effect of wettability and surface functional groups on protein adsorption and cell adhesion using well-defined mixed self-assembled monolayers. *Biomaterials*, 28(20):3074–3082, 2007.

[147] N. Faucheux, R. Schweiss, K. Lützow, C. Werner, and T. Groth. Self-assembled monolayers with different terminating groups as model substrates for cell adhesion studies. *Biomaterials*, 25(14):2721–2730, 2004.

[148] A. G. Frutos, J. M. Brockman, and R. M. Corn. Reversible protection and reactive patterning of amine-and hydroxyl-terminated self-assembled monolayers on gold surfaces for the fabrication of biopolymer arrays. *Langmuir*, 16(5):2192–2197, 2000.

[149] L. Chang, Y. Ding, and X. Li. Surface molecular imprinting onto silver microspheres for surface enhanced Raman scattering applications. *Biosensors and Bioelectronics*, 50:106–110, 2013.